

UNIVERSITY OF “BLIDA1” SAAD DAHLEB

Faculty of Technology

Institute of Aeronautics and Aerospace Engineering

A THESIS SUBMITTED FOR THE DOCTORAL DEGREE

in Aeronautics

**STUDY AND MODELING AIRCRAFT STRUCTURES UNDER
FOREIGN OBJECT IMPACT (FOI: Bird)**

A Dissertation by

BELKHELFA FATIMA ZOHRA

Date of graduation, 11 July 2021

In front of the jury:

Rezoug Tahar	Professor, University Saad DAHLAB, Blida	President
Boukraa Salah	Professor, University Saad DAHLAB, Blida	Supervisor
Benkhedda Amina	Professor, University Saad DAHLAB, Blida	Examiner
Mahi Amel	Conferences master A, USD, Blida	Guest
Aissani Mouloud	Research master A, RCIT, Algiers	Examiner
Mesrati Nadir	Professor, National polytechnic School, Algiers	Examiner
Nacer Tala-Ighil	Research director, RCIT, Algiers	Examiner

بِسْمِ اللَّهِ الرَّحْمَنِ الرَّحِيمِ

المخلص

هذا العمل مخصص للجانب الصناعي والهدف منه هو تصميم حواف أمامية لهياكل الأجنحة الأفقية و العمودية للطائرة تكون مؤافية تمامًا لشروط الهيئات العالمية للطيران المتعلقة باصطدام الطيور. لقد أظهرت تصميمات الحافة الأمامية المطورة في هذا العمل للأجنحة الخالية من الأضلاع المصنوعة من تكوينات مخففة لمادة الساندويتش مقاومة ناجحة لاصطدام طيور بأوزان 4 و 8 رطل وبسرعة عالية.

خصوصية هذا العمل تكمن في دراسة شاملة لمشكل اصطدام الطيور، والذي يدرج: اصطدام الطيور التفاعل بين الطيور و هيكل الطائرة والاستجابة الديناميكية لهيكل الطائرة أثناء الاصطدام. من أجل فهم كامل لعملية اصطدام الطيور، والتي تتمثل في: مرحلة الصدمة - مرحلة الارتخاء - مرحلة السيلان المستقر - ونهاية الاصطدام، تم دراسة المبادئ الأساسية لعملية اصطدام جسم ناعم تحليليًا ثم رقميًا مما ساعد على تطوير نموذج فعال لاصطدام الطيور. لقد تم تطوير نماذج الاصطدام لأحجام صغيرة وكبيرة من الطيور بتقنية ديناميكا الجسيمات الملساء و تم التحقق من صحة هذه النماذج بالمقارنة مع نتائج الاختبارات التجريبية، أولاً: على لوحة حديدية صلبة مسطحة (باربر 1975 و شاليتا 1979)، ثانياً: على جزء من حافة أمامية لجناح طائرة مضلع مصنوع من مادة مركبة من صفائح معدن الألمنيوم و ألياف الزجاج (قويدا 2009)، ثالثاً: على حافة أمامية لجناح عمودي غير مضلع لطائرة حقيقية مصنوع من مادة ساندويتش مكون أساساً من: قشرة مصنوعة من مادة مركبة، لب مرن من خلايا النحل مصنوع من مادة الألمنيوم، و قشرة داخلية من الألمنيوم (قويدا 2013). لقد تم توسيع هذه المنهجية لإجراء ستة اختبارات اصطدام بواسطة المحاكاة الرقمية باستعمال البرنامج الرقمي ألاس دينا، حيث تم اختبار ثلاث أنواع مختلفة من المواد (معدن بسمك 2.54 مم، مركب من صفائح المعدن و الألياف بسمك 1.4 مم، و ساندويتش بسمك 8.05 مم) في تصميم جزء من حافة أمامية لأجنحة ذات أضلاع وتم تكهن الأضرار الناتجة عن كل اصطدام، حيث استعمل نموذجين اثنين لاصطدام الطيور لكل اختبار مادة، النموذج الأول بوزن 4 رطل و الثاني بوزن 8 رطل و كانت سرعة الاصطدام 129 م/ثا.

في الأخير و بنفس المنهجية و مع أخذ بعين الاعتبار عامل الوزن في تصنيع الأجنحة، تم اختبار اصطدام طيور بوزن 4 و 8 رطل و بسرعة عالية على ثلاث تكوينات مبتكرة لمواد مخففة من الساندويتش في تصميم حافة أمامية لأجنحة طائرة خالية من الأضلاع. التكوين الأول يحوي لب واحد و سمك إجمالي يساوي 7.15 مم، التكوين الثاني يحتوي على لابين و سمك إجمالي يبلغ 13.7 مم، و التكوين الثالث يحوي لابين و سمك إجمالي يصل 13.95 مم، وكان أحد الإنجازات المهمة في هذا العمل هو تلبية هذه التكوينات المطورة لمتطلبات سلامة الطيران.

Abstract

The presented work is dedicated to industrial aspects and its goal designing aircraft leading edge structures that fully comply with bird strike's airworthiness requirements. Designs developed in this work for ribless leading edge configurations made of alleviated compositions of sandwich material have demonstrated successful resistance to bird impact with a nominal weight of 4 lb and 8 lb at high velocity.

The particularity of this work lies in a comprehensive study of the bird impact problem which includes: the bird impact, the interaction between bird and LE, and the dynamic response of the LE structure. For a complete understanding of the full impact process, that comprise: the shock phase- the release phase- the steady state phase- and the termination of impact, the fundamental principles of soft body impact process were first studied analytically, then numerically and this enabled an effective bird impact model development.

SPH impact models for small and large sizes of bird were developed and validated against experimental test results, firstly: on a rigid steel flat plate (Barber 1975 and Challita 1979), secondly: on a FML composite leading edge bay (Guida 2009), and third: on a ribless configuration of a real aircraft leading edge made of sandwich material and principally composed of: FML outer skin- honeycomb flexcore- Aluminum inner skin (Guida 2013). This methodology was extended to perform six numerical impact tests with the help of the finite element code Ls-Dyna, where three material types were tested for the leading edge structure (metal with a thickness of 2.54 mm, a composite fiber metal laminate with a thickness of 1.4

mm, and a sandwich of a thickness of 8.05 mm) and the resultant damage was predicted for each material impact test, where two bird models were used for each material impact testing, the first with 4 lb and the second with 8 lb and the impact velocity was 129 m/s.

Lastly, by the same methodology and taking into account the leading edge weight factor, three different innovative sandwich material configurations for an aircraft ribless leading edge were tested to high velocity impact of 4 lb and 8 lb birds. The first configuration was a single core and had a total thickness of 7.15 mm, the second configuration was a double core and had a total thickness of 13.7 mm, and the third configuration was a double core and had a total thickness of 13.95 mm. The important achievement in this work was the meet of these new developed configurations to the airworthiness requirements.

CONTENTS

ABSTRACT	v
LIST OF FIGURES	xv
CHAPTER 1	
1. INTRODUCTION	3
2. EASA & FAA CERTIFICATION REQUIREMENTS	4
3. FAA REQUIREMENTS CONCERNING BIRD STRIKE TEST	6
4. TECHNIQUE OF MODELING FOR BIRD AVAILABLE IN LS-DYNA	7
4.1. Smoothed Particle Hydrodynamics (SPH) Formulation	8
4.1.1. <i>Kernel approximation</i>	8
4.1.2. <i>Equation of motion</i>	9
4.1.3. <i>Kernel function</i>	10
4.1.4. <i>Variable smoothing length</i>	12
4.2. Sorting	12
4.3. Time Integration	13
4.4. Coupled SPH-Finite Element Method (SFM)	14
4.5. Initial Setup	16
CHAPTER 2	
1. INTRODUCTION TO THE FLUID DYNAMIC NATURE OF BIRD IMPACTS	19
2. FULL ANALYSIS OF THE BASIC PROCESS OF BIRD IMPACT	20
2.1.The Shock Phase	22
2.1.1. <i>The governing equations</i>	22
2.1.2. <i>The development of the shock equation of state for non-porous material</i>	25
2.1.3. <i>The development of the shock equation of state for porous material</i>	26
2.2. The Release Phase	32
2.3.The Steady Flow Phase	35
2.3.1. <i>The development of the steady state equation of state for porous material</i>	40

2.4. The Termination of Impact	42
3. PREDICTION OF THE FLUID PROCESS FOR BIRD IMPACT	43
CHAPTER 3	
1. INTRODUCTION	49
2. TEST DATA FOR SMALL SIZE OF BIRD, 0.163 lb, IMPACTING A FLAT RIGID DISK	49
2. 1. Barber’s Experimental Test Data	49
2.2. Bird Modeling Development	50
2.2.1. <i>Bird model geometry</i>	50
2.2.2. <i>Bird impact material model</i>	52
2.2.3. <i>Bird impact EOS model</i>	53
2.3. Finite Element Flat Disk and Transducers Modeling	54
2.4. The Contact Modeling	55
2.5. Validation of the Small Bird, 0.163 lb, Impact Model on a Rigid Flat Disk	55
3. TEST DATA FOR LARGE SIZES OF BIRD, 4 lb & 8 lb, IMPACTING A FLAT RIGID PLATE	58
3.1. CHALLITA’s Experimental Test Data	58
3.2. Finite Element Modeling	59
3.3. Validation of the 4 lb and 8 lb Bird Impact Models on a Rigid Flat Plate	59
4. BIRD IMPACT SCENARIOS ON RIGID FLAT AND HIGHLY CURVED CONFIGURATIONS	63
5. TEST DATA FOR LARGE SIZES OF BIRD, 4 lb, IMPACTING A DEFORMABLE LEADING EDGE BAY WITH RIBS	66
5.1. GUIDA’s Experimental Test Data for Large Sizes of Bird (4 lb) Impacting a Composite FML Leading Edge Bay	66
5.2. Finite Element Modeling of the Composite FML Leading Edge Bay	67
5.3. Prediction of the Bird Impact Scenario on the Composite FML LE Bay	68
5.4. Validation of the 4 lb Bird Impact Model on a Composite FML Leading Edge Bay	68

6. TEST DATA FOR LARGE SIZES OF BIRD, 8 lb, IMPACTING A C27J AIRCRAFT TAILCONE LEADING EDGE MADE OF SANDWICH FML MATERIAL	70
6.1. GUIDA’s Experimental Test Data	70
6.2. FE Modeling of the Ribless Sandwich FML Leading Edge	71
6.3. Prediction of the Bird Impact Scenario on the Ribless Sandwich FML Leading Edge	71
6.4. Validation of the 8 lb Bird Impact Model on the Ribless Leading Edge	73
 CHAPTER 4	
I. INTRODUCTION TO SANDWICH STRUCTURES	77
I.1. FML Facing Sheet	79
<i>I.1.1. GLARE: Glass Reinforced Aluminum Laminate</i>	80
<i>I.1.2. GLARE Benefits for Aeronautical Applications</i>	82
<i>I.1.2.1. Fatigue crack growth</i>	82
<i>I.1.2.2. Residual strength</i>	83
<i>I.1.2.3. Fire burn-through</i>	83
<i>I.1.2.4. Impact damage</i>	83
<i>I.1.2.5. Blast loading</i>	84
<i>I.1.2.6. Inspection-Maintenance</i>	84
I.2. Honeycomb Core	85
<i>I.2.1. Honeycomb Manufacturing Process</i>	86
<i>I.2.2. Honeycomb Core Cells Configurations</i>	88
<i>I.2.2.1. Flex-Core cell configuration</i>	88
<i>I.2.3. Honeycomb Mechanical Properties and Test Methods</i>	89
<i>I.2.3.1. Compressive Properties</i>	89
<i>I.2.3.2. Crush Strength</i>	90
<i>I.2.3.3. L and W Shear Properties</i>	90
 II. NUMERICAL TEST OF BIRD IMPACT ON SMALL SCALE OF A LEADING EDGE	91
II.1. Test Article Description	91
II.2. FE Model, Material Model & Constitutive Law	92
<i>II.2.1. Metallic Configuration</i>	93
<i>II.2.2. FML Configuration</i>	93

<i>II.2.3. Sandwich -FML Flexcore Configuration</i>	95
<i>II.2.3.1. FML outboard skin</i>	96
<i>II.2.3.2. Aluminum flexcore honeycomb</i>	96
<i>II.2.3.3. Aluminum inboard skin</i>	98
II.3. Results & Discussions	99
<i>II.3.1. Bird Impact on Metallic LE Bay</i>	99
<i>II.3.2. Bird Impact on Composite (FML) LE Bay</i>	101
<i>II.3.3. Bird Impact on Sandwich FML LE Bay</i>	103
III. BIRD IMPACT ONTO REAL AIRCRAFT RIBLESS SANDWICH FML LEADING EDGE STRUCTURE	106
III.1. Finite Element Model of the C27J Aircraft Leading Edge	107
III.2. Results & Discussions	108
IV. BIRD IMPACT ONTO INNOVATIVE MATERIAL CONFIGURATIONS OF AN AIRCRAFT RIBLESS LEADING EDGE	110
IV.1. The Sandwich Metallic Configuration With Simple Core	110
IV.2. The Sandwich Metallic Configuration With Double Core	110
IV.3. The Sandwich Glare Configuration With Double Core	110
IV.4. Results & Discussions	111
V. CONCLUSIONS	120
REFERENCES	122

LIST OF FIGURES

CHAPTER 1

Figure.1.1. Statistical impact distribution on an aircraft (source: Airbus).....	4
Figure 1.2. Particle neighborhood for SPH particle j	9
Figure 1.3. Cubic B-spline kernel function for 3D	11
Figure 1.4. Neighbor search particles inside a $2h$ radius sphere	13
Figure 1.5. Integration cycle in time of the SPH computation process	13
Figure 1.6 Lagrangian code structures for SPH particles and FEM elements	14
Figure 1.7 SFM: linking between the finite elements and SPH particles	15
Figure 1.8 SFM: sliding contact between the finite elements and SPH particles	16
Figure 1.9. Cylinder SPH mesh possibilities	16

CHAPTER 2

Figure 2.1. The phases of bird impact (<i>a</i>) initial impact (<i>b</i>) impact decay (<i>c</i>) steady flow (<i>d</i>) termination	21
Figure 2.2. One dimensional shock flow	22
Figure 2.3. Compressibility effect on the Hugoniot pressure for water	23
Figure 2.4. Obliquity effect on the Hugoniot pressure for water	24
Figure 2.5. Shock Hugoniot for air	27
Figure 2.6. Porosity effect on the Hugoniot shock for water	29
Figure2.7. Pressure vs. volume relationship across a shock compression for water with various porosity	29
Figure 2.8. Porosity effect on the shock velocity for water	30
Figure 2.9. Hugoniot Pressure-volume* 100 relationships for water with various porosities, for pressures up to 500 MN/m^2 (5 kbar)	30
Figure 2.10. Hugoniot Pressure-volume relationships for water with various porosities, for pressures up to 20 MN/m^2	31
Figure. 2.11 . Hugoniot Shock pressures measured during normal impact of birds.....	31
Figure 2.12. Shock and release waves in fluid impact	32
Figure 2.13. Duration of the Hugoniot pressure vs. impact velocity for a cylindrical impact of water	33
Figure 2.14. Comparison of the shock velocity, u_s , and the sound speed in the shocked region, c_r	33
Figure 2.15. Duration for which the pressure will rapidly decay, t_c , vs. impact velocity for a cylinder impact of water (a , is the initial radius of the cylinder)	34
Figure 2.16. Variation of the critical length vs. impact velocity for water	35
Figure 2.17. Steady flow	36
Figure 2.18. Compressibility effects on stagnation pressure in steady flow for a cylinder impact of water	37

Figure 2.19. Compressibility effects on the radial distribution of steady flow pressure for the normal impact of a water jet	38
Figure 2.20. Steady flow pressure distribution vs impact velocity (m/s) of 0.060 Kg bird along major axis for normal impact [79]	39
Figure 2.21. Steady flow pressure distribution vs impact velocity (m/s) of 0.060 Kg bird along major axis at 45 °, for oblique impact [79]	39
Figure 2.22 . Porosity effect on the isentropic pressure for water	41
Figure 2.23. Isentropic pressure-volume relationships for water with various porosities, ($P < 500 \text{ MN/m}^2$)	41
Figure 2.24. Isentropic pressure-volume relationships for water with various porosities, ($P < 20 \text{ MN/m}^2$)	42
Figure 2.25. Pressure vs. volume relationship across an isentropic compression for water...42	42
Figure 2.26. Total duration of impact for different weight of a cylinder of water with 10% of porosity	43
Figure 2.27. SPH impact model of a cylinder of water with 10% of porosity on a rigid plate.....45	45
Figure 2.28. Hugoniot shock pressure for water with 10% of porosity	45
Figure 2.29. Isentropic pressure at the stagnation point for water with 10% of porosity.....46	46

CHAPTER 3

Figure 3.1. SPH bird model with cylindrical shape, $L/D=2$	51
Figure 3.2. SPH bird model with hemispherical shape, $L/D>2$	51
Figure 3.3. SPH bird model with hemispherical shape, $L/D =2$	52
Figure 3.4. Plot of the shock pressure for water with 10% of porosity versus the impact velocity	54
Figure 3.5. Plot of the shock pressure for water with 10% of porosity versus volumetric strain, $P= f(\epsilon_V)$, Tabulated EOS type 9	54
Figure 3.6. Bird impact scenarios on the rigid plate at 198 m/s	56
Figure 3.7. Plot of the contact force (N) vs time (s)	56
Figure 3.8. Transducers" B" and "C" modeling	57
Figure 3.9. Transducer B: resultant contact force	58
Figure 3.10. Transducer C: resultant contact force	58
Figure 3.11. Normal impact model of 4lb bird and oblique impact model of 8lb bird, onto a rigid flat plate	60
Figure 3.12. Normal 4 lb bird impact scenario on the rigid plate at 298 m/s	60
Figure 3.13. Plot of the contact force (N) vs time (s) for normal 4lb impact (90°)	61
Figure 3.14. Oblique 4 lb bird impact scenario on the rigid plate at 104 m/s	61
Figure 3.15. Plot of the contact force (N) vs time (s) for oblique 4 lb impact (45°).....61	61
Figure 3.16. Normal 8 lb bird impact scenario on the rigid plate at 245 m/s.....61	61
Figure 3.17. Plot of the contact force (N) vs time (s) for normal 8 lb impact (90°).....62	62
Figure 3.18. Oblique 8 lb bird impact scenario on the rigid plate at 115 m/s.....62	62
Figure 3.19. Plot of the contact force (N) vs time (s) for oblique 8lb impact (45°).....62	62

Figure 3.20. Different views of the bird impact on a rigid flat plate at 129 m/s	64
Figure 3.21. Different views of the bird impact scenario onto a rigid leading edge bay at 129 m/s	65
Figure 3.22. The arrangement of the test [82].....	66
Figure 3.23. View the leading edge bay [30].....	67
Figure 3.24. Finite element model of the LE bay	68
Figure 3.25. Bird impact scenario onto a deformable FML leading edge bay at 129 m/s.....	69
Figure 3.26. Numerical al results obtained for the impact of 4lb bird onto the FML LE bay at 129 m/s	70
Figure 3.27. Experimental results for the impact of 4lb bird onto the FML LE bay at 129 m/s [22]	70
Figure 3.28. View of a model of real C27J aircraft leading edge [82]	70
Figure 3.29. View of the finite element model of the ribless C27J leading edge	71
Figure 3.30. bird impact scenario onto real C27J aircraft leading edge at 129 m/s, made of sandwich FML material	72
Figure 3.31. Final shape of the ribless sandwich FML LE after the 8 lb bird impact at 129 m/s.....	72
Figure 3.32. Differents views of the ribless sandwich FML LE after the 8 lb bird impact at 129 m/s	73
Figure 3.33. Ribless sandwich FML LE after impact of 8 lb bird at 129 m/s, Exp [82].....	73
Figure 3.34. Front view of the ribless sandwich FML LE after the 8 lb bird impact at 129 m/s.....	73
Figure 3.35. Time history (ms) of the central node displacement (mm) on the upper skin of the ribless LE.....	73

CHAPTER 4

Figure.4.1. Schematic representation of a sandwich structure	77
Figure. 4.2. Sandwich structure failure modes [92].....	78
Figure 4.3. Composite sandwich applications in A380 [93].....	79
Figure 4.4. A typical fiber metal laminate	80
Figure 4.5. Structure of GLARE	81
Figure 4.6. Schematic of the fatigue-crack growth mechanism in GLARE [99].....	82
Figure 4.7. Theoretical behavior of honeycomb cell in compression	86
Figure 4.8. Expansion manufacturing process for honeycomb material.....	87
Figure 4.9. Corrugated manufacturing process for honeycomb material	87
Figure. 4.10. Honeycomb density [112].....	88
Figure 4.11. Bellshaped core, or flex-core honeycomb.....	88
Figure 4.12. Compressive test	89
Figure 4.13. General honeycomb initial compressive stress- strain curves	89
Figure 4.14. Typical load-deflection curve	90
Figure 4.15. Tensile plate shear	91

Figure 4.16. One bay leading edge specimen	92
Figure 4.17. Finite element model of the LE	93
Figure 4.18. Unit cell of F40- 0.0019- 5052- 3.1 pcf honeycomb	96
Figure 4.19. Effective stress (Kg/mm.s ²) of a single cell of the flexcore honeycomb F40- 0.0019-5052 under dynamic out of plane compression with a velocity of 129 m/s.....	98
Figure 4.20. 4lb bird striking onto Al 6013 T6 Alloy LE bay with a velocity of 129 m/s.....	99
Figure 4.21. 8 lb bird striking onto Al 6013 T6 Alloy LE bay with a velocity of 129 m/s...99	99
Figure 4.22. V.M stress distribution of, (a) 4lb, (b) 8lb, bird striking onto Al 6013 T6 LE bay with a velocity of v= 129 m/s.....	100
Figure 4.23. 4lb bird striking onto composite FML LE with a velocity of 129 m/s.....	101
Figure 4.24. 8lb bird striking onto composite FML LE with a velocity of 129 m/s.....	101
Figure 4.25. V.M stress distribution of, (a) 4lb, (b) 8lb, bird striking onto FML LE bay with a velocity of v= 129 m/s.....	102
Figure 4.26. 4 lb bird striking onto sandwich FML LE bay with a velocity of 129 m/s.....	103
Figure 4.27. 8lb bird striking onto sandwich FML LE bay with a velocity of 129 m/s.....	103
Figure 4.28. V.M stress distribution of, (a) 4lb, (b) 8lb, bird striking onto sandwich FML LE bay with a velocity of v= 129 m/s	104
Figure 4.29. Alenia C27 J Spatran aircraft	106
Figure. 4.30. Ribless leading edge	107
Figure 4.31. FE view of the ribless leading edge.....	108
Figure 4.32. 4 lb bird and 8 lb bird impact onto ribless sandwich FML LE at 129 m/s.....	108
Figure 4.33. 3D views of the ribless sandwich FML LE after 4 lb and 8 lb bird impacts at 129 m/s.....	108
Figure 4.34. Font views of the ribless sandwich FML LE after 4 lb and 8 lb bird impacts at 129 m/s (the 8lb bird impact test on the S.FML. LE has bee already validated in Chapter 3).....	109
Figure 4.35. Up views of the ribless sandwich FML LE after 4 lb and 8 lb bird impacts at 129 m/s	109
Figure 4.36. 4 lb bird and 8 lb bird impact onto the three differents configuration of the ribless LE at 129 m/s	111
Figure. 4.37. 3D view of three configurations of the ribless LE after 4 lb and 8 lb bird impacts at 129 m/s	112
Figure. 4.38. Front view of three configurations of the ribless LE after 4 lb and 8 lb bird impacts at 129 m/s	113
Figure. 4.39. Up view of three configurations of the ribless LE after 4 lb and 8 lb bird impacts at 129 m/s	113
Figure 4.40. Plot of the different energies for the 8 lb impact at 129 m/s on the S. FML. 1C.LE.....	115
Figure 4.41. Plot of the different energies for the 8 lb impact at 129 m/s on the S. MTL. 1C.LE.....	116
Figure 4.42. Plot of the different energies for the 8 lb impact at 129 m/s on the S. MTL.2C. LE.....	116
Figure 4.43. Plot of the different energies for the 8 lb impact at 129 m/s on the S. GLR.2C. LE	117

List of Symbols

FAA: American Federal Aviation Administration
FAR: U.S. Federal Aviation Regulations
EASA: European Aviation Safety Agency
CS: Certification Specifications
CFR: Code of Federal Regulations
 $f(\mathbf{x})$: function
 Ω : sub-domain of influence
 W : is an interpolating kernel
 \mathbf{x} : 3-D position vector
 $d\mathbf{x}'$: volume element
 h : smoothing length
 $h^2 \nabla^2 f$: accuracy order
 N : set of discrete interpolation points
 i and j : represents the particle number
 \mathbf{x}_i : centroid of the particle i
 \mathbf{x}_j : centroid of the particle j
 m_j : mass associated with particle j
 ρ_j : density associated with particle j
 $\nabla \cdot f(\mathbf{x})$: spatial gradient of the kernel approximation
 $\nabla \cdot \mathbf{v}$: divergence of velocity
SPH: Smooth particles hydrodynamics
 ξ : dimension of the problem
 κ : scalar factor to comply with Eq. (1.1)
 M : total mass of n particles inside a sphere of radius $2h$
 δt : time step
 C_{CFL} : a numerical constant
FEM: finite element method
SFM: coupled SPH-FEM
 $\Delta \mathbf{x}_i$: lengths parameter
CSLH: coefficient applied to the smoothing length of the particles
 (1) : subscript refers to parameters in the region in front the shock
 (2) : subscript refers to parameters in the region behind the shock
 P_H : Hugoniot pressure
 \mathbf{u}_s : velocity of the shock propagating into the fluid
 \mathbf{u}_p : velocity of the particles behind the shock
 \mathbf{u}_0 : velocity of impact
 c_0 : isentropic wave speed in the material
 k : a constant for the material
 α : impact angle of obliquity
 p : subscript refers to the cylinder properties

t : subscript refers to the target properties
 A and B : material constants
 q : particle velocity and shock velocity ratio
 ρ_z : average density of the soft body material with porosity
 ρ_f : full density of the soft body material (density without porosity)
 z : term represents the volume fraction of air
 $1 - z$: represents the volume fraction of the soft body material
 ρ_{AVG} : average density of the mixture
 $f v_i$: volume fraction of the i^{th} constituent
 ρ_i : density of the i^{th} constituent
 t_B : duration of the shock pressure at the center of impact
 a : initial radius of the cylinder
 c_r : velocity of the initial release wave
 t_c : time that it takes the front of the release wave to just capture all of the shock wave
 L_c : critical cylinder length
 $(L/D)_c$: nondimensional critical cylinder length
 P : pressure at any point in the steady flow field
 u : velocity at a point in the steady flow field
 P_0 : atmospheric pressure
 P_s : stagnation pressure
 K'' : constant along the streamline
 F : force generated in the steady flow regime
 A : impact surface
 r : radial distance from the center
 ζ_2 : is a constant in the Leach and Walker expression
 γ : ratio of specific heats
 t_D : total duration of the impact
 ρ_b : bird density in kg/m^3
 W_b : weight of the bird in Kg
 D : bird diameter in m
 V_b : bird volume
 L : total length of the bird
EOS : equation of state

CEROD : erosion in compression
TEROD : erosion in tension
C : represents the function or constants array
T : temperature which depends on volumetric strain
 ϵ_V : volumetric strain
E : internal energy
SPC: single point constraint defined as boundary conditions
LE : leading edge
t : numerical impact duration
A, B, C : transducers positions
FML : fiber metal laminate
Al : aluminum
CNRB : constrained nodal rigid body
ARALL : aramid reinforced aluminum laminate
GLARE : glass reinforced aluminum laminate
CARALL : reinforced aluminum laminate
L : dimension in the ribbon direction
W : dimension in the transverse direction of the ribbon
FE : finite element
 ρ : material density
E : Young's modulus
 ν : Poisson's ration
 σ_y : yield stress
 E_t : tangent modulus
 S_1 : longitudinal tensile strength
 S_2 : transverse tensile strength
 S_{12} : shear strength
 C_2 : transverse compressive strength
 α : nonlinear shear stress parameter
 $\bar{\tau}$: fiber matrix shearing term
 F_{matrix} : matrix cracking failure criteria
 F_{comp} : compression failure criteria
 F_{fiber} : fiber breakage criteria
V : relative volume
 v : element volume
 v_f : volume of the fully compacted element
 E^{com} : compression modulus in the fully compacted phase
 E_{ii}^{un} and G_{ij}^{un} : compression and shear moduli in the not compacted phase

μ : Poisson's ratio

V_f : relative volume of fully compacted brick element

$\Delta\epsilon_{ij}$: strain increment

n : time increment.

S_{ij} : honeycomb stresses in th fully compacted phase

$\Delta\epsilon_{ij}^{dev}$: deviatoric strain increment

β : scale factor of the yield stress

D and p : Cowper-Symonds [Jones 1983] coefficients

$\dot{\epsilon}$: strain-rate

CHAPTER 1

BIRD STRIKE
AIRWORTHINES
S
REQUIREMENTS

1. INTRODUCTION

Aviation companies register significant losses, especially, when a tragic accident occurs to an aircraft. One of the main causes of such accident is bird strikes. Bird strikes are defined as a collision between a bird and an aircraft which is in flight or on a take-off or landing roll [1]. As of 11 November 2019, bird strikes were determined to have caused 618 hull losses and 534 fatalities since the beginning of aviation [2]. Examples of hazards caused by these foreign objects are: the accident occurred in 1962, in which a Vickers Viscount turboprop airplane operated by a U.S. airline crashed with no survivors near Chesapeake, Maryland after impacting with a swan [3]. Another example is the accident occurred in January 2009 to the aircraft engine of Airbus A320 of US Airways, where the aircraft ditched into Hudson River in New York after experiencing loss of both turbines after an engine ingestion of at least two Canadian geese [4]. A similar accident occurred in August 2019, and took place in Moscow when the crew of an Airbus A321 performed a successful emergency landing in a corn field after the engines failed due to ingestion of multiple gulls during departure [5], all passengers and crew survived.

Bird strikes hit the large front-components of the aircraft, i.e. the nose (windshield, window frame, radome and forward fuselage skin), the leading edges of the wings and empennage, as well as the engines (fan blades and inlet) (Fig.1.1). Therefore the aviation authorities require that all forward facing components need to prove a certain level of bird strike resistance in certification tests before they are allowed for operational use. These requirements are defined by the American Federal Aviation Administration (FAA) within the U.S. Federal Aviation Regulations (FAR) and by the European Aviation Safety Agency (EASA) within the Certification Specifications (CS).

The typical method of bird-proof design of aircraft components is to build and test, then redesign and test again. This procedure is not only very time-consuming, but also costly and difficult to perform. Therefore, numerical simulations are becoming a fundamental design tool that satisfies both time and costs. Since the late eighties, explicit finite element codes have been used to develop high efficiency bird-proof structures. These codes adopted various finite element methods to model the impact phenomena: the Lagrangian, the Eulerian, the Arbitrary Lagrangian Eulerian (ALE), and recently solvers based on the Smoothed Particle Hydrodynamics (SPH).

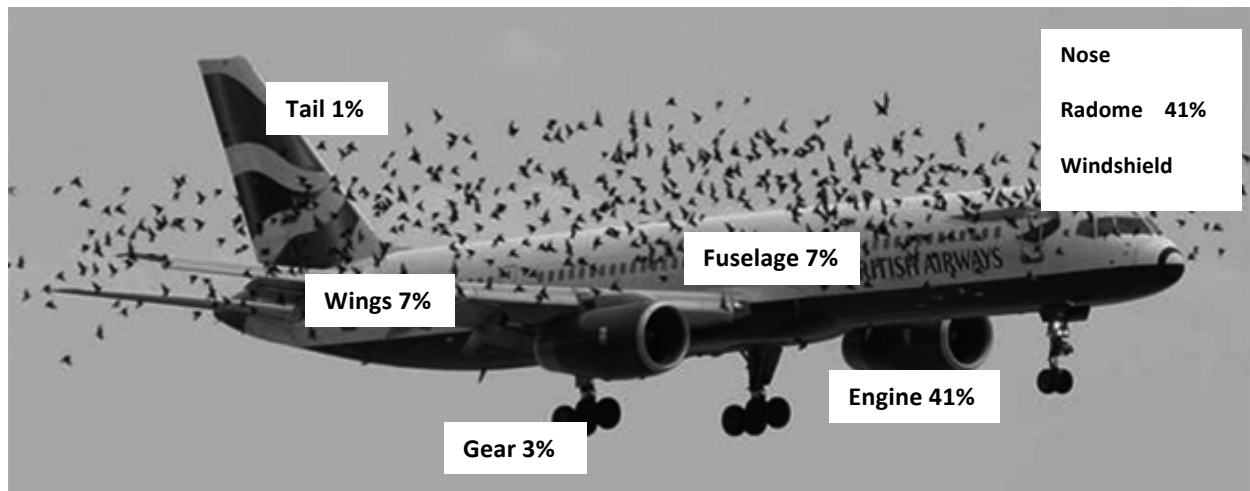


Figure.1.1. Statistical impact distribution on an aircraft (source: Airbus)

2. EASA & FAA CERTIFICATION REQUIREMENTS

Aircraft have to meet certification requirements to prove their airworthiness [6]. Depending on their size, aircrafts are grouped into categories. Airplanes used for commercial aviation are either in the category Normal (EASA)/Normal Category Airplanes (FAA) or Large Aeroplanes (EASA)/Transport Category Aircraft (FAA). The categories and their descriptions, which are mostly corresponding, can be found in Table 1.1. By 2014, approximately 97% of aircraft in the worldwide commercial fleet were certified as Large Aeroplanes/Transport Category Aircraft; the remaining 3% were certified as Normal/Normal Category Airplanes.

Table 1.1. Certification categories relevant for commercial aviation aircraft in Europe and the US (**CS**: Certification Specifications; **CFR**: Code of Federal Regulations).

Europe- EASA	US- FAA
CS-23 Normal Aeroplanes aeroplanes with a passenger-seating configuration of 19 or less and maximum certified take-off mass of 8618 kg (19000 lbs) or less [7]	14 CFR Part 23 Normal Category Airplanes airplanes with a passenger-seating configuration of 19 or less and a maximum certificated take-off weight of 19000 lbs or less [8]
CS-25 Large Aeroplanes turbine-powered aeroplanes of more than 5700 Kg (12500 lbs) maximum certified take-off weight, excluding commuter airplanes which are covered by the category Normal Aeroplanes [9,10]	14 CFR Part 25 Transport Category Aircraft multi-engine airplanes with more than 19 seats or a maximum take-off weight greater than 19000 lbs [11]

In Europe, the majority of commercial aircrafts are certified by the standard CS 25—Large Aeroplanes. The US-American counterpart consists of the Federal Aviation Regulations

(FAR) 14 CFR Part 25—Transport Category Airplanes. These regulations contain the following requirements regarding damage-tolerance of aircraft components.

- **Windshield:** withstand without penetration an impact of a 4 lb bird at cruise speed.
- **Structure:** Successfully completing a flight after an impact with a 4 lb bird when the aircraft's velocity relative to the bird along the aircraft's flight path equals cruise speed at sea level or 0.85 cruise speed at 8000 ft, whichever is more critical.
- **Empennage:** Successfully completing a flight after an impact with an 8 lb bird at cruise speed (FAA only).
- **Pitot tubes:** sufficient separation to prevent damage to all of them in case of a bird strike.

Aircraft in the category *CS 23–Normal Aeroplanes* respective *14 CFR Part 23—Transport Category Airplanes* only have to prove an impact-resistance of the windshields. Both the European and the US regulations demand that *each windshield and its supporting structure directly in front of the pilot must withstand, without penetration, the impact equivalent to a two-pound bird when the velocity of the aeroplane is equal to the aeroplane's maximum approach flap speed.* [7,8]. Consequently, category 23 aircraft are more vulnerable to damage due to collisions with birds.

Regarding the impact-resistance of engines, which have to be certified independently of the aircraft, separate EASA and FAA regulations are in force. To prove that an engine responds in a safe manner to bird ingestion, it must undergo an engine ingestion test. The European regulations (CS-E 800 [12]) demand tests considering the ingestion of single large birds and large flocking birds. The FAR add tests for small and medium single and flocking birds [13]. Depending on the engine's diameter, different criteria regarding bird mass and thrust settings are required. In all tests, the ingestion of the bird must not lead to a hazardous engine effect. EASA defines the following events as Hazardous Engine Effects [12]:

1. non-containment of high-energy debris,
2. concentration of toxic products in the engine bleed air for the cabin sufficient to incapacitate crew or passengers,
3. significant thrust in the opposite direction to that commanded by the pilot,
4. uncontrolled fire,
5. failure of the engine mount system leading to inadvertent engine separation,
6. release of the propeller by the Engine, if applicable,
7. complete inability to shut the engine down.

3. FAA REQUIREMENTS CONCERNING BIRD STRIKE TEST

Bird strike tests are done in accordance with FAR Parts 25 and 33. These tests once involved the shooting of a live chicken (real bird) of appropriate weight at the article to be certified. It is easy to imagine that the cleanup effort following each test was substantial. For simplicity, sanitary, aesthetic, and repeatability reasons, it is now permitted to use cleaned and dressed chickens instead of live birds.

- ***A typical windshield test program*** involves several bird shots at various points on each windshield and frame. The goal is to show that pilots will not be injured by the bird, windshield fragments, or broken airframe or interior parts; and that the damaged structure and windshield will continue to hold cabin pressure following a bird strike event. High speed cameras (10,000 –20,000 frames per second) are placed inside and outside the cockpit to capture the details of any failure. At actual playback speeds, the outside video of a successful bird shot shows nothing but sabot fragments fluttering down and some condensation vapor emanating from the cannon. At slow playback speeds, the replay shows the fluid behavior of the bird, high local deflections of the windshield, and rather large amplitude impact waves and reflections rippling throughout the forward fuselage.
- **Wing shots;** are targeted at inboard and outboard leading edges. The typical goal is to show that the bird does not penetrate the main load-carrying spars and no fuel cells are damaged so as to cause fuel leakage. Splitter plates (in the form of a span-wise triangular box) are often placed inside the leading edge skins to deflect the bird and reinforce the leading edge structure.
- ***Empennage shots;*** are targeted at several span-wise locations along the leading edges of the vertical fin and stabilizer, where vulnerabilities resulting from impact damage are expected to be the highest. The typical goal of these tests is to show that the bird does not penetrate the main load-carrying spars. Similar to wing leading edges, the empennage leading edges often contain splitter plates inside the skins to deflect the bird and to reinforce the leading edge structure.
- ***Engine bird strike tests;*** include the investigation of the damage effects on engine operations as well as on fan disk integrity. Engine operation tests must show that the engine will continue to produce at least 75% thrust for 5 minutes after ingesting a flock of small or medium weight birds. Fan integrity tests must demonstrate that the engine does not catch fire or disintegrate after being struck by a single, 4 lb bird.

4. TECHNIQUE OF MODELING FOR BIRD AVAILABLE IN LS-DYNA

Finite element simulations may incorporate various solution strategies such as the following: pure Lagrangian approach, and Smooth Particle Hydrodynamics (SPH) approach. Each of these numerical techniques has distinct advantages and disadvantages. In the Lagrangian formulation, however, the mesh is embedded in the structure; and as the structure distorts, the mesh undergoes undesirable distortions that negatively affect the accuracy of the results, especially when used in problems such as bird strike analysis where the bird undergoes severe distortions. Very well known negative volume errors and hourglass modes occur due to the mesh entangling.

Smoothed Particle Hydrodynamics (SPH) is a meshless formulation, and thus completely avoids the problems such as element distortions and hourglass modes. SPH is based on Lagrangian formulation, and is developed initially for astrophysical problems [14 - 16]. In the SPH formulation, the bird is discretized into large number of interacting masses. Since it is based on Lagrangian formulation, it allows for efficient tracking of material deformations and history dependent behavior. The main drawback of the SPH model is its relatively high CPU times; however, it is highly robust numerically. SPH is more efficient than the Euler mesh because only the region where the material exists at the current time is modeled; and at the same time it does not suffer from mesh distortions like a pure Lagrangian mesh, since SPH is mesh-less.

The first adoption of the SPH method for bird strike simulations is documented in the late 1990s and early 2000s [17,18,19], where this approach was implemented in the code PLEXUS and used for fan blade impact studies. References [20,21,22,23–26,27,28,29,30,31–33,34,35–48] used the SPH approach in LS-DYNA and PAMCRASH for bird strike investigations on leading edges and highlight the increased stability, good potential of bird splitting and reduced cost of the simulations compared to Lagrangian bird impactors. SPH bird impactors for impact on fan blades are documented in [49,50,24,51–53], for impact on engine nacelles in [54], on a windscreen in [55,56], on composite plates in [21,34, 39], on wing flaps in [57], on an aircraft radome in [58], on wing pod and belly pod nose in [48] and on a helicopter rotor blade in [59].

Because of its advantages, the SPH technique is chosen for the spatial discretization of the bird model of the presented work. Consequently, the foundation of the methodology for the Smoothed Particle Hydrodynamics (SPH) technique is presented below.

4.1. Smoothed Particle Hydrodynamics (SPH) Formulation

Smoothed Particle Hydrodynamics (SPH) is an N-body integration scheme developed by Lucy, Gingold and Monaghan [1977]. The method was developed to avoid the limitations of mesh tangling encountered in extreme deformation problems with the finite element method.

In the SPH method, the continuum is treated as a random set of particles that interact with each other. The particles are the computational framework on which the governing equations are resolved. This new model requires a new calculation method. SPH is a technique that has foundations in the interpolation theory, and allows any function to be expressed in terms of the values of the same function at a set of disordered points that makeup the continuum [16]. Spatial derivatives of various field variables are computed using kernel estimates, in the absence of regular connectivity between the particles found in methods that use a mesh.

4.1.1. Kernel approximation

The integral representation or kernel approximation of a function $f(\mathbf{x})$ over a compact sub-domain of influence, Ω , and its divergence can be expressed as

$$f(x) = \langle f(x) \rangle = \int_{\Omega} f(x') W(x - x', h) dx' \quad (1.1)$$

$$\nabla \cdot f(x) = \langle \nabla \cdot f(x) \rangle = - \int_{\Omega} f(x') \cdot \nabla W(x - x', h) dx' \quad (1.2)$$

where W is an interpolating kernel or smoothing function, x is the 3-D position vector, dx' is a volume element, and h is the smoothing length. It has been shown that the above approximation has accuracy of the order of $h^2 \nabla^2 f$ [60].

The smoothing kernel function W is similar to a weight function, and must satisfy the following conditions:

- normalized in each sub-domain:

$$\int W(x - x', h) dx' = 1 \quad (1.3)$$

- compact support, i.e.,

$$W(x - x', h) = 0 \quad \text{for } |x - x'| \geq 2h \quad (1.4)$$

- reduces to Dirac-delta function, when $h \rightarrow 0$

$$\lim_{h \rightarrow 0} W(x - x', h) = \delta(x - x') \quad (1.5)$$

The interaction between the random set of particles is weighted by the interpolating kernel W .

For numerical computations, the kernel approximation of $\langle f(x) \rangle$ can be written in terms of arbitrary set (N) of discrete interpolation points as

$$\langle f(x_i) \rangle = \sum_{j=1}^N f_j(x_j) W(x_i - x_j, h) \frac{m_j}{\rho_j} \quad (1.6)$$

where, i and j represents the particle number; x_i , x_j is the centroid of the particle i and j , respectively; m_j and ρ_j are the mass and density associated with particle j , respectively. N is the number of particles that fall within the smoothing length. In the above formulation, each particle is assumed to be a small volume element. Figure 1.2 shows the particle neighborhood for particle j as a circle of radius $2h$. Within this circular neighborhood, it is usually assumed that there is one SPH particle for an approximate spacing of the parameter h .

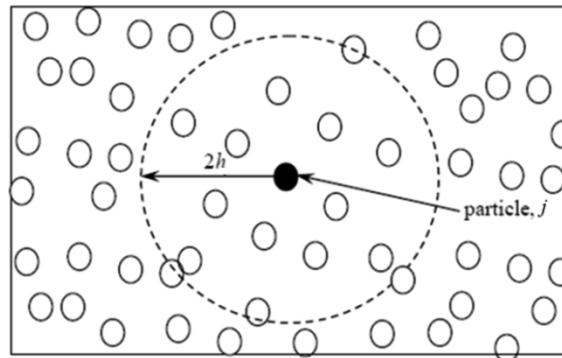


Figure 1.2. Particle neighborhood for SPH particle j

4.1.2. Equation of motion

In the SPH methodology, the spatial gradient of the kernel approximation $\langle \nabla \cdot f(x) \rangle$ is obtained from

$$\langle \nabla \cdot f(x_i) \rangle = - \sum_{j=1}^N f_j(x_j) \cdot \nabla W(x_i - x_j, h) \frac{m_j}{\rho_j} \quad (1.7)$$

However, Monaghan [16] suggests the following form for $\nabla \cdot f(x)$ for improved accuracy:

$$\nabla \cdot f(x) = \frac{1}{\rho} (\nabla \cdot (\rho f) - f \cdot \nabla \rho) \quad (1.8)$$

Note that the above formulation is obtained from the product rule of differentiation.

Similarly, the divergence of velocity $\nabla \cdot v$ can be written as

$$\nabla \cdot v = \frac{1}{\rho} (\nabla \cdot (\rho v) - v \cdot \nabla \rho) \quad (1.9)$$

The discrete kernel approximation of $\nabla \cdot v$, now follows from equation (1.7):

$$(\nabla \cdot v)_i = \frac{1}{\rho_i} \sum_{j=1}^N (v_j - v_i) \cdot \nabla_i W_{ij} \quad (1.10)$$

where $\nabla_i W_{ij}$ refers to the gradient of W taken with respect to particle i .

Now, using the definitions presented above, the SPH governing equations can be written [61] as follows:

- Continuity or conservation of mass:

$$\left\langle \frac{d\rho_i}{dt} \right\rangle = \sum_{j=1}^N (v_j - v_i) m_j \cdot \nabla W_{ij} \quad (1.11)$$

- Conservation of linear momentum:

$$\left\langle \frac{dv_i}{dt} \right\rangle = - \sum_{j=1}^N \left(\frac{\sigma_i}{\rho_i^2} + \frac{\sigma_j}{\rho_j^2} \right) m_j \cdot \nabla W_{ij} \quad (1.12)$$

- Conservation of energy:

$$\left\langle \frac{dE_i}{dt} \right\rangle = - \left(\frac{\sigma_i}{\rho_i^2} \right) \sum_{j=1}^N (v_j - v_i) m_j \cdot \nabla W_{ij} \quad (1.13)$$

4.1.3. Kernel function

The value of the interpolating kernel, or the smoothing function W varies in the neighborhood shown in Figure 1.2 of an SPH particle j . The value of W is at its maximum

when $h \rightarrow 0$, and rapidly falls off as the boundary of the neighborhood is approached. In other words, interpolating kernel W has a compact support. The most common interpolating kernel used is the B-spline. The values of W based on the B-spline are

$$W(q, h) = \frac{\kappa}{h^\xi} \begin{cases} \left(1 - \frac{3}{2}q^2 + \frac{3}{4}q^3\right) & q \leq 1 \\ \frac{1}{4}(2 - q)^3 & 1 < q \leq 2 \\ 0 & q > 2 \end{cases} \quad (1.14)$$

where $q = \frac{|x_i - x_j|}{h}$

where, $\xi (= 1, 2 \text{ or } 3)$ is the dimension of the problem and κ is the scalar factor to comply with Eq. (1.1). Three values of κ corresponding to $\xi (= 1, 2 \text{ or } 3)$ are $2/3$, $10/7\pi$ and $1/\pi$, respectively. The 3D cubic B-spline kernel function $\xi = 3$, $h=1$ and $\kappa = 1/\pi$ is demonstrated in Figure 1.3.

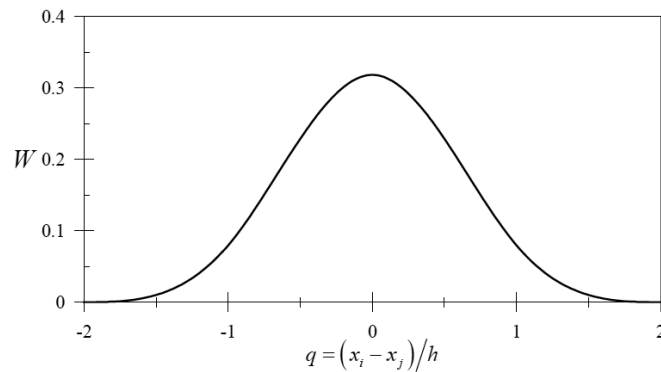


Figure 1.3. Cubic B-spline kernel function for 3D

Derivatives of the cubic B-spline kernel function are shown as:

$$\frac{dW}{dq} = \frac{\kappa}{h^\xi} \begin{cases} 3\left(-q + \frac{3}{4}q^2\right) & q \leq 1 \\ -\frac{3}{4}(2 - q)^2 & 1 < q \leq 2 \\ 0 & q > 2 \end{cases} \quad (1.15)$$

$$\frac{d^2W}{dq^2} = \frac{\kappa}{h^\xi} \begin{cases} 3\left(-1 + \frac{3}{2}q\right) & q \leq 1 \\ \frac{3}{2}(2 - q) & 1 < q \leq 2 \\ 0 & q > 2 \end{cases} \quad (1.16)$$

Smoothing length h varies during the course of a computation to ensure the availability of enough particles in the neighborhood of SPH particle j . Smoothing length h is a function of spatial dimension and time. It is computed from

$$\frac{dh}{dt} = \frac{1}{h} \nabla \cdot v \quad (1.17)$$

4.1.4. Variable smoothing length

In order to avoid problems related with expansion and compression of material, a variable smoothing length presents a best solution. W. Benz developed the concept of a variable smoothing length. The main idea of this concept is that it is necessary to keep enough particles in the neighborhood to validate the approximation of continuum variables. The smoothing is allowed to vary in time and space. For a constant smoothing length, a material expansion can lead to numerical fracture and a material compression can slow down the calculation significantly.

The mass has to be kept constant in the neighborhood (space). The total mass M of n particles inside a sphere of radius $2h$ is:

$$M = n \cdot m = n \cdot (\rho V) = n \cdot \rho \cdot \frac{4}{3} \pi 8h^3 \quad (1.18)$$

Then we have the time rate of change of the mass:

$$\frac{dM}{dt} = n \cdot \frac{d\rho}{dt} \cdot \frac{32}{3} \pi h^3 + n\rho \frac{32}{3} \pi \frac{dh^3}{dt} \quad (1.19)$$

Since the mass is constant in time, the left hand of the equation is equal to zero. Thus the equation is simplified to:

$$\frac{dh}{dt} = \frac{1}{3} \bar{h} \nabla \cdot V \quad (1.20)$$

Due to computational efficiency a minimum of 0.2 times the initial smoothing length and a maximum value for the smoothing length twice the initial smoothing length are required. The value of the smoothing length is then between those minimum and maximum values.

4.2. Sorting

In LS-Dyna, A bucket sort algorithm is used to accomplish the neighboring search task. The sorting consists of finding which particles interact with which others at a given time. the bucket sort consists of partitioning the domain into boxes where the sort is

performed. With this partitioning the closest neighbors will reside in the same box or in the closest boxes. This method reduces the number of distance calculations and therefore the CPU time. A scheme of this neighbor search is shown in Fig. 1.4 (Lacome, 2001).

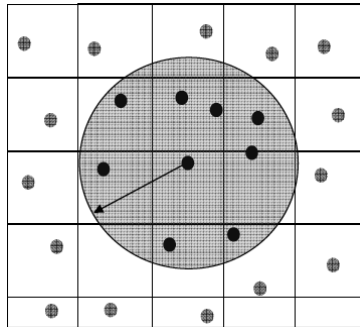


Figure 1.4. Neighbor search particles inside a $2h$ radius sphere

4.3. Time Integration

The SPH formulation was integrated into the LS-Dyna code by Lacome [61]. Figure 1.5 illustrates an integration cycle in time of the SPH computation process. Neighbor search is an important part of the SPH formulation. It is important to know which particle will interact with its neighbors because the interpolation depends on these interactions. The influence of a particle is established inside of a sphere of radius of $2h$, where h is the smoothing length. In the neighboring search, it is also important to list, for each time step, the particles that are inside that sphere. If we have N particles, then it is required $(N-1)$ distance comparison. If this comparison is done for each particle, then the total amount of comparisons will be $N(N-1)$.

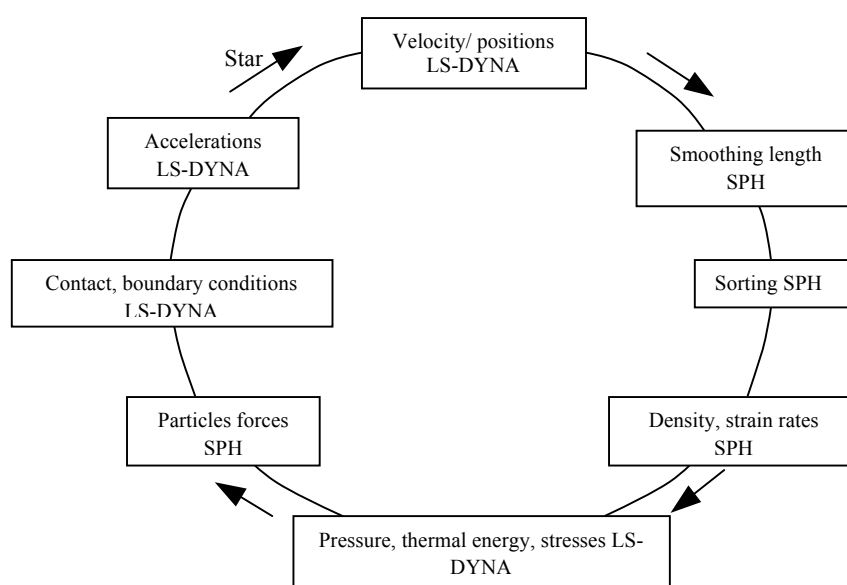


Figure 1.5. Integration cycle in time of the SPH computation process

A simple and classical first-order scheme for integration is used. The time step is determined by the expression:

$$\delta t = C_{CFL} \text{Min}_i \left(\frac{h_i}{c_i + v_i} \right) \quad (1.20)$$

where the factor C_{CFL} is a numerical constant.

4.4. Coupled SPH-Finite Element Method (SFM)

Both FEM and SPH methods have certain advantages and disadvantages which when combined, enhance their performance further. To optimize the computational resources, in the coupled SPH-FEM method (SFM), the SPH particles are employed in the region of large deformation and damage, while the rest of the domain is modeled by the finite element (FE) mesh. Compared to the SPH method, the SFM is able to reduce the requirement of computational resources significantly by lowering the number of SPH particles. Application of the SPH method is limited to selected regions of very large deformation, fracture and damage to mitigate any numerical problems encountered in the FE approach. Moreover, using the FEM for the rest of the domain improves the accuracy of the results.

Both SPH and FE methods are based on the Lagrangian formulation. The SPH method can be easily included in an existing Lagrangian based FEM by considering SPH particles as elements with one node. Schematic overview of the Lagrangian SPH and FEM as shown in Figure 1.6 elaborates the major difference between the two methods, determination of strains, strain rate and forces. Same material model and equations of state are applicable for both methods. Therefore, it is possible to combine the two methods with appropriate conditions imposed at the interface.

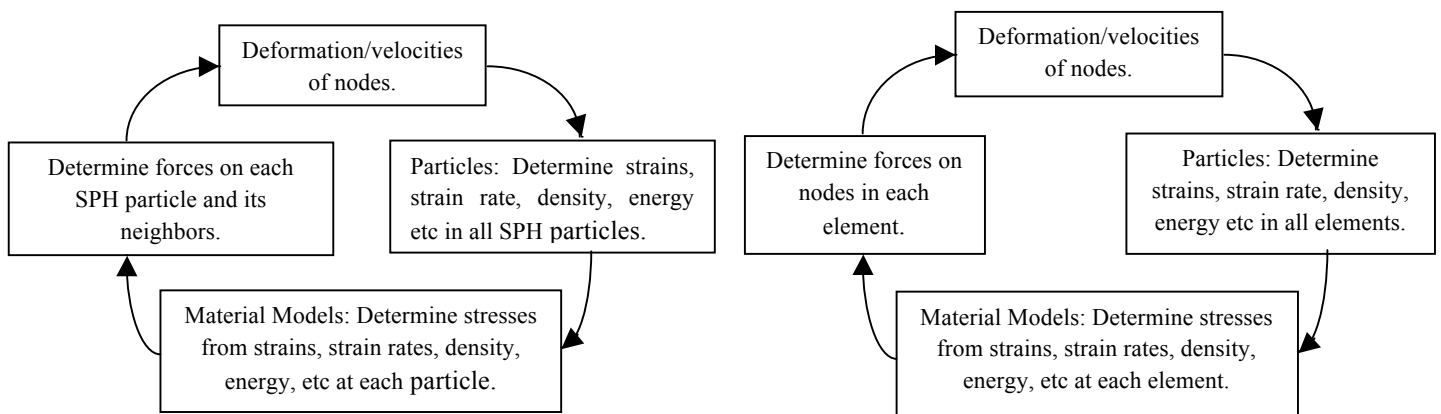
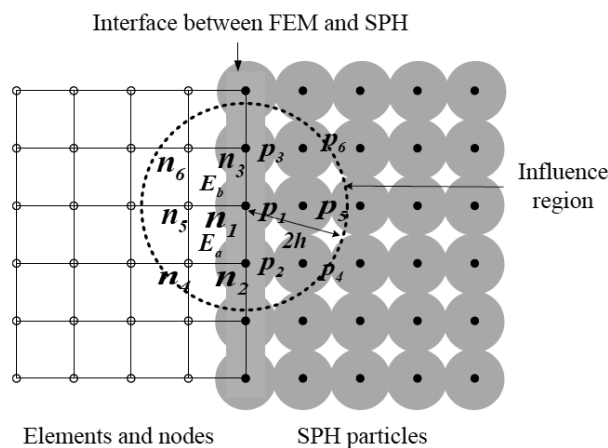


Figure 1.6 Lagrangian code structures for SPH particles and FEM elements

Figure 1.7 describes link between the finite elements and SPH particles. The interface between elements and particles ensures continuous bonding of the two methods. At the interface, the SPH particles are constrained and moved with the elements. A node to surface contact option is used to link the SPH particles and finite element surfaces where, the SPH particles are considered as slave nodes and the side of the finite element surface is treated as the master surface. Possible penetration of the slave nodes are continuously monitored throughout the calculation procedure with slave nodes displacements. Upon detecting reasonable penetration, a contact constraint is applied to push back the slave nodes towards the master surface (Attaway et al., 1994). The influence sub-domain of the particles at/near the interface zone such as the particle P_1 , covers both the FE and SPH particles, and hence certain considerations are required in the computation. For strain and strain rate calculation of each particle (P_1), only the SPH particles inside the influence sub-domain (P_1, \dots, P_6) are considered, whereas the contributions from both SPH particles (P_1, \dots, P_6) and interface elements (E_a and E_b) inside the influence sub-domain are used to calculate the forces (Johnson, 1994). Finite element nodes (n_1, \dots, n_6) within the influence domain are not considered for force calculation except through the elements. Figure 1.8 demonstrates the sliding interface between the SPH particles and finite elements. This is particularly significant for penetration events where projectile is modeled using finite elements and the target consists of SPH particles. Again a node to surface contact is used where, the SPH particles are considered as slave nodes and the side of the finite element surface is treated as the master surface.

**Figure 1.7** SFM: linking between the finite elements and SPH particles

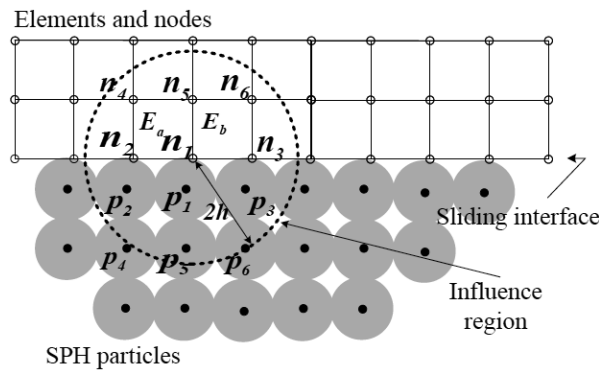


Figure 1.8 SFM: sliding contact between the finite elements and SPH particles

4.5. Initial Setup

In LS-Dyna, a set of particles has two kinds of properties: *Physical properties* which are mass, density, constitutive laws, defined in the ELEMENT_SPH and the PART cards, and *Geometrical Properties* of the model which concern the way particles, are initially placed. Two different parameters are to be fixed: Δx_i lengths and the CSLH coefficient. These parameters are defined in the SECTION_SPH card. A proper SPH mesh must satisfy the following conditions: it must be as regular as possible and must not contain too large variations. For instance, if a cylinder SPH mesh is considered, at least two SPH distribution types are possible (see Figure 1.9). The mesh number 2 includes too many inter-particle distance discrepancies. Therefore, the first mesh, more uniform, is better [63]. The coupling between finite elements and SPH elements is realized by using contact algorithms. Any “nodes_to_surface” contact type can be chosen where the slave part is defined with SPH elements and the master part is defined with finite elements.

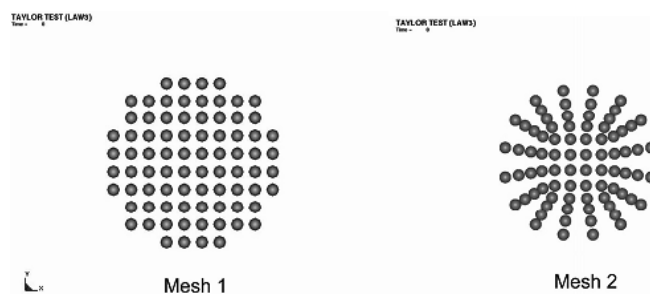


Figure.1.9. Cylinder SPH mesh possibilities

CHAPTER 2

***FULL ANALYSIS
OF THE BASIC
PROCESS OF
BIRD IMPACT***

1. INTRODUCTION TO THE FLUID DYNAMIC NATURE OF BIRD IMPACTS

Bird and substitute bird materials are recognized as soft body materials. Unlike impacts, involving strong materials, the impact of projectiles of soft-body materials is dominated by the tendency of the projectile material to behave like a fluid during the impact [67, 68]. For the impact of solids, the mechanisms dominating the impact process vary with impact velocity into five physical regimes [74]; *(a) elastic impact; (b) plastic impact; (c) hydrodynamic impact; (d) impact at sonic velocities, and ; (e) explosive impact.*

An impact involving a projectile of soft-body material against a target surface made of aluminum or steel generates stresses that substantially exceed the strength of the projectile material but are well below the strength of the target material. These materials have a much lower strength than that of typical target materials. This impact behavior of low-strength projectile materials has been theoretically and experimentally studied by Wilbeck [67].

Wilbeck [67] treated the impact of a bird on a rigid plate as an unsteady fluid dynamic process and developed a simplified one-dimensional analysis of a homogeneous right-circular cylinder of soft-body material impacting normally on a rigid plate. The analysis showed the entire impact process to occur in four distinct phases. *(a) the shock phase, (b) the release phase, (c) the steady flow phase, and (d) the termination of impact.*

In the first phase, which is the initial impact phase, very high shock, or Hugoniot, pressures are generated. This pressure was calculated [67], using the Hugoniot relation for a mixture, together with the shock properties of gelatin, and was compared with the peak pressure measured for the impact of right circular cylinders of gelatin with 10 percent porosity [68]. The Barber's measured pressures [68] and the Wilbeck's calculated pressure were in good agreement. Better agreement has been even shown in another work by Bauer and Barber [69, 70]. This agreement in the initial phase of the impact process has indicated that the hydrodynamic description of the event was well justified.

After the first phase, the high shock pressures decay to steady fluid dynamic pressures. These pressures were calculated by considering the process as steady jet flow. This theoretical conclusion was again in agreement with measured steady-flow pressures [67, 68, 70].

Furthermore, the calculations of shock decay by Wilbeck [67] have established that for a projectile with a length-to-diameter ratio larger than a critical value, the shock will be

severely weakened by radial expansion waves and the projectile should undergo complete shock decay to steady flow. Steady flow would be expected to prevail if the length-to-diameter ratio of the projectile in the direction of the impact exceeds approximately unity. For real birds striking end-on, the length-to-diameter ratio ranges from 2 to 3 and a steady-flow regime should occur. This conclusion has been amply supported by the measurements [67, 68, 70].

Further evidence of the tendency of the projectile material to flow radially outward at the impact location is apparent during the steady-flow phase. As the radial pressures decrease during the shock decay, shear stresses develop in the projectile material. If the shear strength of the projectile material is large enough to withstand these shear stresses, the radial motion of the projectile will be impeded. On the other hand, the projectile material will begin to flow if its shear strength is smaller than the shear stresses developed. The experiments have confirmed that for real birds, and gelatin, the shear strength is low enough for the pressures generated to cause the projectile material to flow.

The hydrodynamic impact was found to be the most representative for bird impact problems. Thus, the foundation of the hydrodynamic theory is presented in greater detail in the current work.

2. FULL ANALYSIS OF THE BASIC PROCESS OF BIRD IMPACT

When a cylinder of any material impacts a target plate, the particles on the front surface of the cylinder are instantaneously brought to rest relative to the target face and a shock is formed. The purpose of this shock wave is to bring each succeeding layer of particles to rest. The shock compression of a layer of particles is so rapid that the particles away from the edge of the cylinder do not have time to "communicate" with the free surface. This implies that these particles behave as if they are in a semi-infinite medium which can undergo only plane strain compression. Thus, shock compression in a bounded medium is usually considered to be a plane strain process.

The pressure in the shock compressed region is very high initially and is constant throughout the region at early times. As the shock propagates up the cylinder, the particles along the cylinder's edge are subjected to a very high pressure gradient due to the shock loading on one side and the free surface on the other. This pressure gradient causes the

particles to be accelerated radially outward and a release wave is formed. The function of this release wave is to relieve the radial pressures in the cylinder.

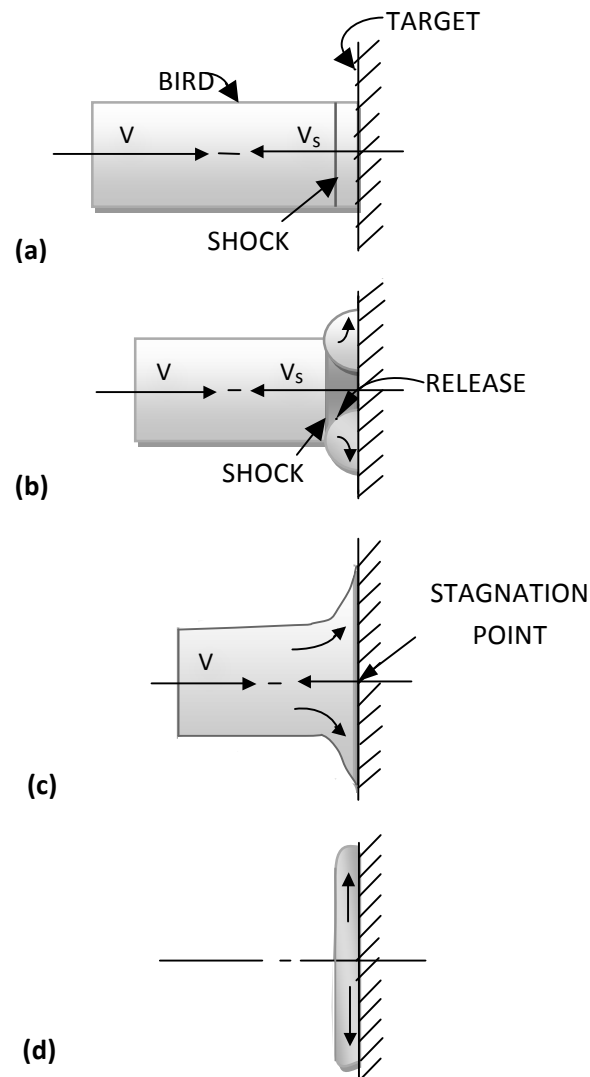


Figure. 2.1. The phases of bird impact (a) initial impact (b) impact decay (c) steady flow (d) termination.

A very complicated state of stress begins to develop in the cylinder. The radial pressure release causes shear stresses to appear. The radial acceleration of the particles also results in tensile stresses being developed. If, at any time, the state of stress is such that the strength of the material is exceeded, the material will "flow". For soft body impact, it will be assumed that the stresses throughout the impact event greatly exceed the material strength, so that the flow will continue indefinitely. For these materials, to a first approximation the material strength can be neglected so that they can be considered to behave as fluids.

After several reflections of the release waves, a condition of steady flow is established. A constant pressure and velocity field is set up in the cylinder, and the particles flow along paths which are fixed in space, called streamlines.

2.1. The Shock Phase

For the normal impact of a cylinder on a rigid plate, the flow across a shock can be considered one-dimensional and adiabatic, irreversible. In order to write the conservation laws across the shock, the steady state shock condition must be considered.

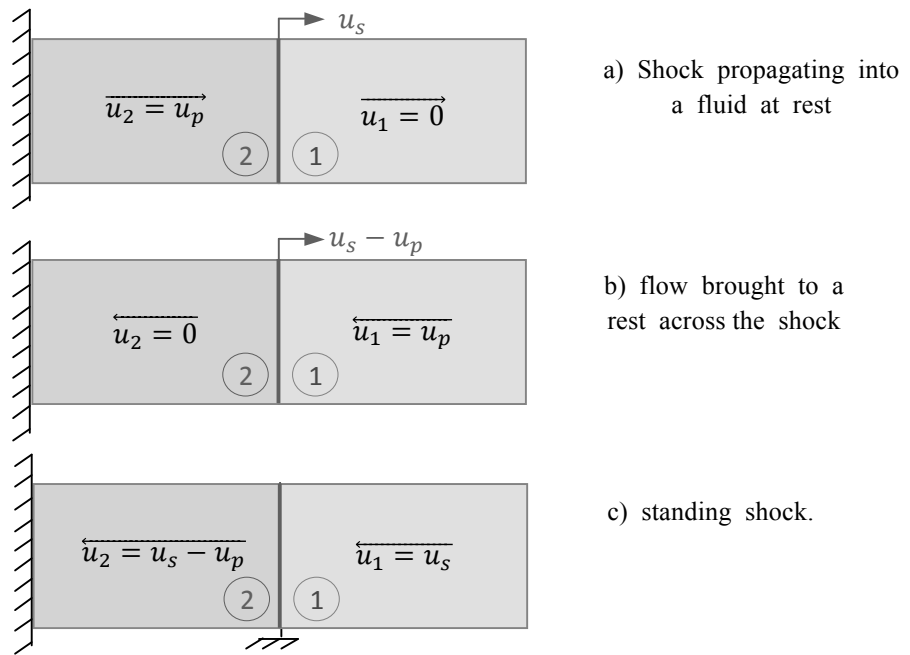


Figure 2.2. One dimensional shock flow.

where (1) represent the region in front the shock, (2) represent the region behind the shock.

2.1.1. *The governing equations:* The equations of conservation of mass (continuity) and momentum may be written

$$\rho_1 u_s = \rho_2 (u_s - u_p) \quad (2.1)$$

$$P_1 + \rho_1 u_s^2 = P_2 + \rho_2 (u_s - u_p)^2 \quad (2.2)$$

Combining these two equations, the pressure behind the shock is found to be

$$P_2 - P_1 = \rho_1 u_s u_p \quad (2.3)$$

The pressure in the shocked region, given by equation (2.3), is often referred to as the Hugoniot pressure, P_H , is given by:

$$P_H = \rho_1 u_s u_p \quad (2.4)$$

where u_s is defined as the velocity of the shock propagating into the fluid at rest and u_p is the velocity of the particles behind the shock.

For the impact of a cylinder on a rigid plate, it can be seen that $u_p = u_0$. Thus, for this case, Equation (2.4) becomes

$$P_H = \rho_1 u_s u_0 \quad (2.5)$$

For very low impact velocities, the shock velocity, u_s , can be approximated by the isentropic wave speed in the material, c_0 . Thus, for low impact velocities, Equation (2.5) may be approximated by the relation

$$P_H = \rho_1 c_0 u_0 \quad (2.6)$$

For most solids and fluids (including water and air) the relationship between the shock velocity and particle velocity can be expressed by the relationship, often called the "linear Hugoniot", as

$$u_s = c_0 + k u_p \quad (2.7)$$

where k is a constant for the material and c_0 is the sound speed (velocity of propagation of an infinitesimal disturbance) in the material.

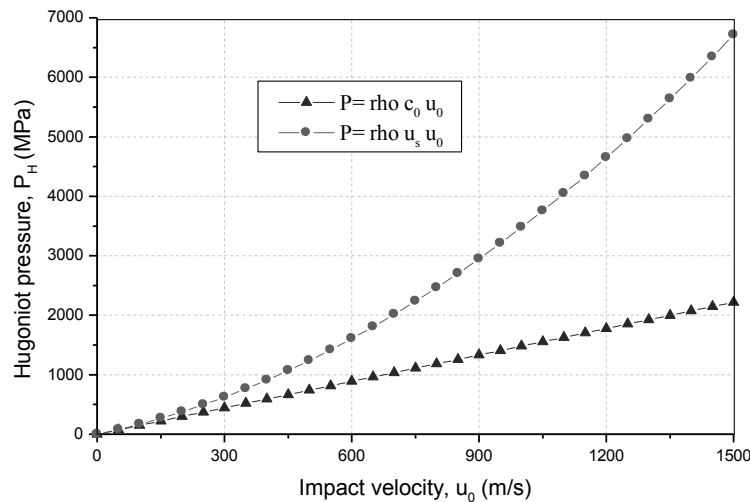
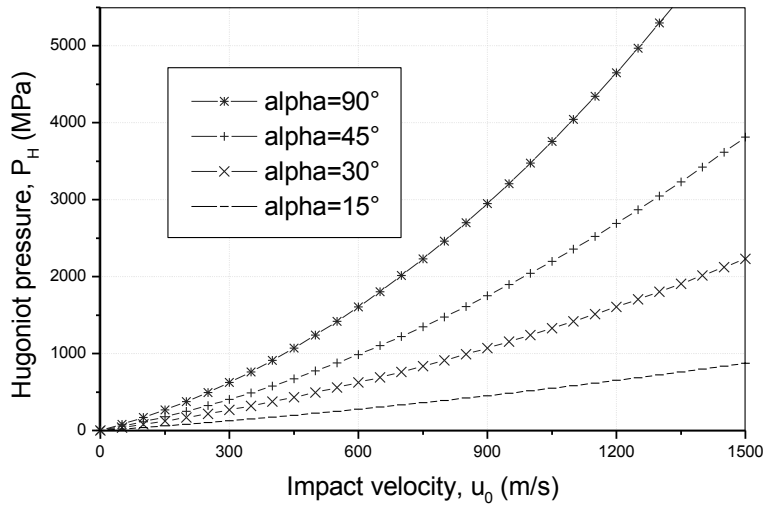


Figure 2.3. Compressibility effect on the Hugoniot pressure for water

For an oblique impact, the Hugoniot shock pressure is identical to that produced by a normal impact of a projectile with an initial velocity of $u_0 \sin \alpha$, and expressed as

$$P_H = \rho_1 u_s u_0 \sin \alpha \quad (2.8)$$

Figure 2.4 demonstrates the decrease in shock pressure with impact angle of obliquity, α , for the impact of a cylinder of water.

**Figure 2.4.** Obliquity effect on the Hugoniot pressure for water

For a non-rigid target, the pressures generated at the cylinder-target interface for the impact of an elastic target material are seen to be

$$P = \rho_p u_{sp} u_0 \left\{ \frac{\rho_t u_{st}}{\rho_p u_{sp} + \rho_t u_{st}} \right\} \quad (2.9)$$

where the subscript p refers to the cylinder properties, and the subscript t refers to the target properties.

Several calculations were made for the normal impact of water on various targets at a velocity of 200 m/s. For the impact on steel, the shock pressure found using Equation (2.9) is approximately 4% less than that found using Equation (2.5). For titanium, the difference is approximately 8%; for aluminum, approximately 11%; and for polycarbonate, approximately 35%.

The expression for the initial shock pressure is given by Equation (2.5). A second expression is needed which provides the response of the impact material under shock loading.

2.1.2. The development of the shock equation of state for non-porous material

It is desirable to obtain a relationship between the pressure and density on both sides of the shock. The continuity equation across the shock, may be written in the form

$$\frac{u_p}{u_s} = 1 - \frac{\rho_1}{\rho_2} = q \quad (2.10)$$

Substituting this relationship into Equation (2.7) gives

$$\frac{u_s}{c_0} = \frac{1}{(1 - K \cdot q)} \quad (2.11)$$

and Equation (2.5) may be written in the form

$$P_2 = \frac{\rho_1 c_0^2 q}{(1 - k \cdot q)^2} \quad (2.12)$$

Another approximate expression for the pressure-density relationship across a one-dimensional shock was given by Cogolev, et al. (Reference [64]), and takes the form

$$P_2 = A \left\{ \left(\frac{\rho_2}{\rho_1} \right)^B - 1 \right\} \quad (2.13)$$

where, A and B are material constants. Ruoff [65] has demonstrated that for a material that exhibits a linear Hugoniot, these constants may be approximated by the expressions

$$A = \frac{\rho_1 c_0^2}{(4k - 1)} \quad ; \quad B = 4k - 1 \quad (2.14)$$

However, many of the soft body materials are porous. The cellular structure of birds normally contains a small amount of porosity. Thus, for porous materials, Equations (2.12) and (2.13) are not representative. Therefore, the following section describes the development of the shock equation of state for porous materials.

2.1.3. The development of the shock equation of state for porous material

The porous material is defined simply as a mixture of two constituents: a soft body material and air. The average density of the material can be defined by the expression

$$\rho_z = z \rho_{air} + (1 - z) \rho_f \quad (2.15)$$

where ρ_z is the average density of the soft body material with porosity, ρ_f is the full density of the soft body material (density without porosity), the term z represents the volume fraction of air, and $(1 - z)$ represents the volume fraction of the soft body material.

Torvik [66] derived an equation for density changes across a shock for a homogeneous mixture, expressed by

$$\frac{\rho_{1AVG}}{\rho_{2AVG}} = \sum_{i=1}^N f v_i \left(\frac{\rho_{1i}}{\rho_{2i}} \right) \quad (2.16)$$

where ρ_{AVG} is the average density of the mixture, $f v_i$, is the volume fraction of the i^{th} constituent, ρ_i is the density of the i^{th} constituent, and N is the number of constituents.

Thus, the shock equation of state for the porous material is given by

$$\frac{\rho_{1,porous}}{\rho_{2,porous}} = (1 - z) \frac{\rho_{1,non\ porous}}{\rho_{2,non\ porous}} + z \frac{\rho_{1,air}}{\rho_{2,air}} \quad (2.17)$$

Torvik's equation should hold true for any compression process (shock and isentropic compression) in which all the assumptions [66, 67] are satisfied and the pressure-density relationships are known for each constituent of the mixture. Assumptions are: **i)** the porous material is macroscopically homogeneous and isotropic, **ii)** the density of each constituent of the mixture is the same as for a homogeneous sample of the given constituent at the same pressure, **iii)** the size of individual particles, of each component is such that the shock pressure is the same in each component, and **iv)** the constituents do not react or change phase during the compression process.

The pressure-density relationship of the soft body material is represented by equation (2.13). Assuming, the material can be represented by a linear Hugoniot, equation (2.7), the constants A and B can be expressed by equation (2.14). The equation (2.13) may be rearranged to obtain

$$\frac{\rho_2}{\rho_1} = \left(\frac{P_2}{A} + 1 \right)^{1/B} \quad (2.18)$$

The pressure-density relationship of air for a shock compression may be approximated by the relationship for a perfect gas

$$\frac{\rho_2}{\rho_1} = \frac{1 + \left(\frac{\gamma + 1}{\gamma - 1} \right) \left(\frac{P_2}{P_1} \right)}{\left(\frac{\gamma + 1}{\gamma - 1} \right) + \left(\frac{P_2}{P_1} \right)} \quad (2.19)$$

where γ is the ratio of specific heats, and is equal to 1.4 for air.

However, equation (2.19) is not a realistic equation of state for air especially for a density ratio up to the value 6.0 (see Figure. 2.5). Air could be represented by the linear Hugoniot relationship [71], equation (2.7), where $k = 1.03$. Note that materials which could be represented by the linear Hugoniot relation could also be represented by the pressure-density relationships given in equations (2.12) or (2.13). Upon examination, air was best represented by equation (2.12) [71].

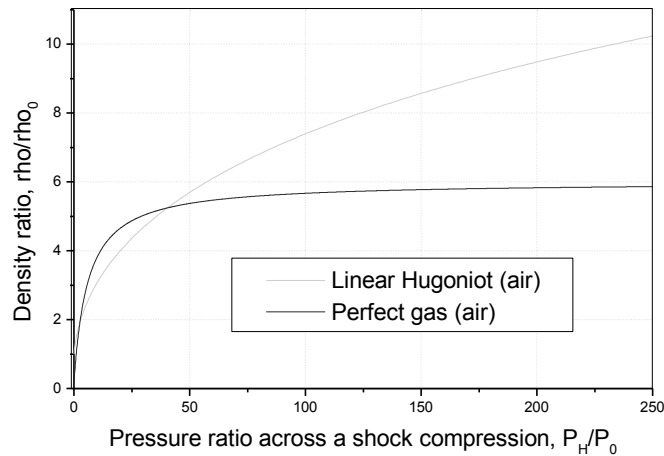


Figure 2.5. Shock Hugoniot for air

It can be noted from the definition of q that

$$\frac{\rho_2}{\rho_1} = \frac{1}{1 - q} \quad (2.20)$$

Rearranging Equation (2.12) into a form compatible with Equation (2.16)

$$\bar{P} \equiv \frac{P_2}{P_1} = \left\{ \frac{\rho_1 c_0^2}{P_0} \right\} \left\{ \frac{q}{(1 - k \cdot q)^2} \right\} \quad (2.21)$$

which gives

$$\bar{P} (1 - k \cdot q)^2 - \left\{ \frac{\rho_1 c_0^2}{P_0} \right\} \cdot q = 0 \quad (2.22)$$

Solving for q from the quadratic equation, it is seen that

$$q = q_1 \pm q_2 \quad (2.23)$$

$$\text{where } q_1 = \frac{2\bar{P}k + \frac{\rho_1 c_0^2}{P_0}}{2\bar{P}k^2} \quad \text{and} \quad q_2 = \frac{\left\{ \left(2\bar{P}k + \frac{\rho_1 c_0^2}{P_0} \right)^2 - 4\bar{P}^2 k^2 \right\}^{1/2}}{2\bar{P}k^2} \quad (2.24)$$

In order for $\frac{\rho_2}{\rho_1}$ to be positive, q must be less than unity. So, Equation (2.23) must take the form

$$q = q_1 - q_2 \quad (2.25)$$

Thus, the final expression for the shock pressure-density relationship of air is given by Equation (2.20), where q is given by Equation (2.25) and q_1 and q_2 by Equation (2.24).

Combining Equation (2.13) for the soft body material without porosity, and Equation (2.20) for air, into Equation (2.17) for the mixture, gives the pressure-density relationship under shock compression for porous materials of the form

$$\frac{\rho_{1,\text{porous}}}{\rho_{2,\text{porous}}} = (1 - z) \left(\frac{P_2}{A} + 1 \right)^{-1/B} + z(1 - q) \quad (2.26)$$

Figure 2.6, shows the effect of porosity on the shock pressure for water as a function of the impact velocity. From this figure, it can be seen that porosity induces a sharp decrease in the pressure. Figure 2.7, illustrates the pressure-volume relationship across the shock compression for water with various porosities, equation (2.26), where the material properties used for water and air are listed in Table 2.1.

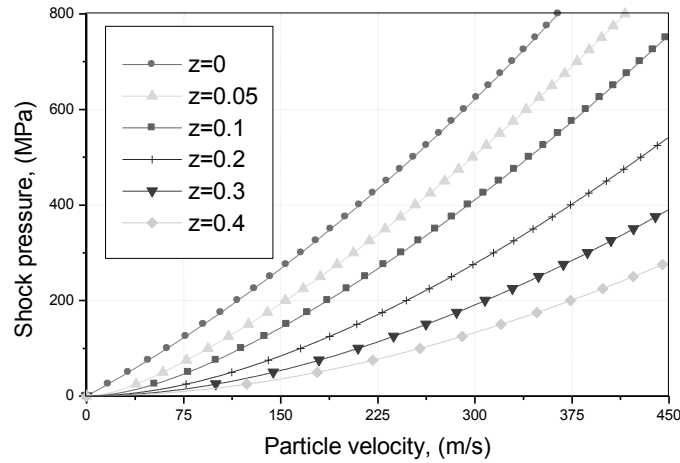


Figure 2.6. Porosity effect on the Hugoniot shock for water

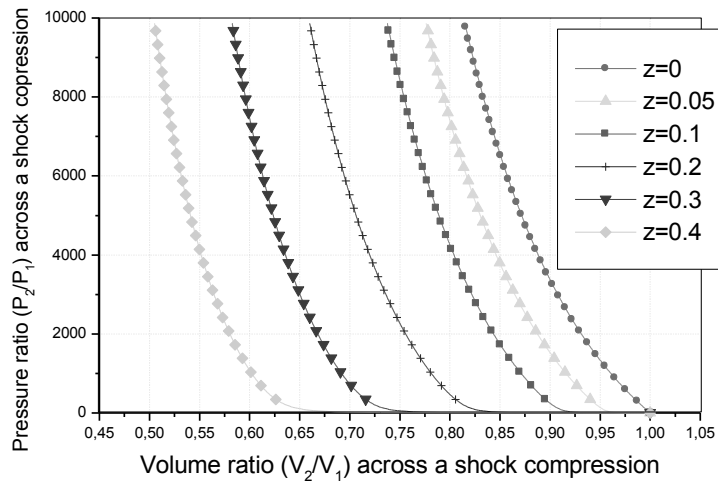


Figure 2.7. Pressure vs. volume relationship across a shock compression for water with various porosity

Table 2. 1. Material properties for water and air [72, 73]

<i>at:1 atm & 20 °C</i>	<i>Water</i>	<i>Air</i>
c_0	1482.9 (m/s)	340.9(m/s)
ρ_0	998.23 (Kg/m ³)	1.204 (Kg/m ³)
k	2	1.03

The decrease in shock velocity due to porosity (Figure. 2.8) results in a marked decrease in the shock pressures. Figure 2.9, shows the variation in specific volume (density)

with pressure up to 500 MN/m^2 (5 Kbar) for water with porosity added and Figure 2.10, looks at the lower portion of these curves for pressures up to 20 MN/m^2 .

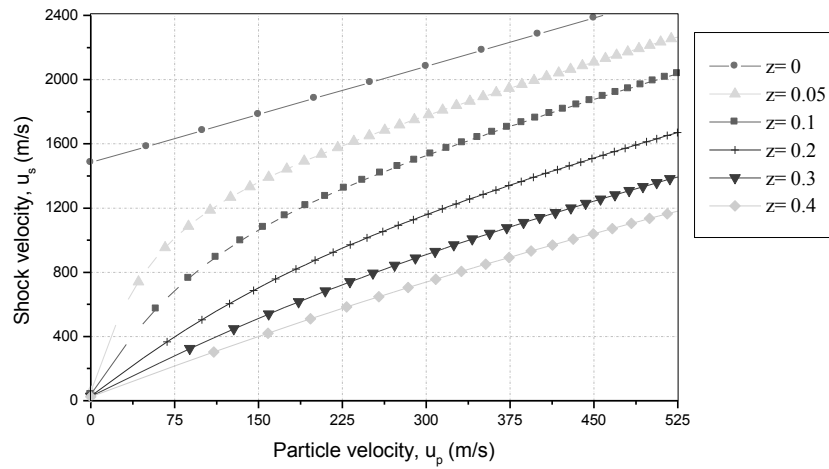


Figure 2.8. Porosity effect on the shock velocity for water

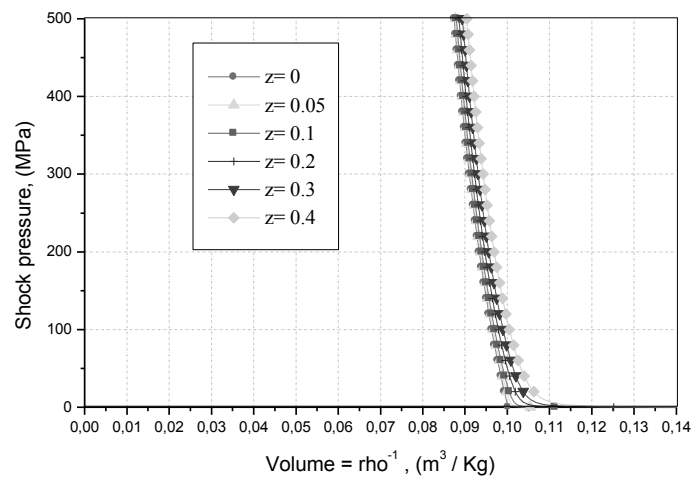


Figure 2.9. Hugoniot Pressure-volume* 100 relationships for water with various porosities, for pressures up to 500 MN/m^2 (5 kbar)

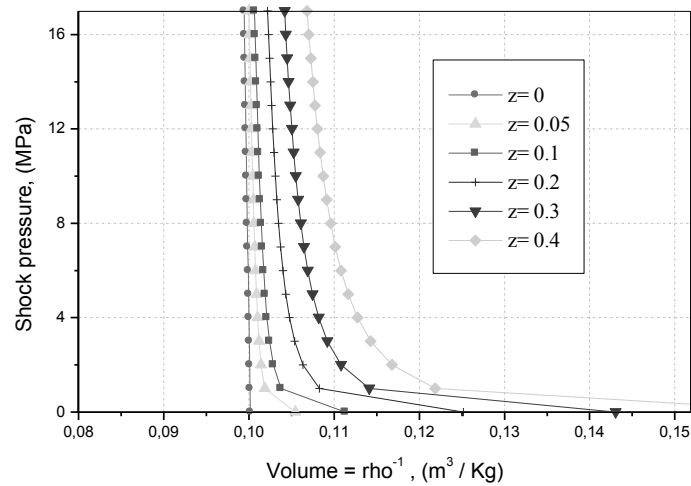


Figure 2.10. Hugoniot Pressure-volume relationships for water with various porosities, for pressures up to 20 MN/m^2

Figure 2.11, shows the plot of the theoretical Hugoniot shock pressure for pure ($z=0.0$) and porous ($z=0.1$) water with the experimental pressure measurements for the impact of birds [67]. These plots show the advantage of having the added complication of air to water versus just void. For example, the contribution of 10% of air to the pressure for an impact velocity of 150 m/s is quantified to be 124 MPa less to that obtained for pure water. Therefore, porosity has to be considered in the material.

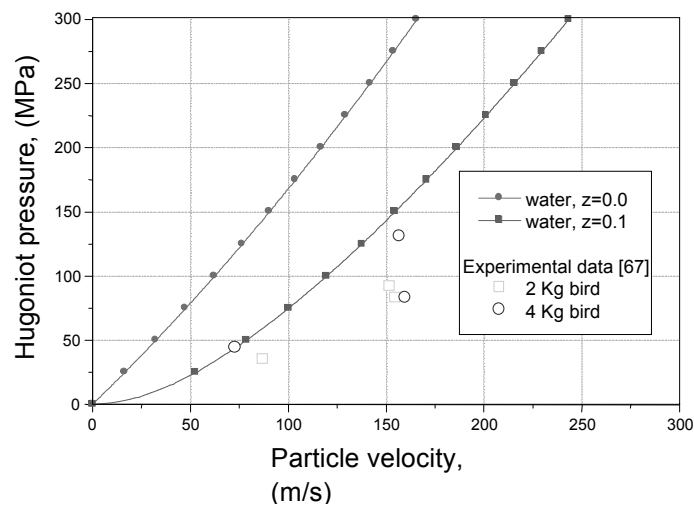


Figure 2.11 . Hugoniot Shock pressures measured during normal impact of birds

2.2. The Release Phase

As soon as the shock is formed it begins to propagate up the impact and radial release waves propagate in towards the center axis of the impact.

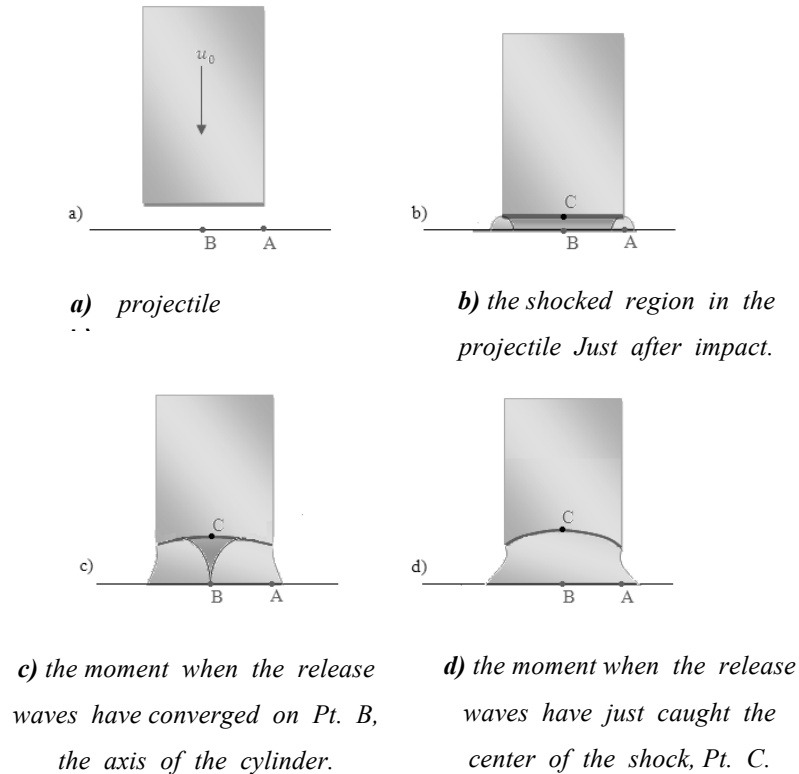


Figure 2.12. Shock and release waves in fluid impact

The duration of the shock pressure at the center of impact, can be approximated by the time necessary for the release wave to initially reach the center of impact, *Pt. B*, is expressed as

$$t_B = a/c_r \quad (2.27)$$

where, a is the initial radius of the cylinder, c_r , the velocity of the initial release wave which is just the speed of sound in the shocked material.

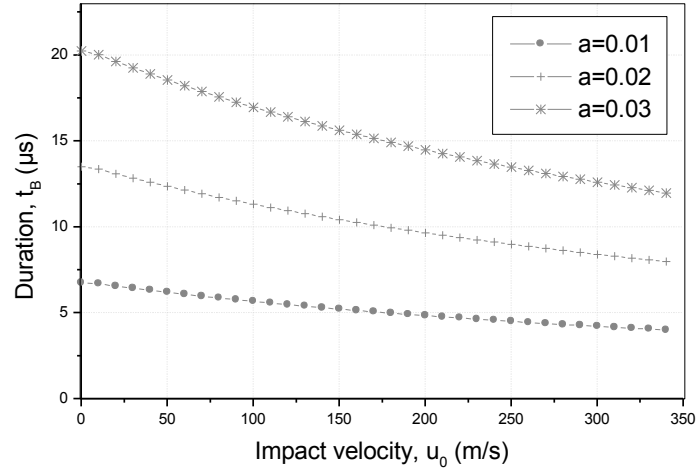


Figure 2.13. Duration of the Hugoniot pressure vs. impact velocity for a cylindrical impact of water

It should be noted that the velocities of the shock and release waves are much greater than the initial velocity of the impact.

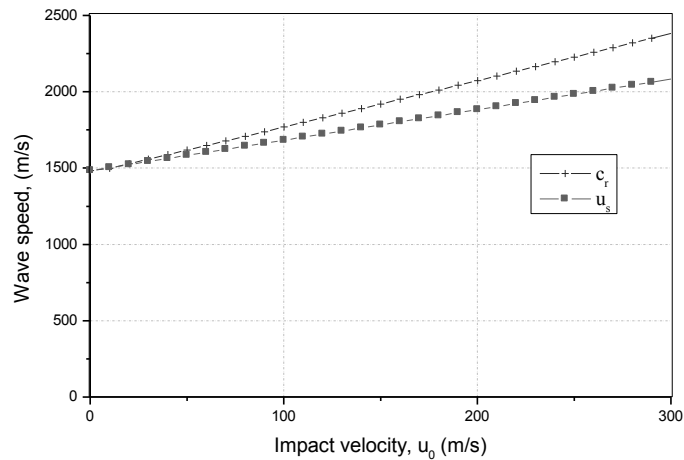


Figure 2.14. Comparison of the shock velocity, u_s , and the sound speed in the shocked region, c_r

The time that it takes the front of the release wave to just capture all of the shock wave, t_c , is given by

$$t_c = \frac{a}{\{c_r^2 - (u_s - u_0)^2\}^{1/2}} \quad (2.28)$$

after this time, the pressure in the region behind the shock will rapidly decay.

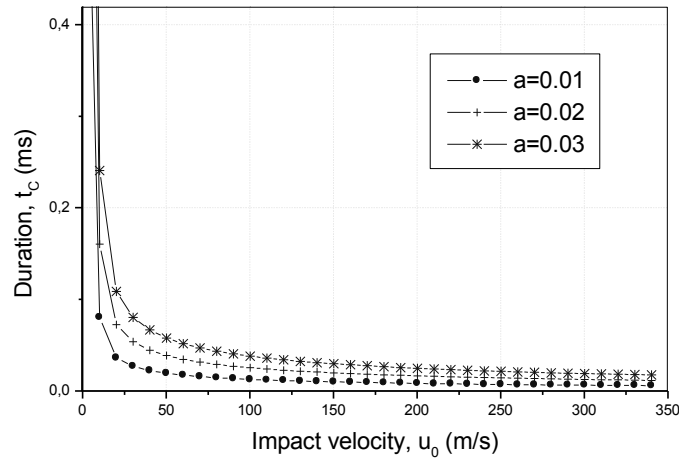


Figure 2.15. Duration for which the pressure will rapidly decay, t_c , vs. impact velocity for a cylinder impact of water (a , is the initial radius of the cylinder).

The length for which the radial release wave will just intersect the shock on axis, **Point. c**, as the shock reaches the end of the cylinder, called the critical cylinder length, L_c , is expressed as

$$L_c = u_s t_c \quad (2.29)$$

The nondimensional critical cylinder length, $(L/D)_c$, is expressed as

$$(L/D)_c = \frac{u_s}{2 \{c_r^2 - (u_s - u_0)^2\}^{1/2}} \quad (2.30)$$

where D is the initial diameter of the cylinder.

For a cylinder with an $L/D < (L/D)_c$, the shock will reflect off the cylinder rear surface before it has all been captured by the radial release waves. The shock will be reflected in the form of a rarefaction wave.

However, for a cylinder with an $L/D > (L/D)_c$, the shock will be substantially weakened by the release waves prior to reaching the cylinder rear surface and its effects will be reduced or effectively cancelled.

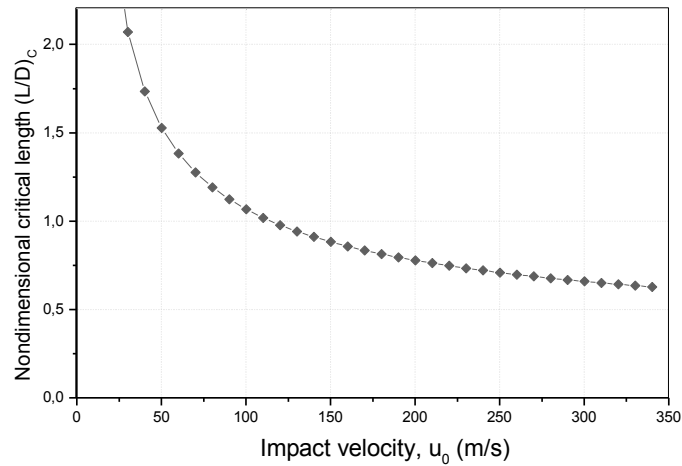


Figure 2.16. Variation of the critical length vs. impact velocity for water

The existence of steady flow, of course, is dependent on the length (or L/D) of the cylinder. For very short cylinders, the impact event will be over before the release regime has ended.

2.3. The Steady Flow Phase

As the radial pressures decrease during the shock pressure decay, shear stresses develop in the cylinder material. Since the shear strength of birds is so low, the pressures generated are usually sufficient to cause “flow”. The bird is considered to behave as a fluid.

After several reflections of the release waves, a condition of steady flow is established and steady pressure and velocity fields are established.

Along each streamline, Bernoulli's equation can be written

$$\int \frac{dP}{\rho} + \int u \, du = K'' \quad (2.31)$$

where K'' is constant along the streamline.

For the case of a cylinder impacting a rigid plate, the flow field is essentially uniform at some distance away from the impact surface, so that the K'' must be the same for each of the stream-lines in this region. This implies that K'' has the same value throughout the entire flow field.

The pressure P , at any point in the flow field can be related to the velocity, u , at that point by the relation

$$\int_{P_0}^P \frac{dP}{\rho} + \int_{u_0}^u u \, du = 0 \quad (2.32)$$

where P_0 and u_0 are the pressure and velocity of the uniform flow field some distance away from the impact surface and are approximated by the atmospheric pressure and the initial impact velocity.

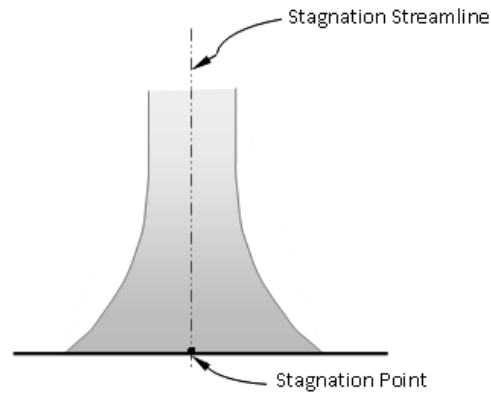


Figure 2.17. Steady flow

In order to obtain the pressure at any point along the impact surface from Equation (2.32), the velocity at that point must be known and the equation of state of the material, $\rho = \rho(P)$, must be known. The expression for the velocity at a point is not found so easily.

The normal approach is to assume an expression for the velocity field based on empirical data, where the pressure at the center and the pressure at the edge are found using Equation (2.32). Then, to assume a general expression for the pressure distribution based on empirical data. This expression is forced to satisfy the pressure boundary conditions and conservation of momentum.

- The axial symmetry dictates that the point at the center of the plate be the stagnation point. The first boundary condition is that the pressure at the center of the plate is the stagnation pressure, P_s (gauge pressure), and the velocity at the center is zero. Therefore, at the center of the plate, Equation 2.32 takes the form

$$\int_{P_0}^{(P_s + P_0)} \frac{dP}{\rho} = \frac{u_0^2}{2} \quad (2.33)$$

For an incompressible fluid, Equation (2.33) gives

$$P_s = \frac{1}{2} \rho u_0^2 \quad (2.34)$$

For a compressible fluid (most materials), Equation (2.33) implies

$$P_s \geq \frac{1}{2} \rho u_0^2 \quad (2.35)$$

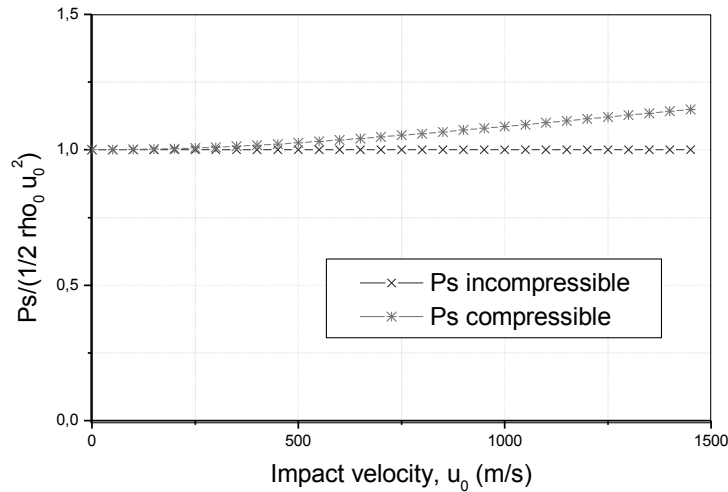


Figure 2. 18. Compressibility effects on stagnation pressure in steady flow for a cylinder impact of water

- The second pressure boundary condition is that the pressure must go to zero at some radial distance from the center.
- Simple momentum considerations require that during steady flow, the impulse imparted to the target by a unit of fluid must be equal to the axial momentum lost during impact. This may be written

$$\int_0^{t_D} (F dt) = \int_{u_0}^u (M du) \quad (2.36)$$

where the force, F , is assumed constant during steady flow and the duration of impact is represented by t_D . For a unit of fluid with initial values of mass M , density ρ , length L , and cross-sectional area A , this expression becomes

$$F t_D = M (u - u_0) \quad (2.37)$$

For most soft body materials including birds, the rebound velocity after impact, u , is so small that it may be ignored. Also, during steady flow, the duration of impact for a unit of fluid of length, L , is simply the time required for the fluid to flow through its length. That is,

$$t_D = L/u_0 \quad (2.38)$$

Thus, the force generated in the steady flow regime is seen to take the form

$$F = \rho A u_0^2 \quad (2.39)$$

Since the force is simply the integral of the pressure over the impact surface, this expression may be rewritten

$$2\pi \int_0^{\infty} P r dr = \rho A u_0^2 \quad (2.40)$$

Leach and Walker [76], have developed a polynomial expression for the pressure distribution for the normal impact of a water jet. This expression was generalized for soft body impacts to allow for the increased stagnation pressure due to compressibility as

$$P = P_s \left\{ 1 - 3 \left(\frac{r}{\zeta_2 a} \right)^2 + 2 \left(\frac{r}{\zeta_2 a} \right)^3 \right\} \quad (2.41)$$

where r is the radial distance from the center, a is the initial radius of the jet, and ζ_2 is constant, from momentum considerations, $\zeta_2 = 2.58$. The plot of equation (2.41) is illustrated in Figure 2.19.

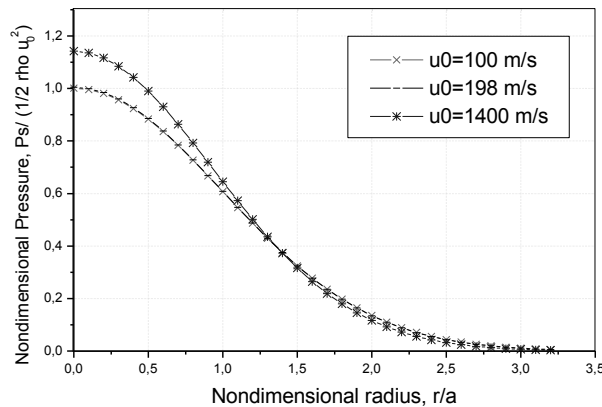


Figure 2.19. Compressibility effects on the radial distribution of steady flow pressure for the normal impact of a water jet

Challita et al [77, 78], have used the three dimensional potential flow theory to predict the pressure distribution produced by the steady flow of a cylindrical jet impacting on a rigid plate. Figure 2.20, illustrates the radial pressure distribution computed from potential theory for normal impacts [79], while the Figure 2.21 demonstrates the distribution of pressure computed for oblique impacts [79].

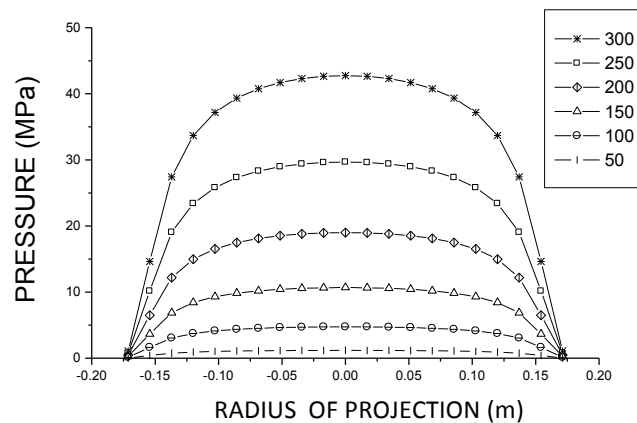


Figure 2.20. Steady flow pressure distribution vs impact velocity (m/s) of 0.060 Kg bird along major axis for normal impact [79]

Note that for the case of an oblique cylinder, the stagnation point moves from the center of the impact and the distribution of pressure is not axisymmetric.

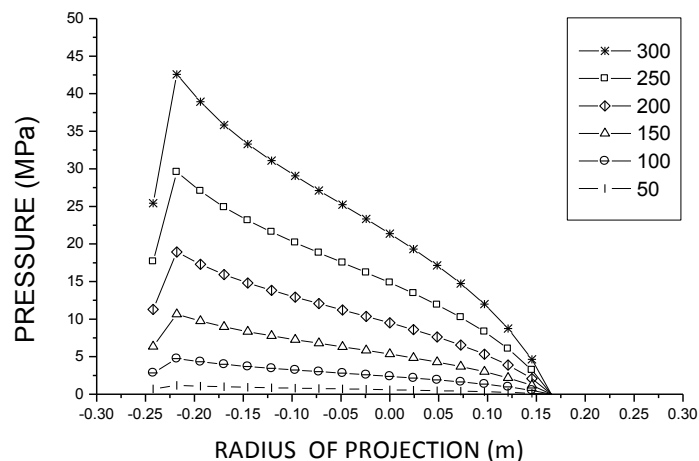


Figure 2.21. Steady flow pressure distribution vs impact velocity (m/s) of 0.060 Kg bird along major axis at 45 °, for oblique impact [79]

2.3.1. The development of the steady state equation of state for porous material:

The pressure-density relationship of the soft body material is represented by Equation (2.42)

$$P_2 = A \left\{ \left(\frac{\rho_2}{\rho_1} \right)^B - 1 \right\} \quad (2.42)$$

Assuming the material can be represented by a linear Hugoniot, Equation (2.7)

$$u_s = c_0 + k \cdot u_p \quad (2.7)$$

the constants can be expressed by Equation (2.14)

$$A = \frac{\rho_1 c_0^2}{(4k - 1)} ; \quad B = 4k - 1 \quad (2.14)$$

Equation (2.42) may be rearranged to obtain

$$\frac{\rho_2}{\rho_1} = \left(\frac{P_2}{A} + 1 \right)^{1/B} \quad (2.43)$$

The pressure-density relationship of air for an isentropic compression may be approximated by the relationship for a perfect gas

$$\frac{\rho_2}{\rho_1} = \left(\frac{P_2}{P_1} \right)^{1/\gamma} \quad (2.44)$$

where γ is the ratio of specific heats ($\gamma = 1.4$ for air).

Thus, substituting Equations (2.43) and (2.44) into Equation (2.17), the pressure-density relationship under isentropic compression for a porous material is seen to be

$$\frac{\rho_{1,porous}}{\rho_{2,porous}} = (1 - z) \left(\frac{P_2}{A} + 1 \right)^{-1/B} + z \left(\frac{P_2}{P_1} \right)^{-1/\gamma} \quad (2.45)$$

The decrease in density due to the addition of porosity causes a decrease in the stagnation pressure during steady flow. However, the increase in compressibility effects tends to counteract this, so that the resulting decrease is relatively small. Figure 2.22 presents the variation in the steady flow stagnation pressure for water with porosity. It can be seen that porosity barely changes the pressure during the steady flow phase. Figure 2.23, shows the relationship between the pressure and the volume across an isentropic compression for water with various porosities, Equation (2.45).

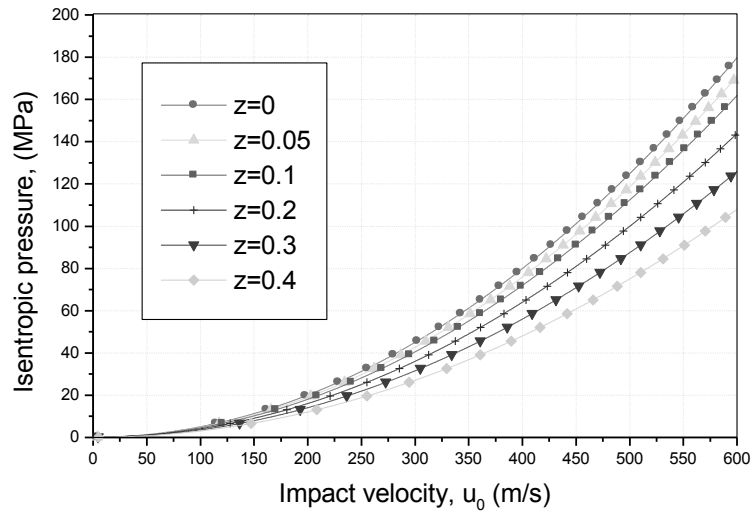


Figure 2.22 . Porosity effect on the isentropic pressure for water

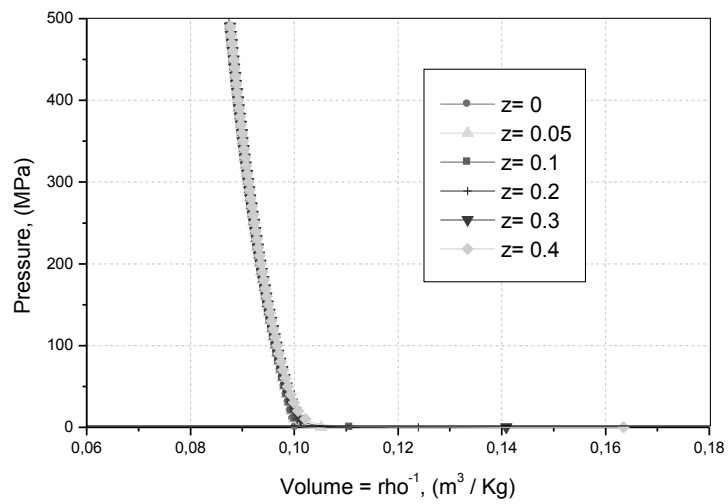


Figure 2.23. Isentropic pressure-volume relationships for water with various porosities, ($P < 500 \text{ MN/m}^2$)

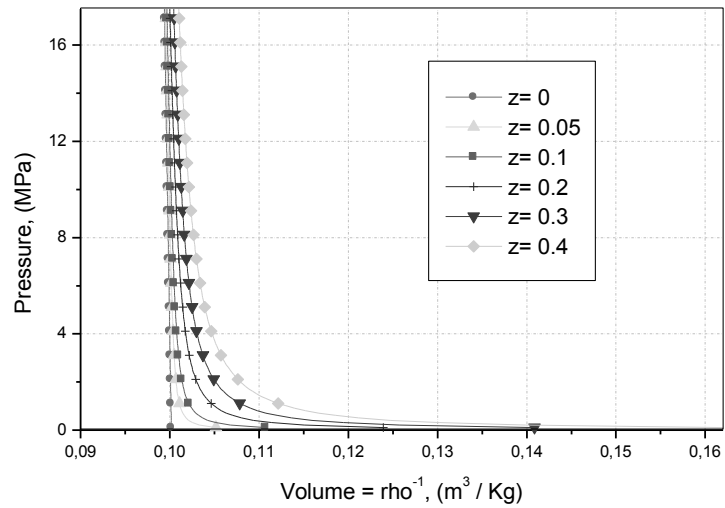


Figure 2.24. Isentropic pressure-volume relationships for water with various porosities, ($P < 20 \text{ MN/m}^2$)

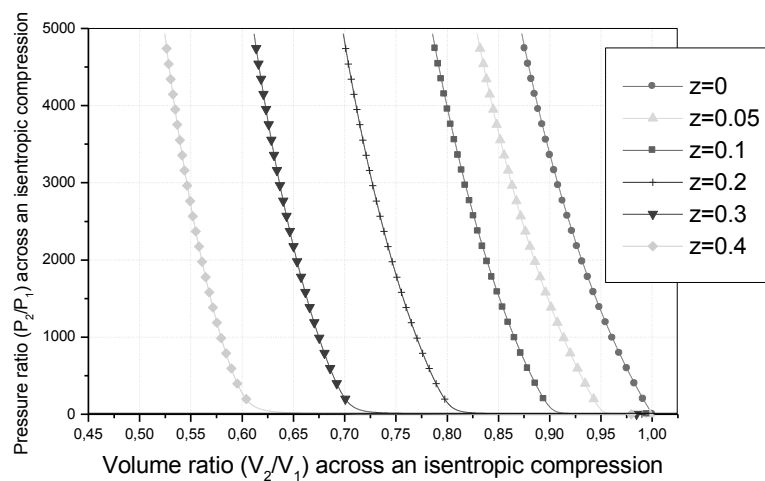


Figure 2.25. Pressure vs. volume relationship across an isentropic compression for water

2.4. The Termination of Impact

As the fluid nears the target surface there is a gradual decrease in velocity with a corresponding increase in local pressure. Thus, during steady flow there is a pressure field set up in the fluid in which the local pressure is maximum at the stagnation point and decreases to the atmospheric pressure, P_0 , at a substantial distance from this point. As the end of the cylinder nears the impact surface, it enters this field of increasing local pressure and disrupts

the field due to the immediate drop in pressure behind the impact rear surface. Release waves emanate from the rear surface and propagate to the impact surface, thereby causing a slight decrease in the impact velocity of the rear surface as well as a decrease in the pressure along the impact surface of the target. This process continues until the end of the cylinder reaches the surface of the plate and the impact event is ended.

The total duration of the impact can be approximated by the time needed for the cylinder to "flow through" its length, or

$$t_D = \frac{L}{u_0} \quad (2.46)$$

Deviation from this could be caused by the decrease in cylinder velocity due to release waves from the back surface of the cylinder.

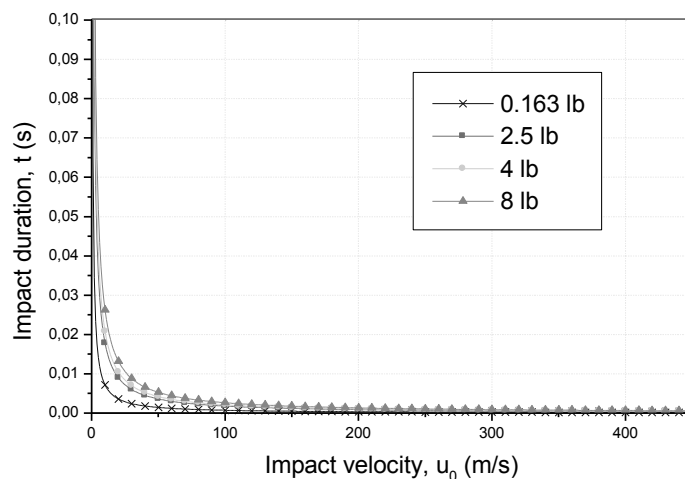


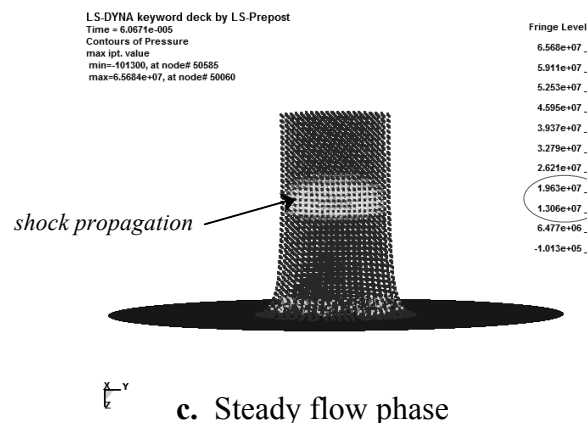
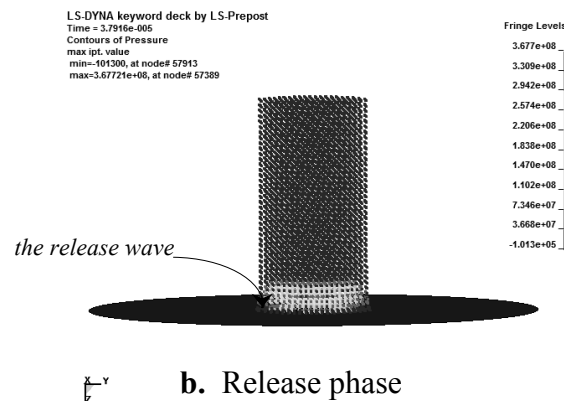
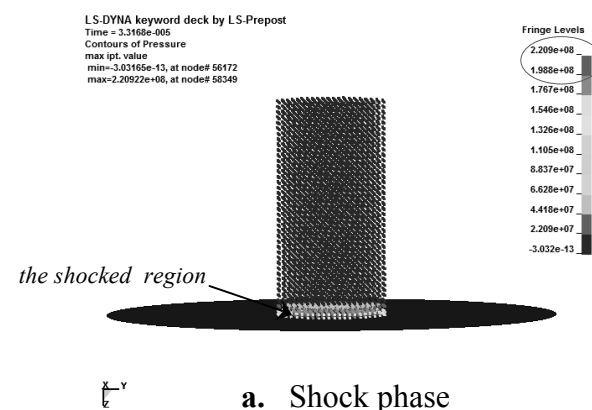
Figure 2.26. Total duration of impact for different weight of a cylinder of water with 10% of porosity

3. PREDICTION OF THE FLUID PROCESS FOR BIRD IMPACT

The entire bird impact process onto a rigid plate was investigated from a numerical standpoint using LS-DYNA. A simplified model of bird, 'cylinder of water' with a weight of 0.163 lb, was initially developed and validated referring to the theory. The developed bird model was based on the Smoothed Particle Hydrodynamic (SPH) method due to their remarkable features: It is not affected by the problems caused by distortions in large deformation and gives better representation of the fluid-like movement of soft body impacts

including their disintegration process [75]. The material density of the bird was equal to 898.52 Kg/m^3 , which is equivalent to that of the mixture of water (90%) and air (10%). The equation of state (EOS) of water with 10% porosity was also used as EOS of the bird material. The entire impact process of the bird was predicted from the simulation and illustrated in Figure 2.27, where, the Figure 2.27-a presents the shock phase, Figure 2.27-b presents the release phase, Figure 2.27-c presents the steady flow phase and Figure 2.27-d presents the termination of the impact.

Figures 2.28 and 2.29 present the plot of the shock pressure and the isentropic stagnation pressure for water with 10% of porosity versus impact velocity obtained from the theory.



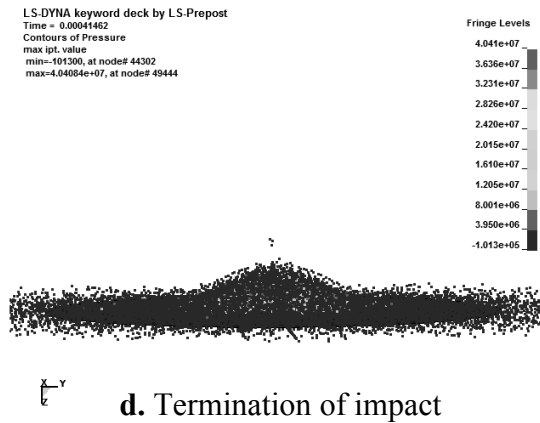


Figure 2.27. SPH impact model of a cylinder of water with 10% of porosity on a rigid plate

From this simulation, it was easy to distinct the four phases characterizing the impact process of birds, as shown in Figure 2.27. During the initial phase of the impact process, Figure 2.27 (a), a high interval of pressure is registered between 198 MPa and 220 MPa in the shocked region and it was constant throughout this region. As illustrated in Figure 2.27(b), radial wave is formed at the edge of the cylinder; consequently, decay in pressure was occurred. The duration of the release phase was very short and was captured to be about 15 μ s. As illustrated in Figure 2.27 (c), the shock is propagated up the cylinder and the material started to flow. The pressure achieved in this steady flow phase was in the interval of 13.0 MPa and 19.6 MPa. Figure 2.27 (d), shows the state when the end of the cylinder approached from the rigid plate and the flow was terminated. The pressure in this termination phase was approximately equal to the atmospheric pressure.

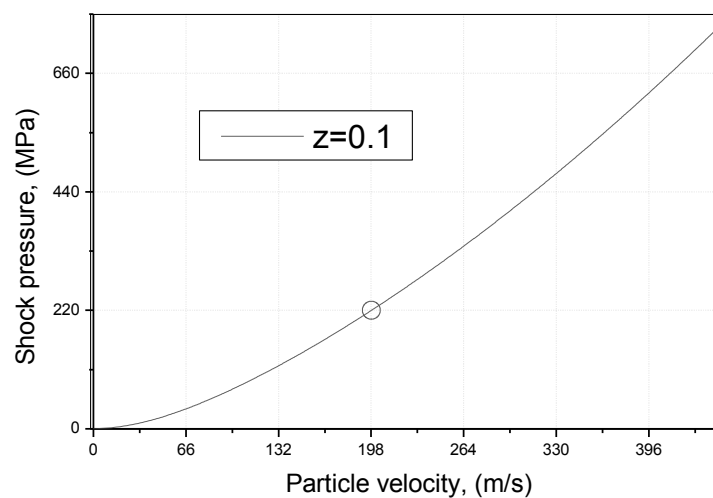


Figure. 2.28. Hugoniot shock pressure for water with 10% of porosity

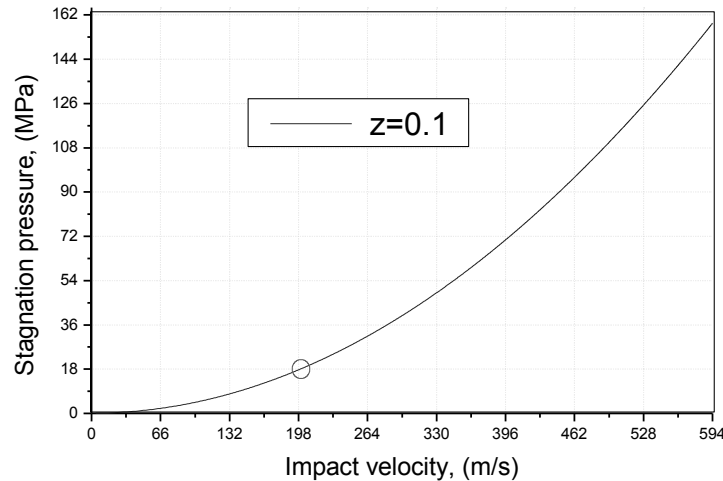


Figure. 2.29. Isentropic pressure at the stagnation point for water with 10% of porosity

The two numerical impact pressures values obtained from the simulation, the peak and the steady flow pressures, were considered in the validation of the impact process. The Hugoniot pressure calculated from the theory for the impact of a cylinder of water with 10% of porosity at a velocity of 198 m/s is equal to 220 MPa, as shown in Figure 2.28. Thus, the isentropic pressure value calculated from the theory for the same impact is equal to 18 MPa, as shown Figure 2.29. The numerical impact pressures in the shock and in the steady flow phases were in accordance with the analytical pressures. The comparison shows that an excellent agreement was achieved.

CHAPTER 3

**BIRD IMPACT
MODELS
DEVELOPMENT
& VALIDATION**

1. INTRODUCTION

The proof of a certain level of bird strike resistance for each aircraft forward-facing component in certification tests is required by the aviation authorities before that component is allowed for operational use. The component should be tested experimentally and real birds have to be used. In order to optimize the number of experiments required for a successful test, validated simulations of bird strikes can substitute the physical aircraft component's tests. To comply with this task, an appropriate numerical bird impact model has to be developed and validated against experimental data before using it for impact simulations on real aircraft components. For this purpose, it is common practice to simulate the impact on a rigid flat plate and to assess qualitatively the flow behavior for comparisons with high speed films and to assess quantitatively the pressure curve for comparisons against data from pressure transducers. Thus, this section refers to bird impact;

- *model development for 0.163 lb, 4 lb, and 8lb;*
- *scenario prediction on flat and highly curved, rigid and deformable configurations for small size of bird (0.163 lb) and large sizes of bird (4lb and 8 lb);*
- *model validation, on a rigid plate, on a deformable leading edge bay, and on real C27J aircraft leading edge.*

2. TEST DATA FOR SMALL SIZE OF BIRD, 0.163 lb, IMPACTING A FLAT RIGID DISK

2. 1. Barber's Experimental Test Data

Because the availability of test data is limited, Barber's 1975 experimental test [80] has been used for validation. In Barber's work, the graphs describe pressure-time variations as functions of velocity, radii from centre of impact and bird size. Piezoelectric quartz transducers were used in the tests. Birds (baby chicken) weighing from 0.060 Kg to 0.150 Kg were shot at velocities from 30 to 350 m/s on a flat rigid plate. The plate was a 4340 steel disk with 5.10 cm thickness, 15.25 cm diameter and heat treated to yield strength of 1035 MN/m² and Rockwell C45. Bird impact pressure data of 84 shots were listed in this reference [80]. The test, "shot 5126", which has the data listed in (Table 3.1), was used for validation of the bird impact model developed in this section. The pressure from the centre of impact (peak pressure on transducer "A") was taken as a reference for calibrating and validating the model.

The test's other data (transducers "B" and "C") were used for the complete validation of the bird's impact model.

Table.3.1. Test data: shot 5126 [80]

Shot	Bird mass (Kg)	Velocity (m/s)	Transducer r position	Peak pressure (MN/m ²)	Pulse duration (μs)
5126	0.074	198	A	41.0	485
5126	0.074	198	B	29.9	475
5126	0.074	198	C	13.5	470

Note: Positions: A-center of impact, B-1.27 cm off center, C-2.54 cm off center

2.2. Bird Modeling Development

The SPH element formulation implemented in the explicit finite element code "LS-DYNA" was used to model the bird with a weight of 0.074 Kg and an equivalent density of 898.52 kg/m³. Details on bird modeling are presented below

2.2.1. Bird model geometry

The shape of the bird is particularly important when the impact pressures are of interest. The cylindrical shape is used for bird strike onto fan blade while the hemispherical shape is recommendable to reproduce the impact of a real bird [88].

Three different configurations have been tested for the SPH bird model. The bird biometric data were obtained for each configuration using the following empirical formula.

The relationship between weight (mass) and density has been assessed from databases of more than 30 species of birds to be [83];

$$\rho_b(\text{plucked}) = 959 - 63 \cdot \log_{10}(W_b) \quad (3.1)$$

where ρ_b is the bird density in kg/m³, W_b is the weight of the bird in Kg.

From the same database as above the relationship between mass and torso diameter is

$$\log_{10}D = -1.095 + 0.335 \log_{10}(W_b) \quad (3.2)$$

More simplified representation of equation (3.2) for the bird diameter is given by

$$D = (0.0804) \cdot W_b^{0.335} \quad (3.3)$$

where D is the bird diameter in m, W_b is the weight of the bird in Kg.

Using equation (3.1), the density of a bird with a mass of 0.074 kg (0.163 lb) was derived equal to 898.52 kg/m³. Since the volume and density are linked by mass, the volume and length can be determined for each configuration of the bird model.

1. *The right circular cylinder shape, $L/D=2$* ; bird was modeled as a cylinder with double length in respect to diameter, as shown in (Figure 3.1). The diameter, D , was given by

$$D = \left(\frac{2V_b}{\pi} \right)^{1/3} = \left(\frac{2W_b}{\pi\rho_b} \right)^{1/3} = 0.0374 \text{ m} \quad (3.4)$$

V_b is the bird volume, W_b is the bird mass and ρ_b is the density of the bird.

The total length of the bird, L , was equal to 0.0748 m.

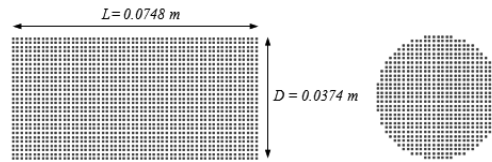


Figure 3.1. SPH bird model with cylindrical shape, $L/D=2$

2. *The Cylindrical shape with hemispherical ends, $L/D>2$* ; the bird was modeled as a hemispherical cylinder with an aspect ratio, L/D , greater than 2, as (Figure 3.2) demonstrates.

The volume of the hemispherical cylinder is equal to the sum of the volume of the cylinder and the volume of the sphere. Using equation (3.3), the diameter, D , of the bird was found equal to 0.033608 m.

The cylindrical length of the bird, L_c , was assumed to be

$$L_c = 4 \cdot \left(\frac{W_b}{\pi \rho_b D^2} - \frac{D}{6} \right) = 0.0704 \text{ m} \quad (3.5)$$

Thus the total length of the bird, L , was equal to

$$L = L_c + D = 0.1040 \text{ m} \quad (3.6)$$

The aspect ratio, L/D , was equal to 3.095.

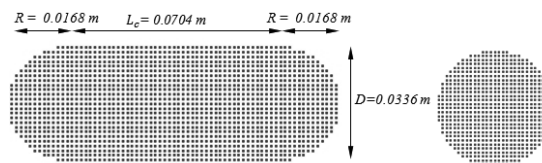


Figure 3.2. SPH bird model with hemispherical shape, $L/D>2$

3. *The Cylindrical shape with hemispherical ends, $L/D=2$* ; the bird was modeled with double length in respect to diameter, as (Figure 3.3) illustrates. The diameter, D , was given by

$$D = \left(\frac{12 V_b}{5 \pi} \right)^{1/3} = \left(\frac{12 W_b}{5 \pi \rho_b} \right)^{1/3} = 0.03977 \text{ m} \quad (3.7)$$

The total length of the bird, L , was equal to 0.07954 m

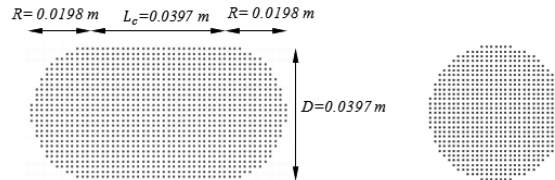


Figure 3.3. SPH bird model with hemispherical shape, $L/D=2$

The numbers of the SPH particles in each bird model were, 15705 particles, 15415 particles, and 16086 particles, for the cylindrical configuration, the hemispherical configuration with $L/D > 2$, and the hemispherical configuration with $L/D = 2$, respectively. In all those configurations, the SPH particles were distributed equally spaced in all directions.

A note about the selection of the following parameters: SPH particles number, contact model, material model and EOS model were based on a convergence study carried out by the author and the appropriate ones are used in this section.

2.2.2. Bird impact material model

The material model used for the bird was defined by *MAT_NULL card in LS-Dyna, where an equation of state (EOS) must be used with it. This material model has no yield strength and behaves in a fluid like-manner. Optionally the following parameters were defined: viscosity, erosion in compression (CEROD) and in tension (TEROD). The parameter *TEROD* represents the relative volume V/V_0 , for erosion in tension and is set equal greater than unity, while the parameter *CEROD* represents the relative volume, V/V_0 , for erosion in compression and is set less than unity. The cut-off pressure was also defined to allow for the material to “numerically” cavitate. In other words, when the bird material undergoes dilatation above certain magnitude, it should no longer be able to resist this dilatation. Since dilatation stress or pressure is negative, setting the pressure cut off for the bird material equal to a very small (given) negative value would allow for the material to cavitate once the pressure in the bird material goes below this negative value. In addition, The Null material has

no shear stiffness and hourglass control was (must be) used with great care. In some applications the default hourglass coefficient might lead to a significant energy loss.

2.2.3. Bird impact EOS model

The equation of state describes the behavior of the bird during impact. The development of an accurate equation of state is necessary to obtain reliable results from simulation. It will affect the kinematics of the SPH particles at impact and as a result influence the loads applied to the structure by the fluids.

Ls-Dyna has 10 equations of state models. The tabulated form (TYPE 9 *EOS_TABULATED), which is linear in internal energy, has been used for the bird material model. The pressure P is defined by:

$$P = C(\varepsilon_V) + \gamma T(\varepsilon_V) E \quad (3.8)$$

where C represents the function or constants array and T , the temperature which depends on volumetric strain. ε_V is natural logarithm of the relative volume V and E is the internal energy. But for a high impact process like birdstrike, the temperature T does not play a major role and hence it is negligible. Thus the term $\gamma T(\varepsilon_V)E$ becomes zero. The effective EOS becomes

$$P = C(\varepsilon_V) \quad (3.9)$$

The volumetric strain ε_V is given by the natural logarithm of the relative volume and is defined by

$$\varepsilon_V = \ln\left(\frac{V_2}{V_1}\right) \quad (3.10)$$

In a shock compression, when the volumetric strain ε_V decreases ($\varepsilon_V < 0$), the pressure increases ($P > 0$). In order for P to be positive, C must be less than unity. So C is given

$$C = \frac{-P}{\varepsilon_V} \quad (3.11)$$

The mixture by volume of water (90%) and air (10%) has been shown to have similar characteristics as birds [67], thus the state's equation of this mixture is used as EOS for the bird model. Figure 3.5 shows the plot of the Hugoniot pressure for a mixture with several amounts of porosity into the tabulated form, equation (3.9).

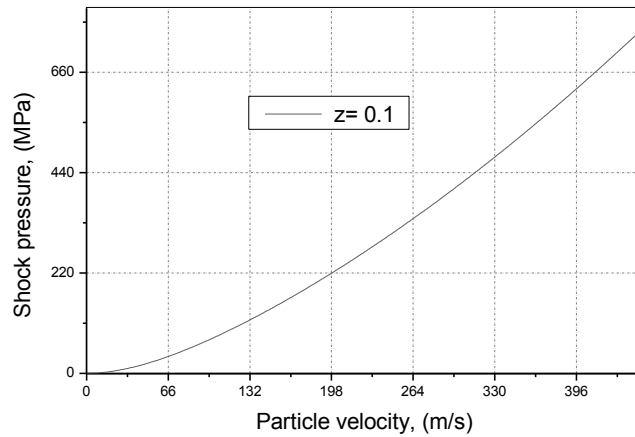


Figure 3.4. Plot of the shock pressure for water with 10% of porosity versus the impact velocity

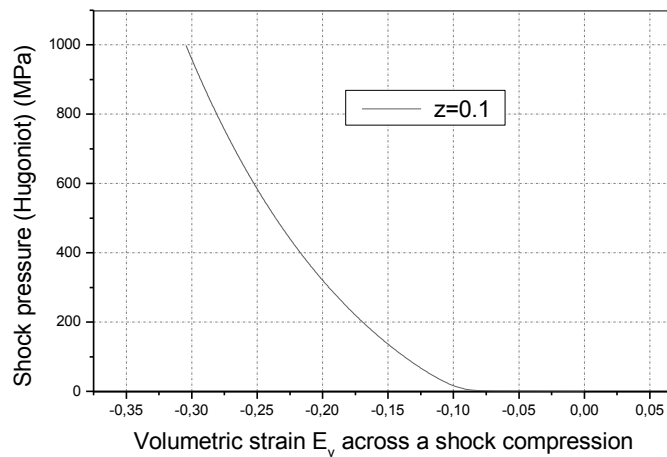


Figure 3.5. Plot of the shock pressure for water with 10% of porosity versus volumetric strain, $P=f(\epsilon_V)$, Tabulated EOS type 9

2.3. Finite Element Flat Disk and Transducers Modeling

The rigid 4340 steel disk was modeled as a flat circular plate, with 5328 four-node Belytschko-Tsai shell elements and a uniform thickness of 0.051 m. The diameter of the disk was 15.25 cm. The SPC were set all around the disk using the *BOUNDARY_SPC card by constraining the node's rotational and translational degree of freedoms in all directions. The material model used for the disk was defined by MAT-RIGID card in LS-Dyna and has the mechanical properties listed in (Table 3.2).

In order to obtain the pressure on the same point of pressure measurement provided by Barber (1975), a transducer with an area of 12x 12 mm² was modeled on the center of the disk with 144 solid elements. The MAT-RIGID card was used to define the material model of the transducer, and has the properties listed in (Table 3.3).

Table.3.2: Mechanical properties of the 4340 steel [80, 84]

ρ (Kg/m ³)	E (GPa)	ν
7850	200	0.29

Table.3.3: Mechanical properties of the piezoelectric quartz transducer [85]

ρ (Kg/m ³)	E (GPa)	ν	G (GPa)	K (GPa)
2650	97.2	n/a	31.14	36.4

2.4. The Contact Modeling

The contact model significantly influences the pressure curve during impact simulation on a flat rigid plate [81]. Selecting an appropriate contact model has a great importance.

Two contacts were defined, one between the bird and the upper surface of the transducer and the other between the lower surface of the transducer and the disk. The interaction between the SPH bird and the target (flat disk, plate, LE) was done through an AUTOMATIC_NODES_TO_SURFACE_CONTACT. In this contact type the SPH node set was assigned as slave and the target surface was the master.

The contact area, where the nodal contact forces are evaluated and converted into pressure for comparison with the experimental pressure, was the transducer area and has a great influence on the peak pressure.

2.5. Validation of the Small Bird, 0.163 lb, Impact Model on a Rigid Flat Disk

The simulation of impact on the rigid plate has been performed for the three bird model configurations as it is reported in the following Figures and the time histories of the resultant forces of contact were obtained for each configuration.

The bird impact behavior on the rigid plate at 198 m/s, has been assessed for the three configurations and it is shown in (Figure 3.6), where the impact duration, “t” was, $t = 3.919689 E-04(s)$, $t = 5.760445 E-04(s)$, and $t = 4.896183E-04(s)$, for the cylindrical model, the hemispherical model with $L/D>2$, and the hemispherical model with $L/D=2$, respectively.

The force curve was obtained for each bird configuration. Figure 3.7, shows the plot of the contact force in (N) at the center of the plate versus time in (s) in correspondence to each bird configuration.

The correlation was guaranteed by the same boundary conditions and the only parameter that changes was the bird geometry. The contact peak pressure was calculated by dividing the resultant peak force generated in the contact between the bird and the transducer over the area of the transducer which equals to 144 mm^2 . The peak contact force was read from the plot obtained from the simulation (Figure 3.7).

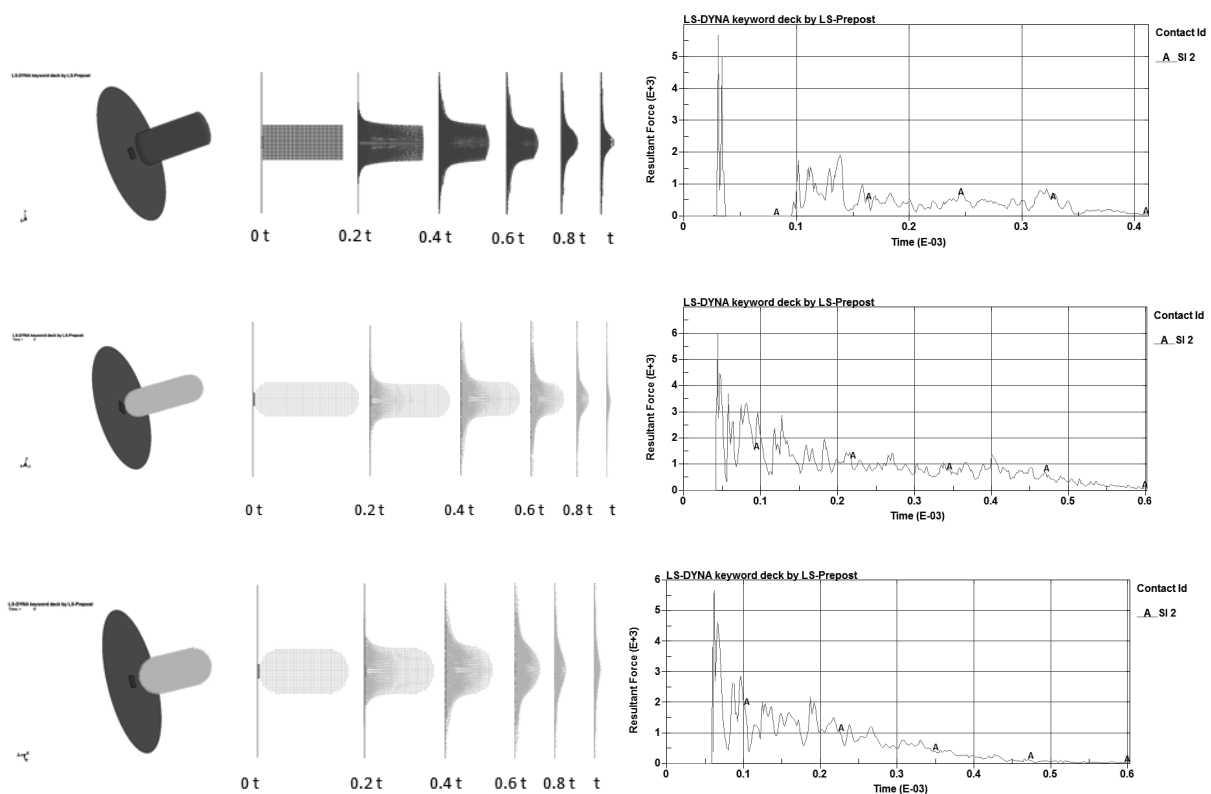


Fig 3.6. Bird impact scenarios on the rigid plate at 198 m/s

Fig 3.7. Plot of the contact force (N) vs time (s)

The peak force intensity obtained from the simulations has a constant trend for each configuration simulated with a value roughly equal to 5.7- 6 KN. The impact duration obtained from the simulations varies from 391 to 489

μ s. Table 3.4, shows the comparison between numerical results and Barber's experimental results concerning the peak pressure and the impact duration.

Table 3.4. Comparison between numerical and the experimental results

<i>Bird model</i>	<i>Peak pressure "A"</i>	<i>Error</i>	<i>Pulse duration</i>	<i>Error</i>
<i>Real bird (Barber)</i>	41.0 MPa		485 μ s	
<i>cylindrical, L = 2D</i>	39.58 MPa	3.46 %	391 μ s	19.38 %
<i>Hemispherical, L > 2D</i>	41.66 MPa	1.62 %	576 μ s	18.76 %
<i>Hemispherical, L = 2D</i>	39.58 MPa	3.46 %	489 μ s	0.82 %

Considering that the peak pressure obtained from Barber's experimental test was 41 MPa [80], an excellent agreement was achieved. An error of 1.62% for the hemispherical model with $(L/D) > 2$ was obtained, while an error of 3.46% was calculated for the hemispherical model with $(L/D) > 2$. The present numerical results show that the length-to-diameter ratio has little influence on the pulse duration, where the hemispherical model with $L/D=2$ gives a good result with an error of 0.82%. Also, comparing curves obtained from simulation for the different models with Barber's pressure curve [80], it is confirmed that the bird model which fits more than others to a bird strike test is the hemispherical ended shape with $L/D=2$.

For a complete validation of the hemispherical model with $L/D=2$, two other transducers, B and C, were modeled at different distances from the center of the plate, as illustrated in (Figure 3.8). The transducer B was set at 1.27 cm, while the transducer C was set at 2.54 cm. The plots of the contact force obtained on these points are shown in (Figures 3.9 and 3.10). Table 3.5, summarizes the pressures data obtained from this simulation.

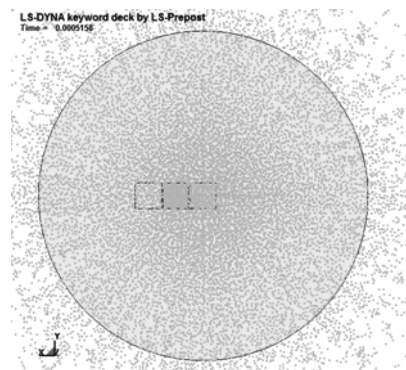
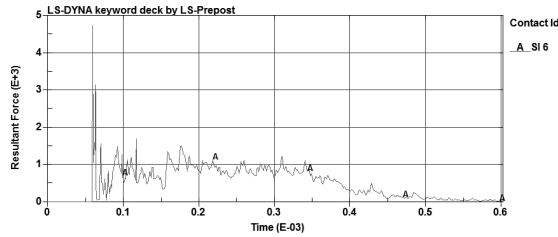
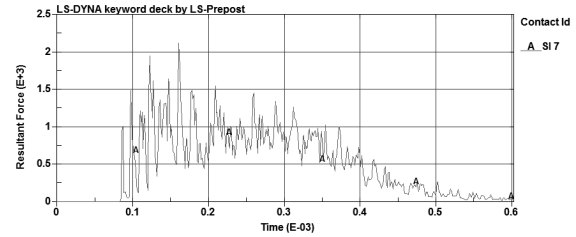


Figure 3.8. Transducers' B" and "C" modeling

Figure 3.9. Transducer *B*: resultant contact forceFigure 3.10. Transducer *C*: resultant contact force**Table 3.5.** Comparison between numerical and the experimental results

	<i>Transducer “B”</i>		<i>Transducer “C”</i>	
	<i>Peak pressure</i>	<i>Pulse duration</i>	<i>Peak pressure</i>	<i>Pulse duration</i>
<i>Barber’s test</i>	29.9 MPa	475 μ s	13.5 MPa	470 μ s
<i>Simulation</i>	32.63 MPa	490 μ s	14.58 MPa	515 μ s
<i>Error</i>	9.13 %	3.15 %	8 %	9.57 %

Correlating the numerical pressure data with the experimental data, (Table 3.5), it is evident that a good agreement was achieved. This good accordance was not only seen in the peak pressure but also on the pulse duration and the graphs’ path [80].

3. TEST DATA FOR LARGE SIZES OF BIRD, 4 lb & 8 lb, IMPACTING A FLAT RIGID PLATE

3.1. CHALLITA’s Experimental Test Data

Real birds (chicken) were impacted at three impact angles (90° , 45° , 25°) and at velocities ranging from 100 m/s to 300 m/s on a flat rigid plate. Piezoelectric quartz pressure transducers were used as the basic sensing devices for these experimental tests. The pressure signals were displayed on an oscilloscope as function of time. Tests of 4 lb and 8 lb birds at velocities of (289 m/s, 104 m/s, 245 m/s, 115 m/s) and obliquity of (90° and 45°), which have the data listed in (Table 3.6), were used for validation of the bird impact models developed in this section. The pressure from the centre of impact (peak pressure on transducer) was taken as a reference for model validation.

Table 3.6. Challita experimental data for the impact of 4lb and 8lb [77]

Impact weight	Impact angle	Impact velocity (m/s)	Transducer position	Pressure ($\text{MN}/\text{m}^2\text{-cm}$)
1560 g (real bird)	90°	289	center	46.3
1560 g (real bird)	45°	104	center	5.2
3220 g (gelatin 10%)	90°	245	1” above center	32.8

3490 g (gelatin 10%)	45°	115	center	16.6
----------------------	-----	-----	--------	------

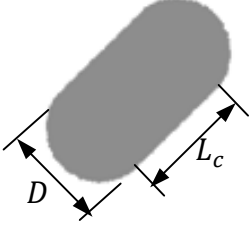
3.2. Finite Element Modeling

The rigid steel plate was modeled as a (700 x700 x 20 mm³) flat plate with 100,000 four node Belytschko-Tsai shell elements. SPC were set all around the plate using the *BOUNDARY_SPC card by constraining the node's rotational and translational degree of freedoms in all directions. The material model used for this plate was defined by MAT-RIGID card in LS-Dyna. Since the material properties of the steel plate have not been described in the Challita reference, the material properties described in the Barber reference were used and listed in (Table 3.2).

A piezoelectric quartz transducer with an area of 12x 12 mm² was modeled, using 144 solid elements, on the plate at different positions (center, 1" above center). The MAT-RIGID card was defined in Ls-Dyna to model the material of this transducer which has the material properties presented in (Table 3.3).

Using equation (3.1), the density of birds with masses of 1.814 kg (4 lb) and 3.628 Kg (8 lb) is derived equal to 942.7 Kg/m³ and 923.73 kg/m³, respectively. Table 3.7, summarizes the bird model parameters for both weights, 4 lb and 8 lb, which have been modeled with 38,734 particles for each weight.

Table 3.7. 4lb and 8lb, bird SPH model parameters.

Bird model	4lb (1.814 kg)	8lb (3.628 kg)
	rho= 942.70 E-9 Kg/mm ³	rho= 923.73 E-9 Kg/mm ³
	D= 113.71 mm	D = 144.24 mm
	R= 56.85 mm	R = 72.12 mm
	Lc= 113.71 mm	Lc= 144.24 mm
	L = 227.42 mm	L= 288.48 mm

3.3. Validation of the 4 lb and 8 lb Bird Impact Models on a Rigid Flat Plate

The 4 lb and 8 lb bird impact behaviors onto the rigid flat plate at different velocities, have been assessed for two angles of impact, normal 90° and oblique 45° as shown in Figures (3.12, 3.14, 3.16, 3.18), where the 4 lb bird impact duration, "t" was, $t = 1.229142E-03(s)$,

and $t = 3.33845E-03(s)$, for the normal, and oblique impact, respectively; and the 8 lb bird impact duration, “t” was, was, $t = 1.88834E-03(s)$, and $t = 3.68156E-03(s)$, for the normal, and oblique impact, respectively.

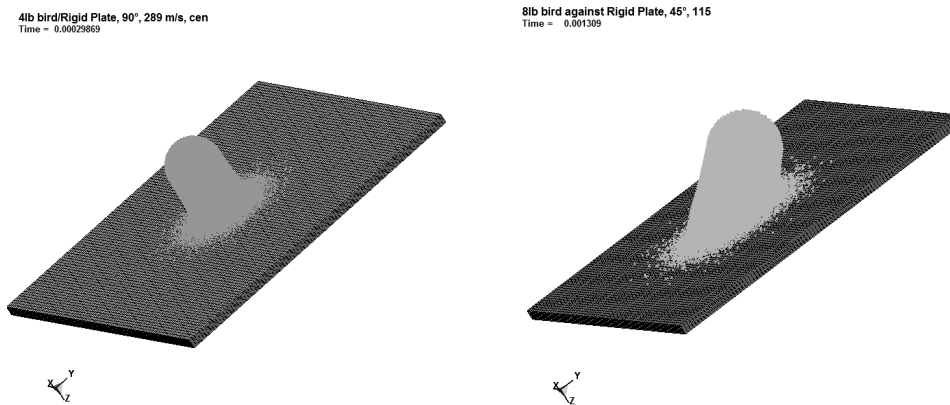


Fig.3.11. Normal impact model of 4lb bird and oblique impact model of 8lb bird, onto a rigid flat plate

Figures 3.13, 3.17, show plots of the contact force versus time, on the center and 1” above the center, of the rigid flat plate obtained from the simulation, where for the normal impact of 4lb bird at 289 m/s, a peak value of $27.4 E+6$ mN was read for the contact force, which corresponds to a peak pressure of 190.27 MPa. The peak pressure of the contact was evaluated in terms of ratio between the peak force and the impact surface, which was taken equal to 144 mm^2 . For the normal impact of 8lb bird at 245 m/s, a peak value of $14.9 E+6$ mN was read for the contact force, which corresponds to a peak pressure of 103.47 MPa.

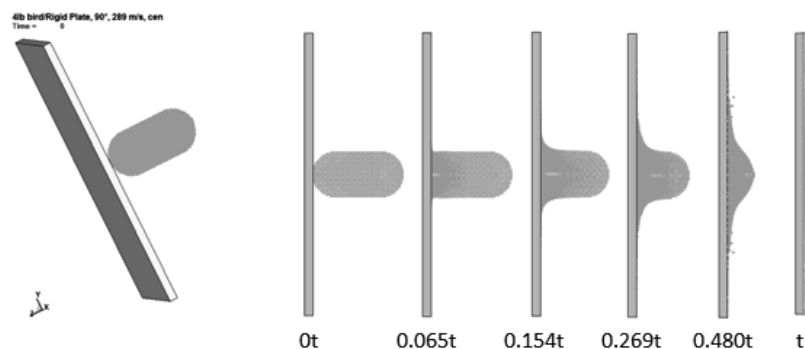


Fig 3.12. Normal 4 lb bird impact scenario on the rigid plate at 298 m/s

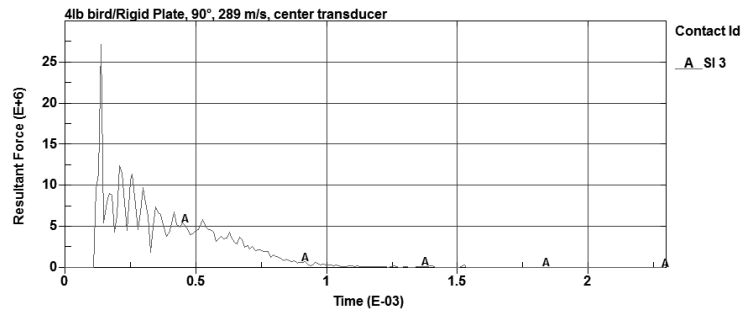


Fig 3.13. Plot of the contact force (N) vs time (s) for normal 4lb impact (90°)

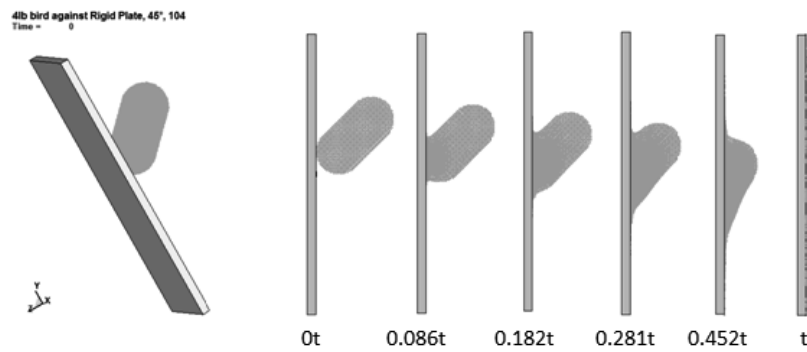


Fig 3.14. Oblique 4 lb bird impact scenario on the rigid plate at 104 m/s

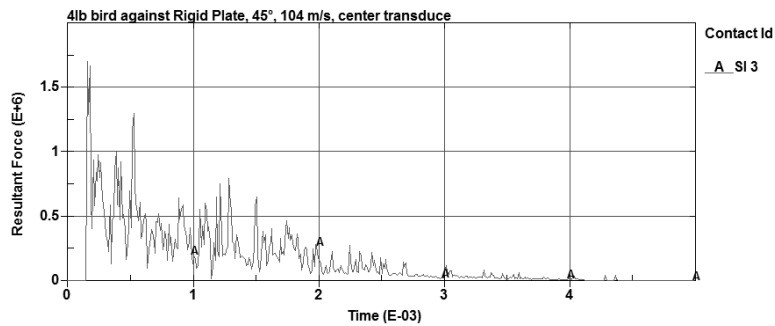


Fig 3.15. Plot of the contact force (N) vs time (s) for oblique 4 lb impact (45°)

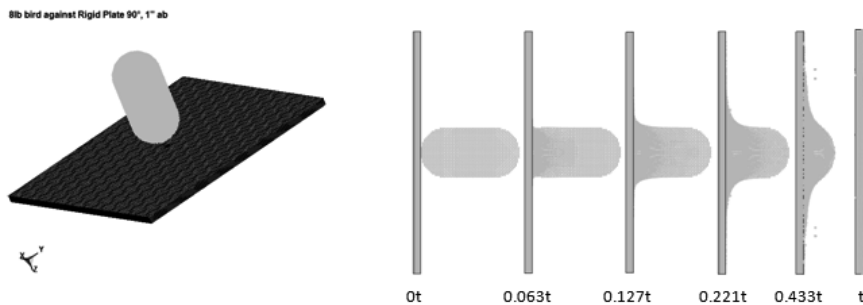


Figure 3.16. Normal 8 lb bird impact scenario on the rigid plate at 245 m/s

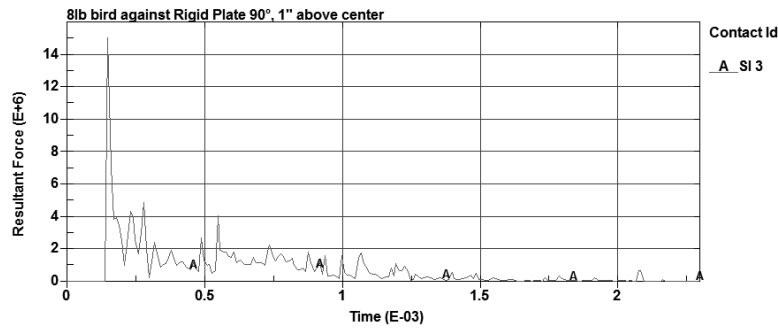


Fig 3.17. Plot of the contact force (N) vs time (s) for normal 8 lb impact (90°)

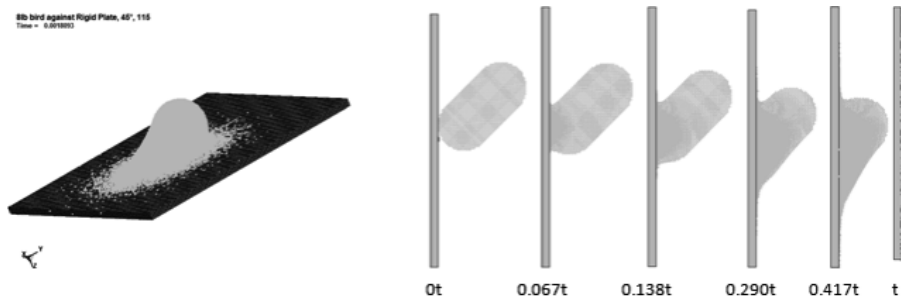


Figure 3.18. Oblique 8 lb bird impact scenario on the rigid plate at 115 m/s

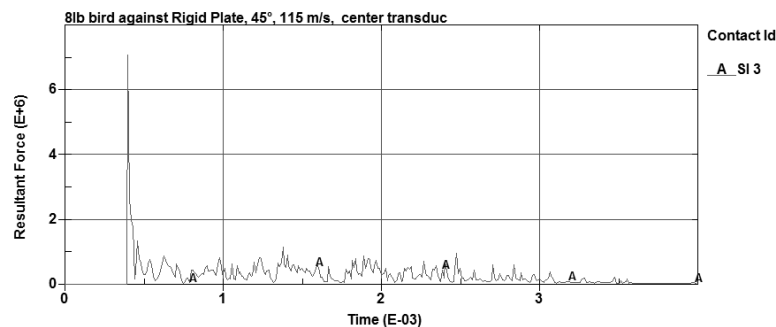


Fig 3.19. Plot of the contact force (N) vs time (s) for oblique 8lb impact (45°)

The comparison between the numerical results and the experimental results [77], for the normal (90°) and oblique (45°) impact of 4lb and 8 lb bird at different velocities (289 m/s, 104 m/s, 245 m/s, 115 m/s), shows that an excellent agreement was achieved with an error less than 7% (see Table 3.8).

Table.3.8. Comparison between numerical and the experimental results

	Contact force (mN)	Simulated pressure (MPa)	Experimental pressure (MPa)	Error (%)
4 lb, 90°	27.4E+6	190.27	203.72	6.60
4 lb, 45°	1.72 E+6	11.94	12.48	4.32
8 lb, 90°	14.9E+6	103.47	108.24	4.40
8lb, 45°	7.1 E+6	49.30	48.14	2.40

4. BIRD IMPACT SCENARIOS ON RIGID FLAT AND HIGHLY CURVED CONFIGURATIONS

A parametric analysis was carried out to investigate the influence of the structural geometry of the target on the bird impact response. By considering the surface rigidity of the target, the bird impact behavior was determined independent of the constitutive response of the structure. In order to identify the effect of high curvature shape on the bird impact behavior the leading edge structure was considered. 4 lb and 8 lb bird impact behaviors at 129 m/s have been assessed for two different structures: rigid flat plate and rigid leading edge as shown in Figures 3.20 and 3.21. From these numerical results the bird impact scenario was identified to be generally similar in both the rigid plate and the rigid leading edge. However, some differences have been seen.

The contact area during impact between the bird and the leading edge was limited compared to the contact area on the flat plate which was approximately four times greater than the bird area, Figure 3.20. This was explained by the propagation of the majority of bird outwards the leading edge because of its high curvature; in contrast to the large propagation of the bird on the flat plate.

Additionally, the duration of impact was registered to be slightly less on the rigid leading edge than on the flat plate. The difference between the impact duration, on the rigid plate and the rigid leading edge, was found equal to 0.449 ms for the impact of 4 lb bird and 0.820 ms for the impact of 8 lb bird.

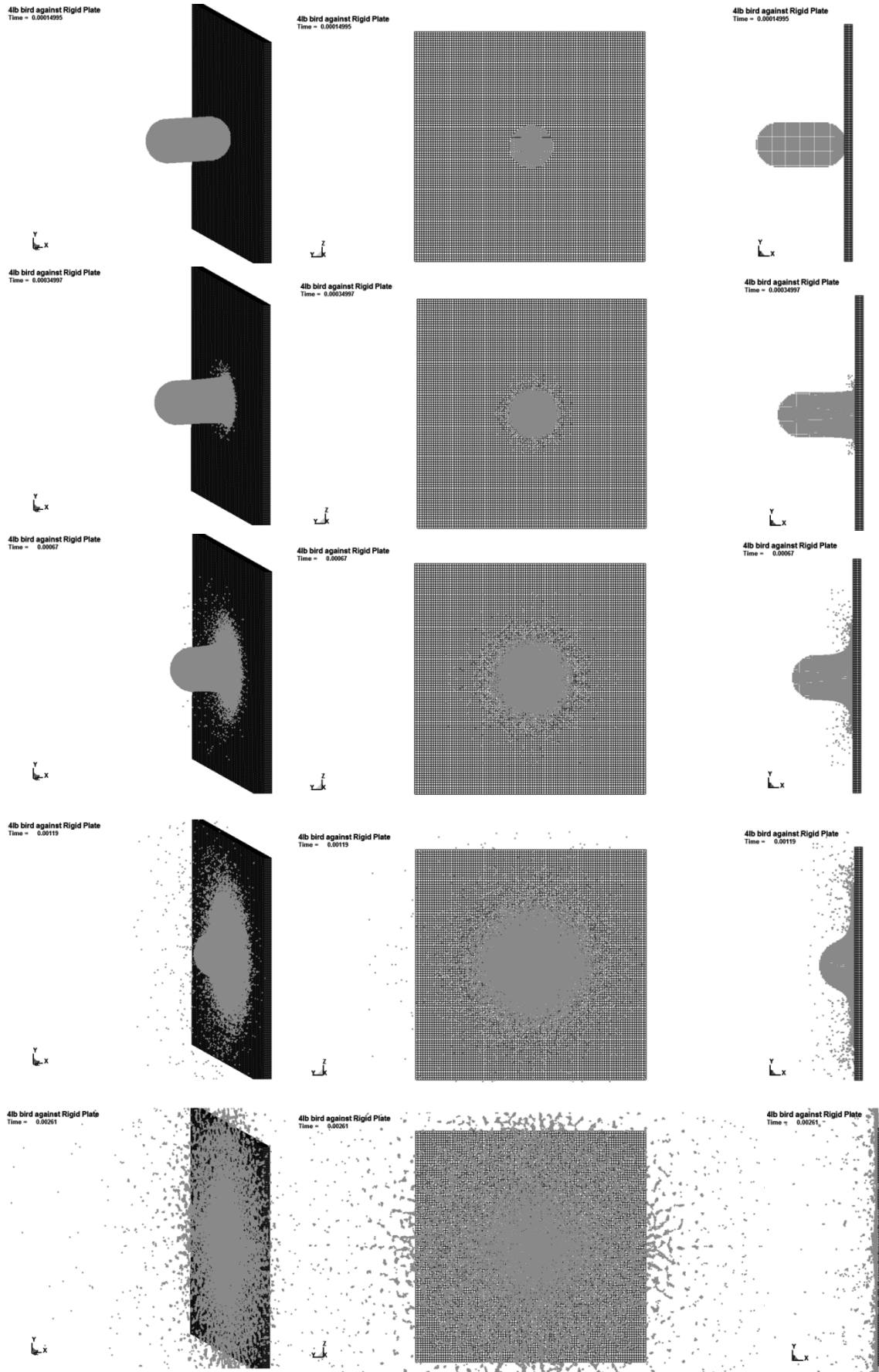


Figure 3.20. Different views of the bird impact on a rigid flat plate at 129 m/s

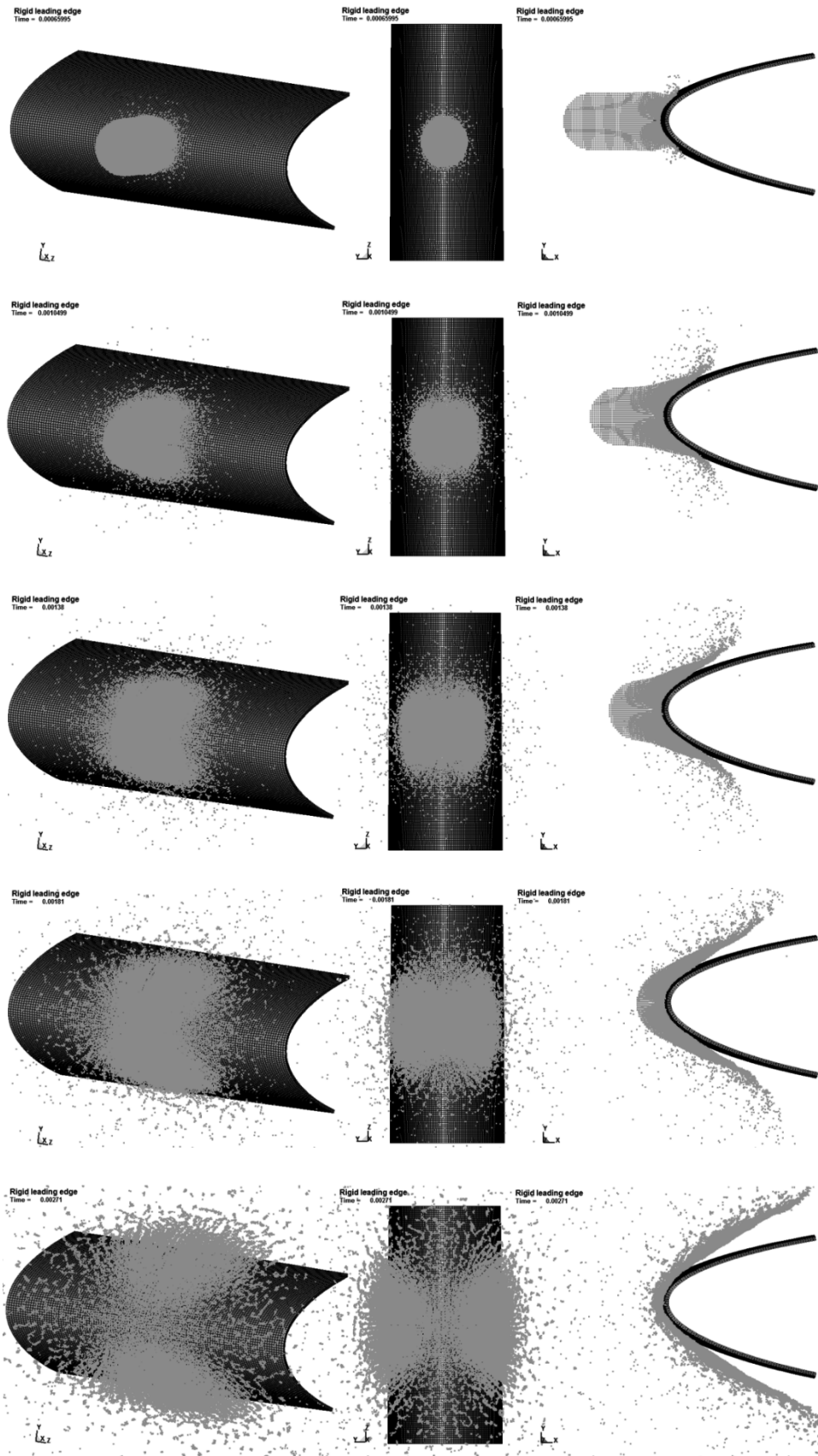


Figure 3.21. Different views of the bird impact scenario onto a rigid leading edge bay at 129 m/s

5. TEST DATA FOR LARGE SIZES OF BIRD, 4 lb, IMPACTING A DEFORMABLE LEADING EDGE BAY WITH RIBS

5.1. GUIDA's Experimental Test data for large sizes of bird (4 lb) impacting a Composite FML leading edge bay

The experimental test presented in the reference [82], had been selected as reference for the validation of the bird impact model. A comparison between the numerical results concerning bird impact on FML sandwich leading edge obtained in the current section with the experimental test results [30] will be considered. The test was conducted using an air pressure gun, dummy birds was fired at a speed of 129 m/s on a FML leading edge structure which was attached to a solid steel support frame. The arrangement of the test is shown in (Figure. 3.22). The operating procedure consisted in holding the bird inside a sabot packed with expanded polystyrene and fired it by applying a pressure above the predetermined test pressure using a hand operated hydraulic pump. The velocity of the bird was measured by two photocell mounted between the muzzle and the sabot separator. Two high-speed cameras up to 10,000 fps were used to visualize the impact sequence. The projectile impacted just inside the leading edge at mid height just onto the target. The experimental deformation at last step of the impact on the leading edge structure was taken as reference for the validation of the bird impact model.



Figure.3.22. the arrangement of the test [82]

The leading edge bay represents a portion of the real leading edge configuration of a C27-J aircraft and consists of an aluminum back spar web 1.22 mm thickness and a hybrid lay-up with FML “Fiber Metal Laminate” supported by two main aluminum ribs 2 mm thick at 631 mm pitch, and shown in (Figure.3.23). The span length of the leading edge bay was 640 mm and the depth at the back spar was 320 mm. The FML skin of the bay consists of

three Al 7475 T761 layers, each aluminum layer having a thickness of 0.3 mm alternated with four layers of glass fibers embedded in an epoxy resin, FM 94-27%- S2- Glass- 187- 460. Each composite fiber/epoxy layer having a thickness of 0.125 mm. The FML's stacking sequence was: Al/G0°/G90°/Al/G90°/G0°/Al, and giving a total thickness of the skin of 1.4 mm.



Figure.3.23. View the leading edge bay [30]

5.2. Finite Element Modeling of the Composite FML Leading Edge Bay

A single shell with 19,308 elements that incorporates the properties of the hybrid lay-up was adopted to model the FML lay-up of the leading edge bay (see Figure. 3.24). In particular, the composite has the mechanical properties listed in Table 4.3 (Chapter 4) and the aluminum has the mechanical properties listed in Table 4.4 (Chapter 4). The Glass fiber/epoxy composite was modeled as a composite orthotropic material with brittle failure where the three failure criteria [Chang and Chang 1987a, 1987b] were defined [82], and the aluminum 7475 T761 was modeled as an isotropic elasto-plastic material with failure based on the plastic strain. The MAT-COMPOSITE-DAMAGE card in LS-DYNA was used to define the Glass fiber/epoxy composite, while the MAT-PIECEWISE-LINEAR-PLASTICITY card was used to define the aluminum. The aluminum ribs were modeled with 6,542 shell elements where the link between the skin and the ribs was modeled using 142 CNRB constrained nodal rigid body elements (Figure.3.24).

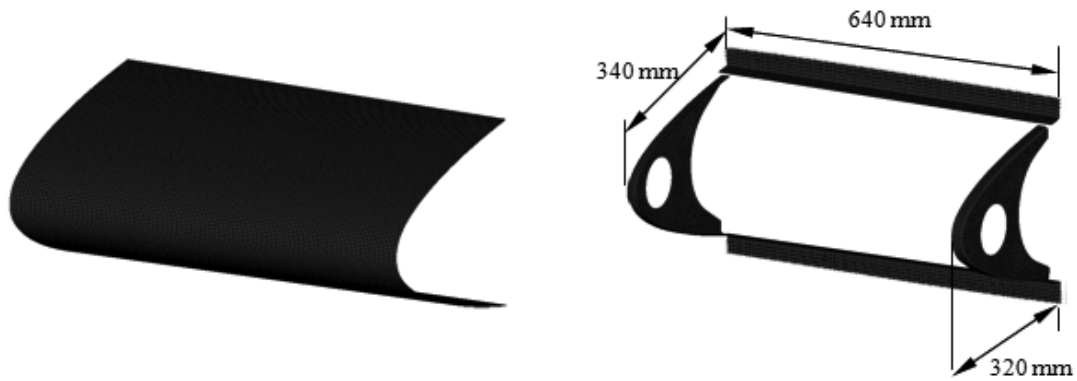


Figure. 3.24. Finite element model of the LE bay

5.3. Prediction of the Bird Impact Scenario on the Composite FML LE Bay

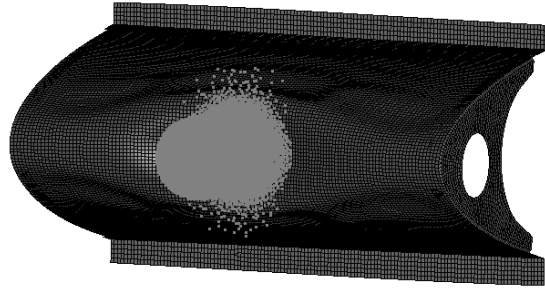
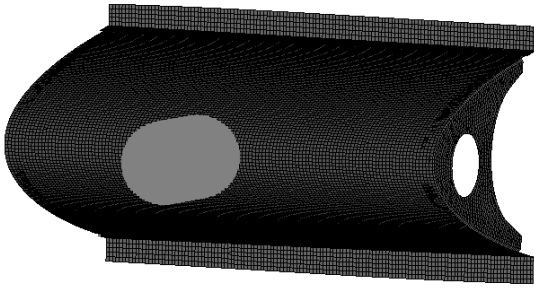
After its validation onto the rigid plate (section 4.1), the 4 lb bird model is now used to perform the impact simulation on a deformable leading edge bay at 129 m/s. The 4 lb bird impact scenario coupled with the response of the composite FML leading edge bay were predicted as shown in Figure 3.25.

5.4. Validation of the 4 lb Bird Impact Model on a Composite FML Leading Edge Bay

Figure 3.26, presents the final shape obtained from the simulation of the composite FML leading edge bay after been impacted by 4lb bird at velocity of 129 m/s, where a total deformation of the skin has affected the back spar without any perforation of the skin, the distance between the ribs at the last phase of impact was measured equal to 237.20 mm. As is shown in Figure 3.27, the distance between the ribs obtained experimentally [22] was measured equal to 220 mm. Correlating the numerical results with the experimental results an excellent agreement was achieved with an error less than 5%. This good accordance was not only seen in the distance between the ribs but also on the final shape of the leading edge bay after the impact.

4lb bird impact on GLare Al 7475 LE bay
Time = 0

4lb bird impact on GLare Al 7475 LE bay
Time = 0.0007198

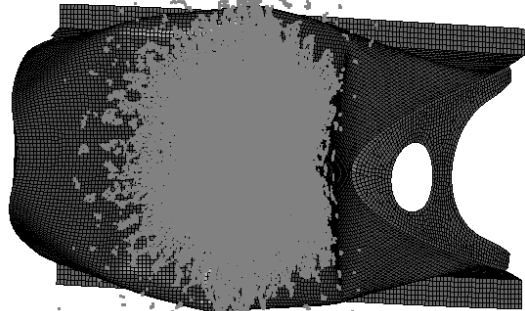
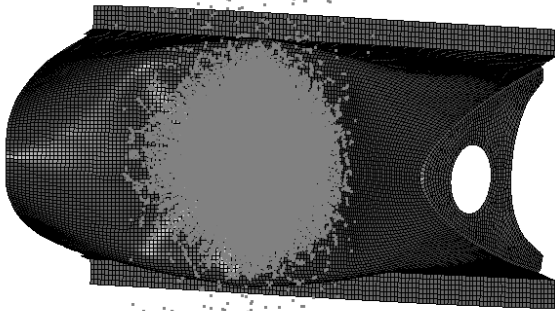


Y
X Z

4lb bird impact on GLare Al 7475 LE bay
Time = 0.0018897

Y
X Z

4lb bird impact on GLare Al 7475 LE bay
Time = 0.0029696

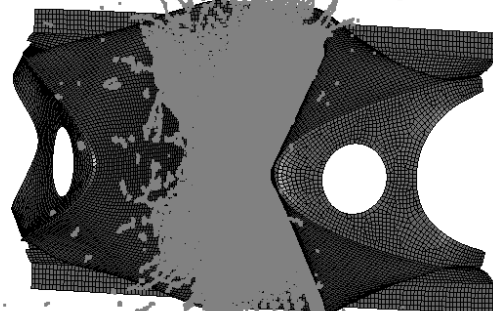
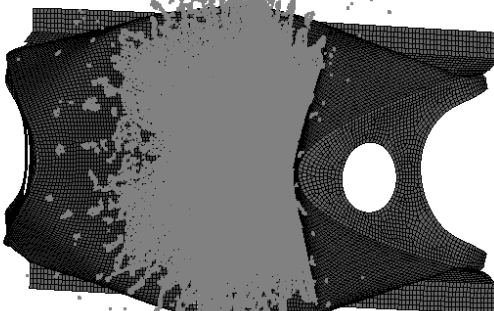


Y
X Z

4lb bird impact on GLare Al 7475 LE bay
Time = 0.0038698

Y
X Z

4lb bird impact on GLare Al 7475 LE bay
Time = 0.0050004



Y
X Z

Y
X Z

Figure 3.25. Bird impact scenario onto a deformable FML leading edge bay at 129 m/s

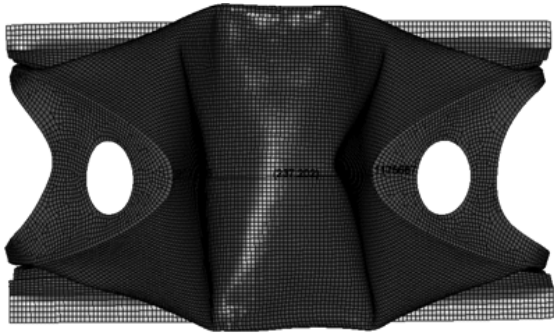


Fig. 3. 26. Numerical simulation results obtained for the impact of 4lb bird onto the FML LE bay at 129 m/s

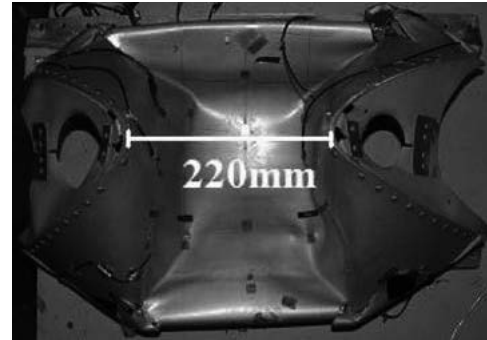


Fig. 3. 27. Experimental results for the impact of 4lb bird onto the FML LE bay at 129 m/s [22]

6. TEST DATA FOR LARGE SIZES OF BIRD, 8 lb, IMPACTING A C27J AIRCRAFT TAILCONE LEADING EDGE MADE OF SANDWICH FML MATERIAL

6.1. GUIDA's Experimental Test Data

A real C27J aircraft leading edge structure was tested for the impact of 8lb bird with a velocity of 129 m/s that presents the cruise speed of the aircraft. The real C27J leading edge was ribless and presents a length of 2970 mm, with a chord that varies between 450 mm and 750 mm and a sweepback angle of 63°. 8lb dummy bird was fired at a speed of 129 m/s on a sandwich FML leading edge structure which was attached to a solid steel frame (see Figure 3.28).

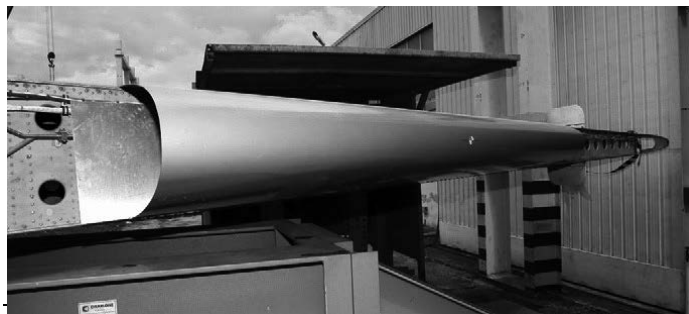


Fig. 3.28. View of a model of real C27J aircraft leading edge [82]

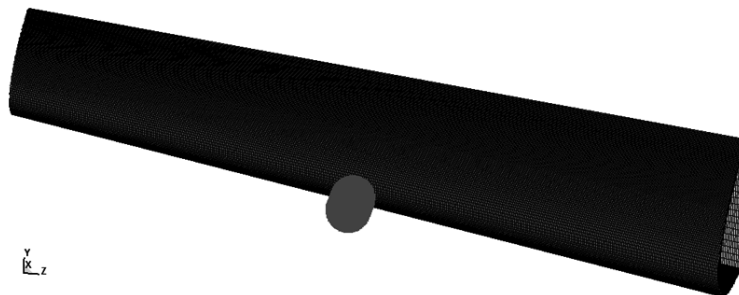
The leading edge consists of two main parts: a spar made of aluminum 2024-T3 alloy 0.8 mm thick and a sandwich FML lay-up configuration which consists of: an outboard ply in FML with a thickness of 1.4 mm, a core made of Aluminum 5052 honeycomb flexcore F40-0.0019 [87] having a cell height of 6.35 mm, a core cell size of 7.62 mm and a core cell wall thickness of 0.048 mm, as well as an inboard ply made of aluminum 2024 T3 alloy with a thickness of 0.3 mm (see Table 3.9). The total thickness of the configuration was 8.05 mm.

Table 3.9. The sandwich FML configuration of the C27J leading edge

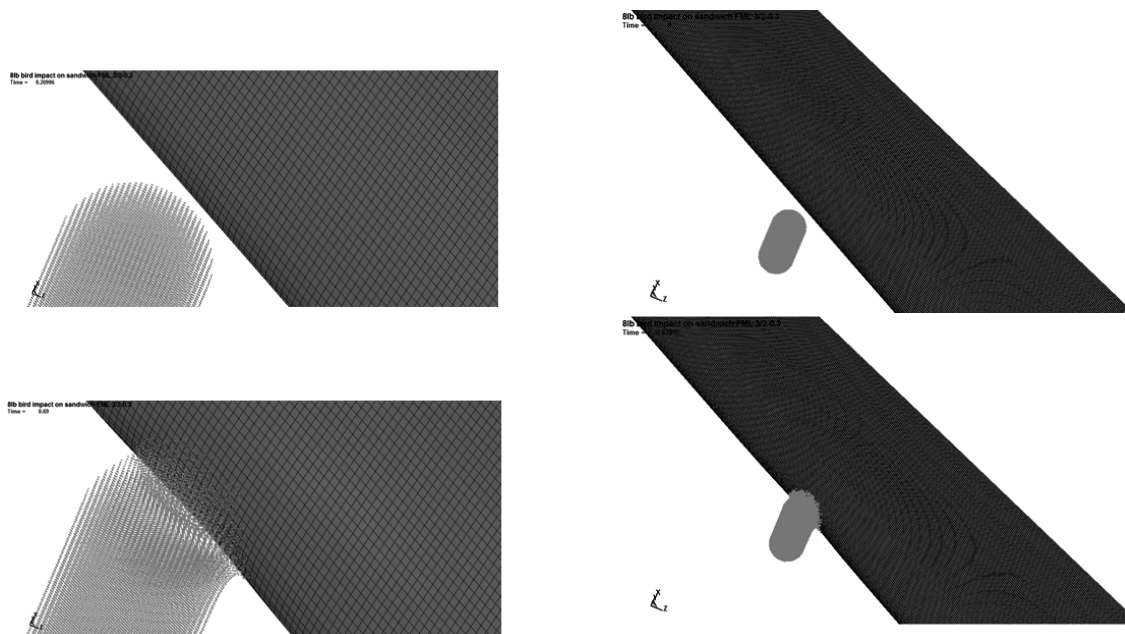
Sandwich lay-up of the ribless LE	Material	Thickness
Upper skin	FML	1.4 mm
Honeycomb flexcore	F40-0.0019- Al 5052	6.35 mm
Inner skin	Al 2024 T3	0.3 mm

6.2. FE Modeling of the Ribless Sandwich FML Leading Edge

The FML outboard ply of the C27J leading edge was modeled with 72,000 shell elements and the honeycomb core was modeled with 144,000 eight-node solid elements. The inboard ply was modeled with 72,000 shell elements (see Figure 3.29) and the spar was modeled with 11,200 shell elements (details on modeling are presented in chapter 4).

**Fig.3.29.** View of the finite element model of the ribless C27J leading edge

6.3. Prediction of the Bird Impact Scenario on the Ribless Sandwich FML Leading Edge



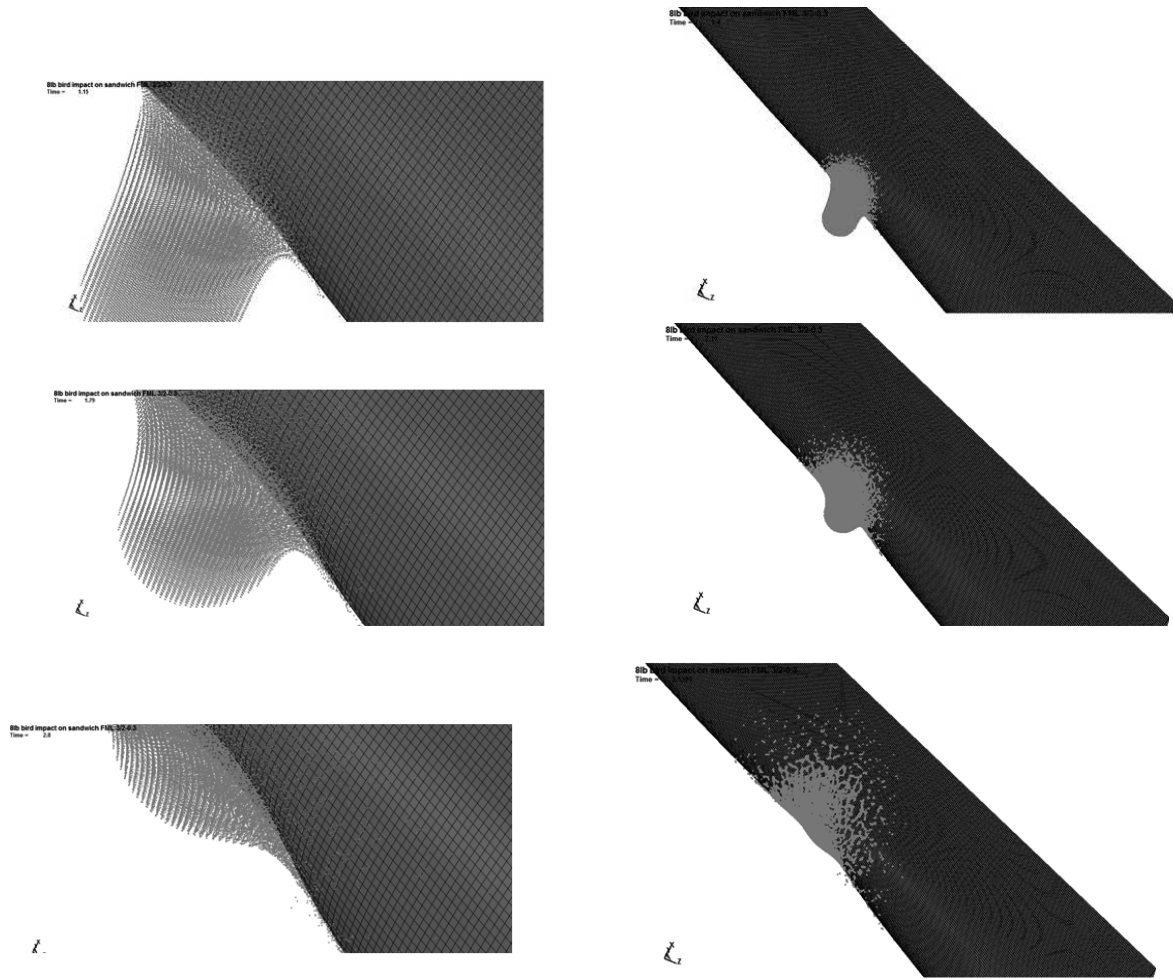


Figure 3.30. bird impact scenario onto real C27J aircraft leading edge at 129 m/s, made of sandwich FML material



Figure.3.31. Final shape of the ribless sandwich FML LE after the 8 lb bird impact at 129 m/s

The response scenario of the ribless leading edge under the 8 lb bird impact at 129 m/s was predicted and shown in Figure 3.30. Figure 3.31 shows the final shape of the leading edge after the impact where a significant deformation has occurred to the sandwich FML lay-up of the leading edge without affecting the spar, while no perforation was seen in the skin of the leading edge.

6.4. Validation of the 8 lb Bird Impact Model on the Ribless Leading Edge

Figure 3.32 presents the final shape of the sandwich FML leading edge, in different views, after being bitted by an 8lb bird at 129 m/s. The results data about the numerical test are reported in Figure 3.34, and summarized in Table 3.10 together with the experimental results obtained by Guida [82] for the same test. The maximum depth of the skin was registered to be equal to 97 mm, as shown in Figure 3.34. The displacement time history of the central node on the leading edge is reported in Figure 3.35.

From the figures below (Fig. 3.32 and Fig 3.34) it can be seen that the skin did not suffer any perforation and the structure was able to absorb the bird impact energy without any major failure. The comparison of the final deformed shape of the leading edge in the numerical and the experimental test shows very similar residual deformed behavior.

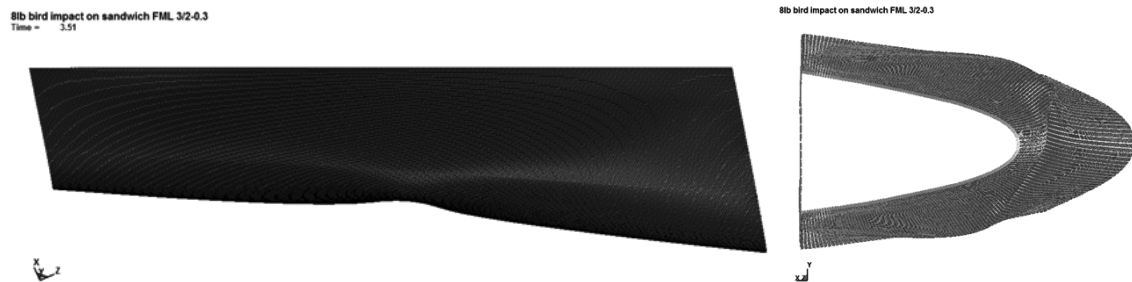


Figure. 3.32. Different views of the ribless sandwich FML LE after the 8 lb bird impact at 129 m/s



Figure.3.33. Ribless sandwich FML LE after impact of 8 lb bird at 129 m/s, Exp [82]

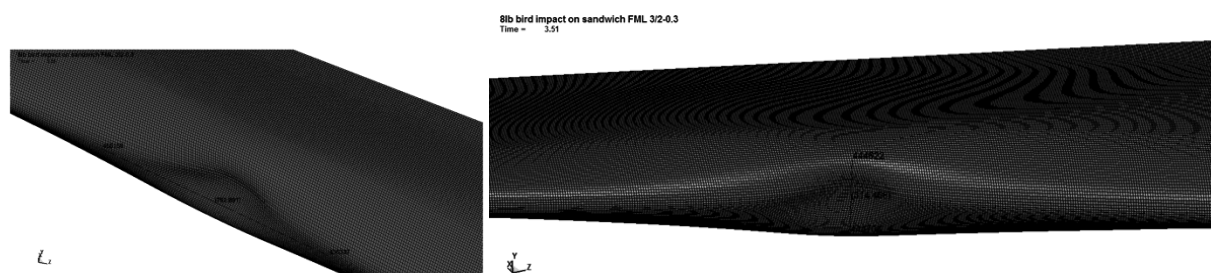


Figure. 3.34. Front view of the ribless sandwich FML LE after the 8 lb bird impact at 129 m/s

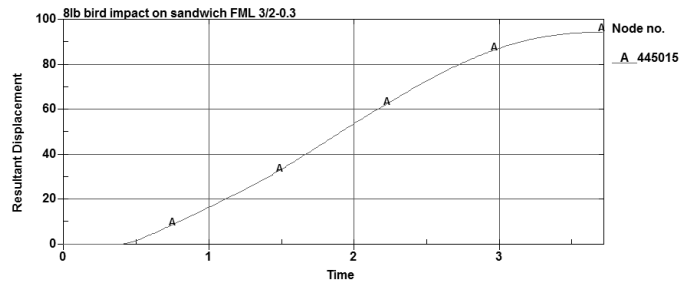


Figure 3.35. Time history (ms) of the central node displacement (mm) on the upper skin of the ribless LE

Table 3.10. Sandwich FML LE deformation measurements

Data results (mm)	<i>Max depth</i>	<i>Length</i>	<i>wide</i>
Experimental [37]	117	-	-
Numerical	97	752.891	314.458

CHAPTER 4

**NUMERICAL
TESTS &
CERTIFICATION
OF NEW
DESIGNED LE
STRUCTURES**

I. INTRODUCTION TO SANDWICH STRUCTURES

Sandwich structures are generally made, of two thin and stiff skins, of lightweight materials such as aluminum or fiber reinforced composite laminates, separated by a thick, lightweight core in different structures, including foam/solid core, honeycomb, truss core, and web core, which can be manufactured by using a variety of base materials, e.g., metal foils, plastic foils, or resin impregnated paper-like materials made of synthetic or natural fibers, which increases the inertia of the resulting section without significantly increasing the mass (Figure 4.1). The strength of the sandwich structure comes from the combination of the properties of the face sheets, core and the interface [89]. The core stiffness against deformation in out-of-plane direction and in shear should be high [90]. The face sheets resist the in-plane and bending loads, and the core resists transverse shear loads [91]. In some cases the face sheet thicknesses or the material may vary; for example in an application where one face should withstand high temperatures, corrosive environment, etc. [91]. Sandwich structures have several application fields such as aviation, automotive, wind energy, civil engineering, etc. There are several advantages of using sandwich structures; such as up to 30% weight savings compared to conventional structures, high flexural stiffness-to-weight ratio, good thermal, fatigue, acoustical insulation properties, resistance to local deformations providing aerodynamic efficiency, and easy mass production [90].

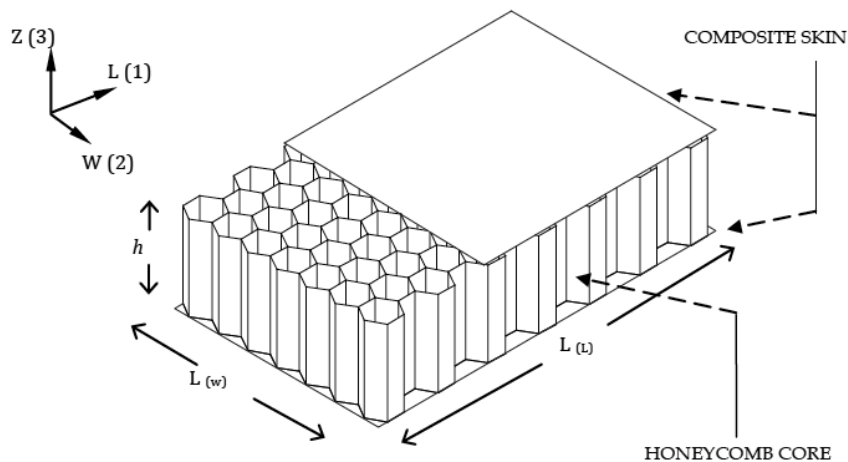


Figure.4.1. Schematic representation of a sandwich structure

They can carry both in-plane and out-of-plane loads. Several different failure modes may occur under these different loadings. These modes are summarized in Figure 4.2. The geometrical

and material differences between the facings and the core cause instabilities at global and local scales. If compressed in the in-plane direction the sandwich structure may fail due to the skin buckling or core wrinkling. Wrinkling may occur in the form of symmetrical or antisymmetrical as shown in Figure 4.2.

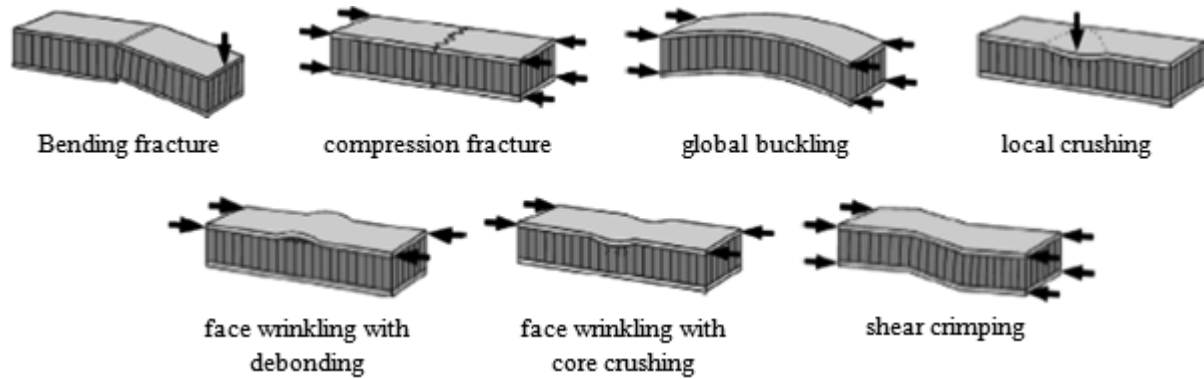


Figure. 4.2. Sandwich structure failure modes [92]

Sandwich structures can be combinations of variety of materials depending on the requirements. One of these combinations is the composite sandwich structure, which is generally used in commercial aircrafts. The composite sandwich structures are used both interior and external structure of the aircrafts as shown in Figure 4.3. The interior applications are fairings and the floor panels in passenger compartment. The typical external applications are the radar domes, belly fairings, engine cowlings, leading and trailing edge fairings and landing gear doors. Composite sandwich construction is most often fabricated using autoclave cure, press cure, or vacuum bag cure. Skin laminates may be precured and subsequently bonded to core, co-cured to core in one operation, or a combination of the two methods. Examples of honeycomb structure are: wing spoilers, fairings, ailerons, flaps, nacelles, floor boards, and rudders. Radar domes and leading edge fairings are exposed to impacts due to bird and lightning strikes and the abrasion caused by rain and dust. Furthermore, foreign object damage caused by runway debris is another important problem for the lower side of the aircraft.

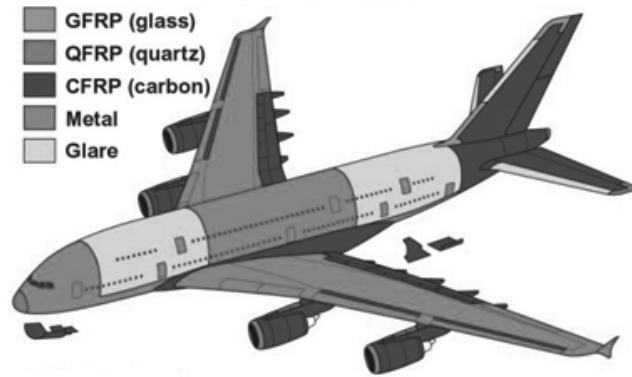


Figure 4.3. Composite sandwich applications in A380 [93]

The aircraft design is a complicated process, for which many parameters relating safety regulations should be taken into account [94]. In addition to these design parameters, environmental effects such as bird strike and runway and tire debris impacts have to be considered in the designing stages. The design should include the materials that may withstand crash and impact loads. Consequently, the material's strain-rate sensitivity, energy absorption and deformation mechanisms are needed to be characterized at increasing high deformation rates in order to reach reliable material properties in the designing stage.

In order to take precautions against the bird impacts, the tests that simulate component behavior must be performed on the structural materials.

I.1. FML Facing Sheet

Most honeycomb structures used in aircraft construction have aluminum, fiberglass, Kevlar, or carbon fiber face sheets. FMLs are hybrid structures based on stacking thin sheets of metal alloy and plies of fiber-reinforced polymeric materials. The idea of fiber metal laminates is in order to gain the superiority fatigue and fracture characteristics of fiber reinforced composite materials and to combine with the plastic behavior and durability of the metal. A typical FML configuration is as shown in Figure 4.4. Three main families of fiber metal laminate in aerospace industry are defined by their fiber-reinforce laminate's constituent as, Aramid Reinforced Aluminum Laminate (ARALL), Glass Reinforced Aluminum Laminate (GLARE) and Reinforced Aluminum Laminate (CARALL). Other less commercialized FML are titanium based and magnesium based FMLs. In comparison to ARALL, GLARE has advantages in terms of

higher tensile strength, higher compressive strength, higher failure strain, superior impact resistance and does not absorb moisture. However GLARE has higher specific weight and lower stiffness than ARALL. In higher energy impact, a crack of aluminum will be followed by severe damage in the fiber-reinforced laminate layers. However magnesium and titanium based FML were proven not as good as aluminum based FML in terms of impact resistance.

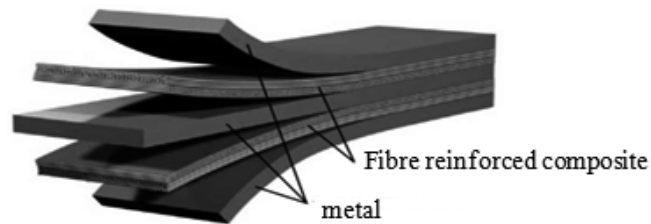


Figure 4.4. A typical fiber metal laminate

1.1.1. GLARE: Glass Reinforced Aluminum Laminate

GLARE, is a glass fiber reinforced aluminum laminate and is commercialized in six different grades as shown in Table 4.1. Composite in GLARE is all based on advanced unidirectional glass fibers which are embedded within epoxy FM94 adhesive with a nominal fiber volume fraction of 60% [95, 96]. Aluminum alloy 2024-T3 is the metal used in all GLAREs except in GLARE 1 that utilizes stronger aluminum alloy 7475-T6. Prepreg is stacked symmetrically in GLARE except for GLARE 3 and GLARE 6. Due to tougher and slightly stiffer properties of 2024-T3, GLARE 2 and 3 has better impact resistance than GLARE 1. In standard practice, a coding system is used to specify GLARE grades. GLARE Grades are described using the following notation: *GLARE X – n/n-1 – t*, where *X* is the grade/sub-grade, *n* the number of metal sheets, *n-1* the number of GRP layers and *t* the sheet thickness. An example of GLARE 3-3/2-0.3 is shown in figure 4.5.

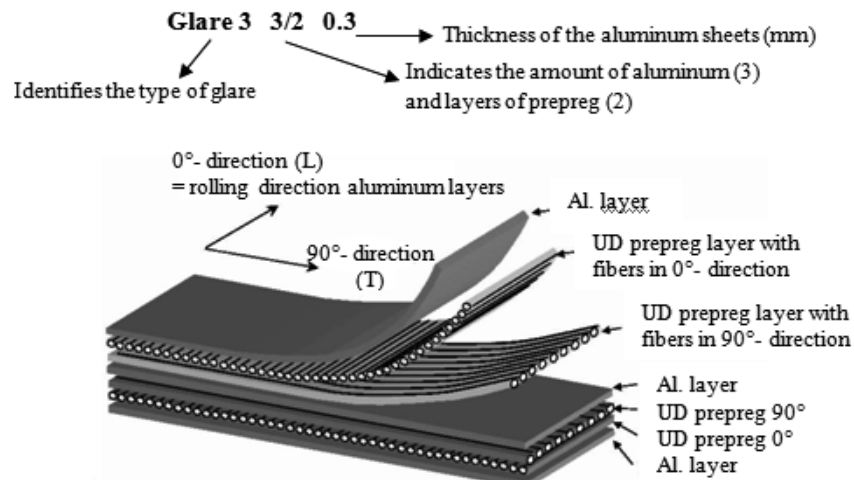


Figure 4.5. Structure of GLARE

Table 4.1. Standard Glare grades

Glare grade	Sub grade	Metal sheet thickness (mm) & alloy	Prepreg orientation * in each fibre layer**	Main beneficial characteristics
Glare 1	-	0.3-0.4 7475-T761	0/0- 90/90	Fatigue, strength, yield stress
Glare 2	A	0.2-0.5 2024- T3	0/0	Fatigue, strength
	B	0.2-0.5 2024- T3	90/90	Fatigue, strength
Glare 3	-	0.2-0.5 2024- T3	0/90	Fatigue, impact
Glare 4	A	0.2-0.5 2024- T3	0/90/0	Fatigue, strength in 0° direction
	B	0.2-0.5 2024- T3	90/0/90	Fatigue, strength in 90° direction
Glare 5	-	0.2-0.5 2024- T3	0/90/90/0	impact
Glare 6	A	0.2-0.5 2024- T3	+45/-45	Shear, off-axis properties
	B	0.2-0.5 2024- T3	-45/ +45	Shear, off-axis properties

GLARE that has already been used to construct the top half fuselage skin in Airbus A380 has a potential to be used as bottom half of the fuselage skin in the near future as it has excellent impact resistance [110]. In fact it is being evaluated for use as cockpit crown, forward bulkheads and leading edges in which they are the area that require most excellent impact resistance material [111].

1.1.2. GLARE Benefits for Aeronautical Applications

GLARE has properties that exceed aircraft grade aluminum alloys in many categories. The benefits for aeronautical applications in particular are summarized below:

1.1.2.1. Fatigue crack growth

Fatigue crack growth is a very common, yet complex problem faced by aerospace and many other products. Although prediction techniques have been developed, such as the Palmgren-Miner method, one can never be too certain of the occurrence of failure due to fatigue cracks. This is detrimental to the safety of the airplane or spacecraft. Materials with better resistance to rapid crack growth have always been sought. Schijve found that FMLs have smaller crack growth rates when compared to monolithic materials (single unreinforced materials) because of crack bridging and delamination effects [97]. This is said to be one of the advantages of GLARE.

With crack bridging, some of the loads normally borne by the aluminum layers are transferred to the fibers. Due to this, additional shear stress occurs at the metal composite interface. For a given laminate thickness, thinner metal layers allows for more fibers, which is thought to result in small shear stresses at the interface. While these shear stresses create delaminations, the loads sustained by the fibers are reduced, resulting in fewer breaks [98]. A situation similar to fiber bridging is known as fiber nesting which removes some of the strain energy away from the crack tip [98]. Fig. 4.6; is an illustration of the crack bridging phenomena.

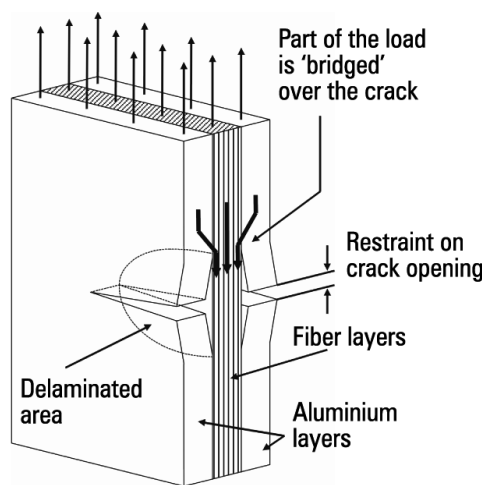


Figure 4.6: Schematic of the fatigue-crack growth mechanism in GLARE [99]

1.1.2.2. Residual strength

Apart from its fatigue crack growth resistance, GLARE is at least equal, if not superior, to monolithic aluminum in retaining its strength in the presence of cracks, holes, cut-outs etc. This effect is attributed to the inherent damage tolerance of the fiber reinforced layers. Investigation of the performance of GLARE specimens with outer skin, partial and through cracks has revealed that GLARE in general exhibits adequate residual strength in the case of through cracks (severe impact damage, rivet holes) and aluminium sheet fatigue cracks (unaffected fiber layers) but GLARE 3 is found to be vulnerable to part-through cracks as failure initiates in the fiber layers and fiber bridging mechanism is inhibited.

1.1.2.3. Fire burn-through

Comparative tests conducted on samples and panels showed that GLARE can withstand exposure to flame temperatures of around 2500 °C for about two minutes, while aluminum alloys of similar thickness are penetrated in only a few seconds. These results are attributed to the high melting temperature (about 1500° C) of glass fibers and to char formation due to resin burning. As fire melts away the outer aluminum face the first GRP layer acts like a protective fire barrier slowing down (or even stopping in the case of temperatures below 1500°C) flame penetration. In addition, delamination between the intact layers provides an effective insulation keeping the inside of the panel at reasonably low temperatures.

1.1.2.4. Impact damage

Resistance to impact loading is an important aspect of the performance of aeronautical materials. In respect to impact, material performance must be evaluated based on two parameters. The extent of damage induced to the material due to an impact event and the ability of the damage structure to carry the service loads safely. GLARE materials perform efficiently to both low and high velocity impact. At low impact energies the behavior is similar to aluminum. Small dents occur on the aluminum layers due to plastic deformation without any delamination of the underlying layers. As impact energies increase matrix cracking and minor delamination in the dented layers is developed. At high velocity impact, cracking or even perforation of the material is observed. At high impact velocities GLARE performance is remarkably improved compared to aluminum due to the strain hardening effect and strain rate dependent behavior of the fibers.

1.1.2.5. Blast loading

The response of GLARE materials to explosive blast loading is only recently started to attract research attention. A significant achievement in this area was the FAA certification of the first blast-proof luggage container that was constructed with GLARE panels (Galaxy Scientific ECOS3 HULD). Work on GLARE variants that utilize woven glass reinforced polypropylene, reports that the extent of damage due to localized blast effects depend mainly on total panel thickness. As the panel thickness increases, behavior deviates from monolithic plate response and debonding failures are seen. There are indications that the progressive nature of the failure mechanisms within a FML panel could be advantageous for containing blast loading compared to the sudden, catastrophic failure of metal containers that zip open (petalling failure) and allow the blast energy to escape.

Ballistic tests have concluded that the main energy absorbing mechanisms are bending and membrane deformation, delamination and tensile fracture. Membrane and bending contribute as much as 90% of the total absorbed energy. Delamination although it requires a small amount of the impact energy to develop, enables layers to function under membrane loads.

The response to far-field blast events is expected to be positive as high strain loading of GLARE is found to be superior to that of monolithic alloys. This behavior is mainly attributed to the high strain rate hardening of glass fibers (reported by many authors) and to their relatively high strain to failure values.

1.1.2.6. Inspection-Maintenance

One of the greatest advantages of GLARE materials for aeronautic applications is their compliance with standard inspection methods for metallic materials. Fatigue and impact damage can be easily detected using ultrasonics, eddy current techniques and visual inspection. In addition the inherent damage tolerance characteristics of GLARE allow for longer inspection intervals. Maintenance is also straightforward as riveted or bonded patch repair works for GLARE structures with the same efficiency as with aluminum alloys.

I.2. Honeycomb Core

The use of honeycomb structures as core material in sandwich panels is widely diffused in many engineering applications, especially where high mechanical performances and low density are requested. The main key performance factors of honeycombs are represented by the capability to withstand through the thickness compression and to absorb energy by plastic deformation of the cell walls. Given the heterogeneous nature of honeycomb sandwich structures, damage may affect both composite skins and honeycomb core. Generally, in the aerospace industry honeycomb structures are made of aluminum foils, phenolic-impregnated Nomex paper or carbon honeycomb, given their superior weight-specific mechanical properties in terms of stiffness and structural weight reduction [100-102]. Furthermore they offer design versatility and cost-efficient manufacturing [103]. However, the closed structure of honeycomb cells may lead to negative effects regarding condensed water trapped in the cells and trigger an increase in weight as well as a reduction of mechanical properties. To overcome this issue, new configurations for core structures, such as folded cores [104], have been recently introduced. In particular, the manufacturing process is described in [105] and a wide range of experimental results can be found in [106].

Most honeycomb structures show a similar mechanical behavior under out-of-plane (i.e., through-thickness direction) compression. In particular, they are characterized by:

- (i) an initial linear-elastic regime up to the buckling limit and a subsequent compressive strength reduction;
- (ii) a plateau of constant stress, named crush strength, corresponding to a progressive degradation of cell walls;
- (iii) a final segment of densification characterized by the compression of the cell wall itself.

However, honeycomb structures can exhibit different features in their compressive out-of-plane behavior depending on the nature of the honeycomb core constituent material. In particular, when the critical compressive stress is reached, the cells begin to collapse by elastic buckling, plastic yielding or brittle fracture, depending on the wall material type. Hanel et al. [107] investigated the influence of the different paper materials, i.e., Kevlar and Nomex, on the structural properties

of wedge-shaped folded cores, whereas other authors investigated the structural behavior of a honeycomb structure made of Nomex paper material, making comparison with a honeycomb core made of aluminum [108]. They report that Nomex material is much more brittle than aluminum foil during the progressive failure mechanism and the crushing regime.

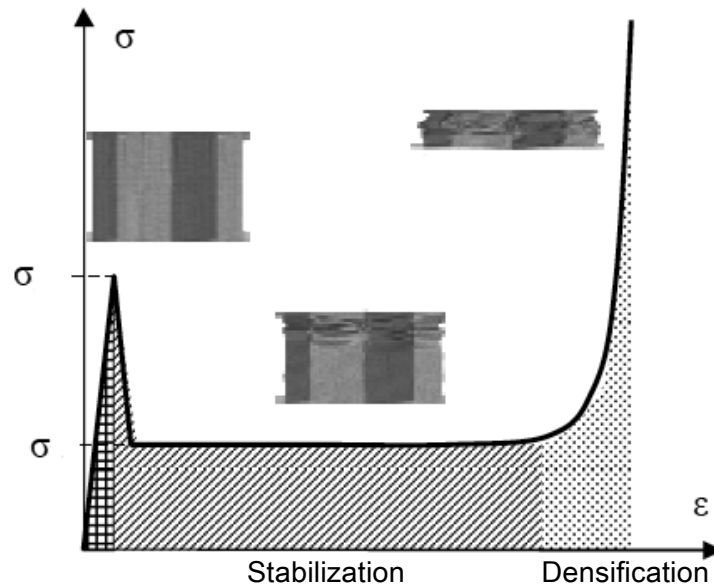


Figure 4.7. Theoretical behavior of honeycomb cell in compression

1.2.1. Honeycomb Manufacturing Process

The most common manufacturing method of honeycomb structures is the adhesive bonding followed by an expansion process [109], reported in Figure 4.8.

The expansion process begins with the stacking of sheets of the substrate material on which adhesive node lines have been printed. The adhesive lines are then cured to form a HOBE (Honeycomb Before Expansion) block. The HOBE block itself may be expanded after curing to give an expanded block. Slices of the expanded block may then be cut to the desired T dimension. Alternately, HOBE slices can be cut from the HOBE block to the appropriate T dimension and subsequently expanded. Slices can be expanded to regular hexagons, under expanded to 6-sided diamonds, and over expanded to nearly rectangular cells. The expanded sheets are trimmed to the desired L dimension (ribbon direction) and W dimension (transverse to the ribbon).

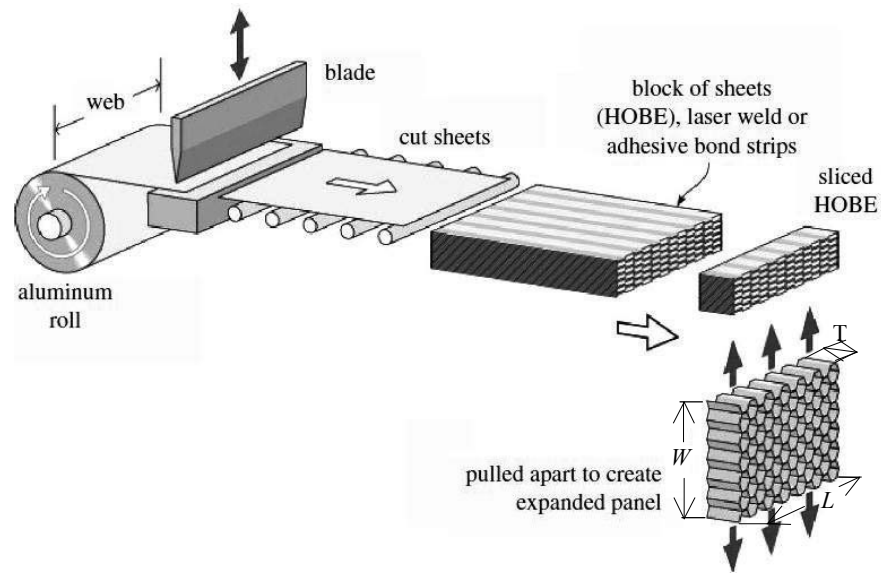


Figure 4.8. Expansion manufacturing process for honeycomb material

The corrugated process of honeycomb manufacture is typically used to produce products in the higher density values. This process starts with the application of the adhesive to the corrugated nodes; then, the corrugated sheets are stacked into blocks and the node adhesive cured. Sheets of honeycomb material are cut from these blocks to the required core thickness (Figure 4.9).

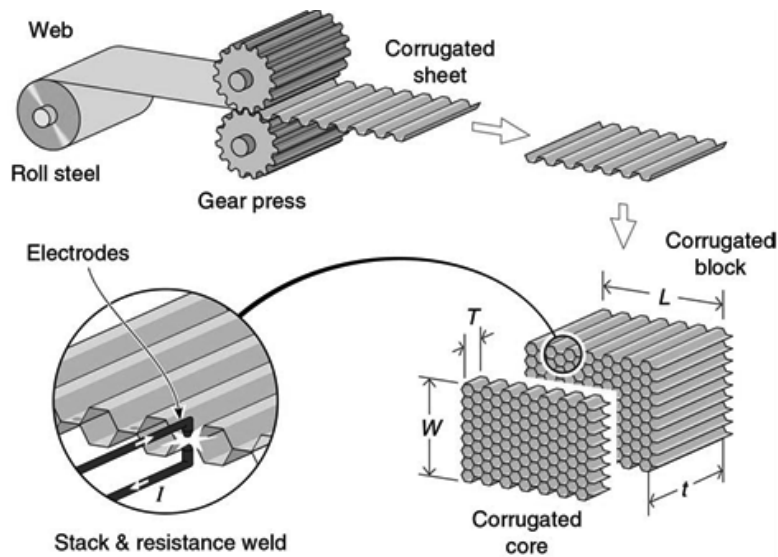
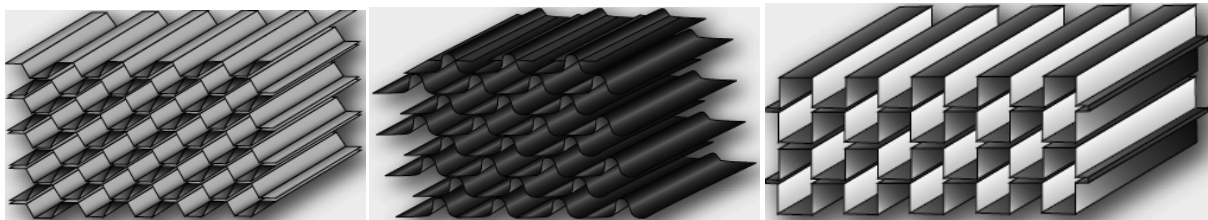


Figure 4.9: Corrugated manufacturing process for honeycomb material

1.2.2. Honeycomb Core Cells Configurations

Honeycomb core cells for aerospace applications are usually hexagonal. The cells are made by bonding stacked sheets at special locations. The stacked sheets are expanded to form hexagons. The direction parallel to the sheets is called ribbon direction. Bisected hexagonal core has another sheet of material cutting across each hexagon. Bisected hexagonal honeycomb is stiffer and stronger than hexagonal core. Overexpanded core is made by expanding the sheets more than is needed to make hexagons. The cells of overexpanded core are rectangular. Overexpanded core is flexible perpendicular to the ribbon direction and is used in panels with simple curves. Bellshaped core, or flex-core, has curved cell walls that make it flexible in all directions. Bell-shaped core is used in panels with complex curves.



Hexagonal Honeycomb core

Flexcore

Overexpanded core

Figure 4.10. Honeycomb density [112]

1.2.2.1. Flex-Core cell configuration provides for exceptional formability in compound curvatures with reduced anticlastic curvature and without buckling the cell walls. Curvatures of very tight radii are easily formed. When formed into tight radii, Flex-Core provides higher shear strengths than comparable hexagonal core of equivalent density. Flex-Core is manufactured from aluminum, Nomex, and fiberglass substrates [87].

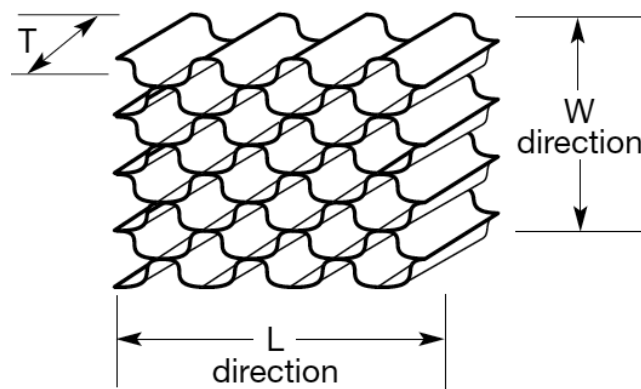


Figure 4.11. Bellshaped core, or flex-core honeycomb

1.2.3. Honeycomb Mechanical Properties and Test Methods

The test methods used for the honeycomb properties listed in reference [87] by Hexcel are outlined below.

1.2.3.1. Compressive Properties

- a. **The stabilized compressive strength**, (also called flatwise compressive strength) represents the ultimate compressive strength of the honeycomb when loaded in the T direction, as shown in Figure 4.12.

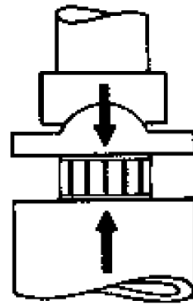


Figure 4.12. Compressive test

- b. **The stabilized compressive modulus**, is determined from the slope of the initial straight-line portion of the stress-strain curve. Some honeycomb materials exhibit a linear initial stress-strain relationship, while other honeycomb materials exhibit a nonlinear curved initial stress-strain relationship. The bare compressive strength is the ultimate compressive strength of the core when loaded in the T direction without stabilization of the cell edges. The value is normally used for an acceptance criteria since this test is easier and faster to perform.

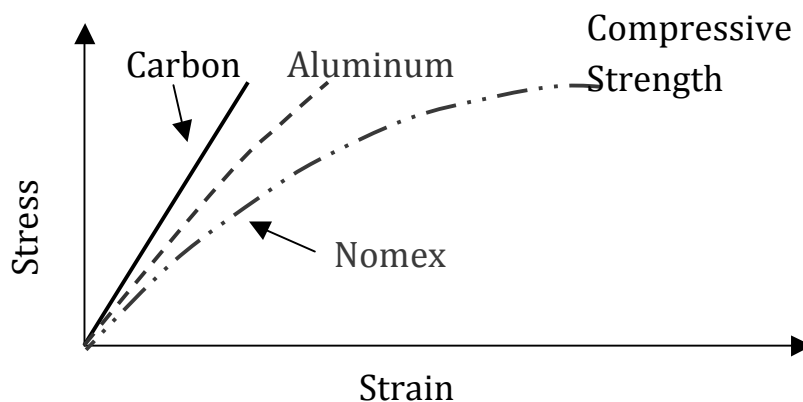
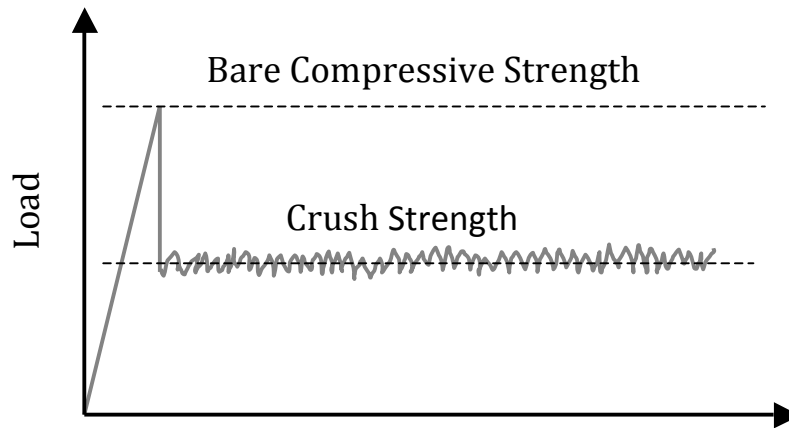


Figure 4.13. General honeycomb initial compressive stress- strain curves*1.2.3.2. Crush Strength*

After honeycomb has exceeded its ultimate compressive strength, it will continue to deform plastically and crush uniformly. The load-deflection curve shows such a typical response.

**Figure 4.14.** Typical load-deflection curve

The average crush load per unit cross-sectional area is defined as the crush strength. Honeycomb will crush at virtually a constant stress level (dependent on the core material and density), hence its absorption capacity is predictable, making it ideal for energy absorption applications. When used in this manner, the core is often precrushed slightly to remove the compressive peak in the load-deflection curve. The crush strength of honeycomb decreases with increasing angle loading from the thickness.

Fixed loading and bearing plates are used for crush strength tests. It should be noted that the crush strength values presented in reference [87] are typical static test results. It has been found that under dynamic loading, these values increase nonlinearly with impact velocity, and numbers as much as 30% higher have been reported.

1.2.3.3. L and W Shear Properties

The shear strength of honeycomb refers to the ultimate stress when a shear load is applied parallel to the L–W plane. The shear modulus is the slope of the initial straight-line portion of the stress-strain curve. The values so obtained are dependent upon the orientation of the applied

loading with respect to the L and W dimensions, being highest in the L direction and lowest in the W direction. The shear strength and modulus values presented in [87] were obtained using the compressive and/or tensile plate shear method.

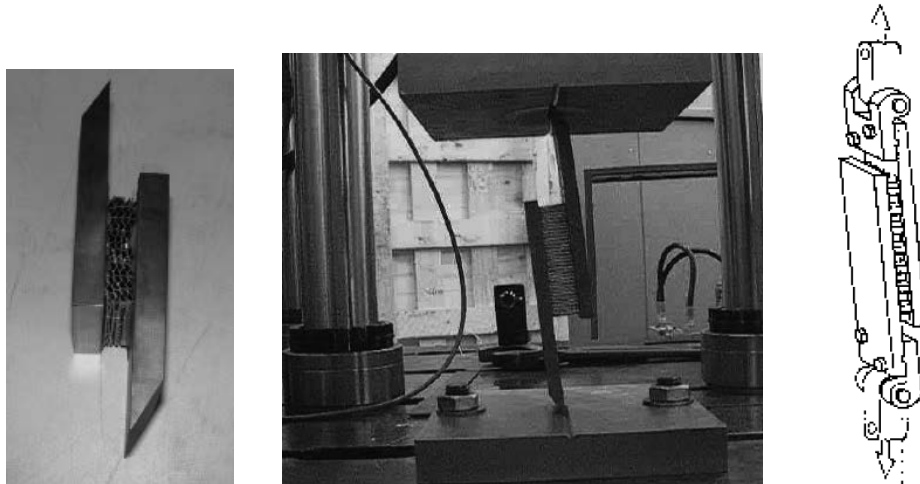


Figure 4.15. Tensile plate shear

The elastic behavior prior to cell wall buckling and the complex crushing behavior characterized, by cell wall folding mechanisms at micro/meso scale can be reproduced, using a numerical method, by reproducing the exact shape of the core structure, even though the large required computational time. Moreover, numerical technique allows gathering mechanical properties which are usually not available among experimental manufacturer databases. This kind of approach is usually pursued to model honeycomb or folded core materials by using different scales ranging from one single cell scale to large scale including the full honeycomb model. An example of this numerical approach can be found in recent studies performed by Heimbs and concerning virtual testing of sandwich panels manufactured with Nomex honeycomb and folded cores [104].

II. NUMERICAL TEST OF BIRD IMPACT ON SMALL SCALE OF A LEADING EDGE

II.1. Test Article Description

Before starting the bird impact analysis on a real aircraft leading edge, some preliminary tests were performed on a small sample of the leading edge for material characterization. Various material configurations were tested for the layup of the leading edge specimen with birds with nominal weight of 4lb and 8lb, and with an impact velocity of 129 m/s, which corresponds to the

requirements demanded by FAA. The analyzed specimen represents a simplified leading edge bay which was extracted by the real leading edge configuration of a C27-J aircraft, Figure 4.16, that represents a portion of a box spar to which the leading edge subassembly is attached. The structure consists of a back spar web with a thickness of 1.22 mm and a skin reinforced by two main ribs with 2 mm thick at 631 mm pitch. The span wise length of the specimen was 640 mm and the depth at the back spar was 320 mm. Assembly was by 4 mm diameter hillock at 25 mm pitch. A typical dimension of the bay is shown in Figure 4.16. The explicit finite element software LS-DYNA was chosen for these numerical investigations. A number of different impact scenarios have been considered on various configurations of the specimen. The main points subjected to variation have been: thickness and materials. Details on the whole model of bird impact on the leading edge bay are presented below.

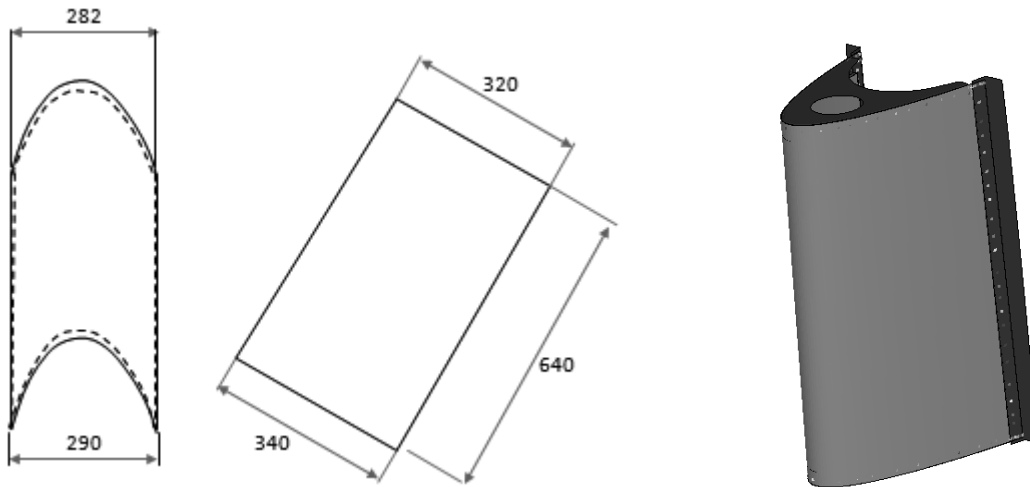


Figure 4.16. One bay leading edge specimen

II.2. FE Model, Material Model & Constitutive Law

The finite element model of the leading edge bay was based on, two aluminum 2024 T3 alloy ribs modeled with 6542 shell elements with a thickness of 2 mm, and a leading edge skin supported by the ribs. The link between the skin and the ribs was modeled using 142 CNRB constrained nodal rigid body elements. The ribs were constrained at the edges of L-shape beams (Figure .4.16). The finite element model of the bay of the leading edge is shown in Figure 4.17. Details on modeling the LE skin are reported below.

The validation of the impact model for 4 lb and 8 lb birds was achieved in the previous chapter (3); henceforth the same bird models were impacting with an angle of 90° at a velocity of 129 m/s the presented leading edge bay.

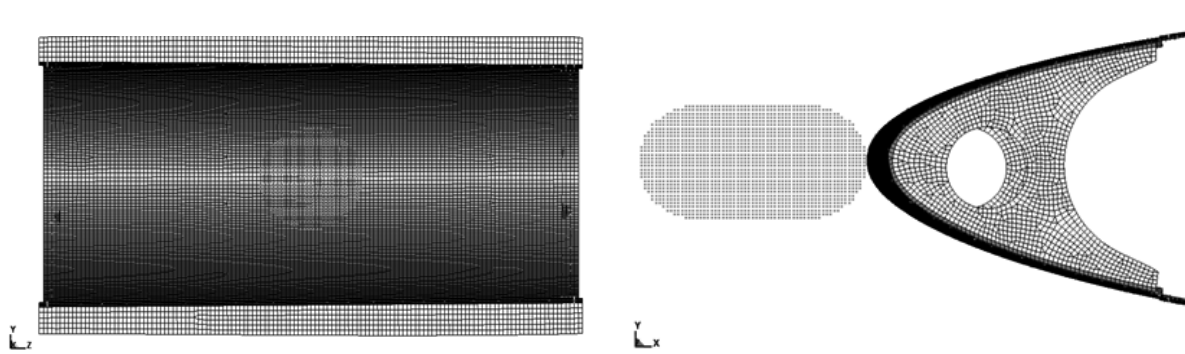


Figure 4.17. Finite element model of the LE

Three different material configurations have been adopted for the skin of the leading edge bay as follow:

II.2.1. Metallic Configuration, The aluminum alloy considered for the skin of the metallic LE configuration has 25 percent higher strength in T6 temper than 6061T6, and has improved toughness, fatigue, strength and stretch characteristics compared to 6061 with equivalent stress corrosion characteristics [85]. The Al 6013 T6 Alloy skin was 2.54 mm thick and was modeled with 19308 shell elements. It was treated as an isotropic elasto-plastic material with a failure based on a plastic strain where the mechanical properties used are reported in Table. 4.2.

Table. 4.2. Mechanical properties of Al 6013 T6 Alloy [85]

ρ (Kg/m ³)	E (GPa)	ν	σ_y (MPa)	E_t (GPa)	Elongation at break
2713	69	0.33	324	32	10%

II.2.2. FML Configuration, the FML considered for this configuration consists of three Al 7475 T761 layers, each layer has a thickness of 0.3 mm, altered with four layers of glass fibers embedded in an epoxy resin, FM 94-27%- S2- Glass- 187- 460, each layer has a thickness about 0.125 mm, with a stacking sequence as: [Al/G 0° /G 90° /Al/G 90° /G 0° /Al]. The total thickness of the FML was about 1.4 mm. A single shell with 19308 elements that incorporate the properties of the hybrid skin was adopted to model the FML skin: in particular the composite has the

mechanical properties listed in Table.4.3, and the aluminum has the mechanical properties listed in Table.4.4. Aluminum 7475 T761 was modeled as an isotropic elasto-plastic material with failure based on the plastic strain

The Glass fiber/epoxy composite was modeled as composite orthotropic material with brittle failure where three failure criteria were defined which use the following material parameters [Chang and Chang 1987a, 1987b]:

- S_1 , longitudinal tensile strength;
- S_2 , transverse tensile strength;
- S_{12} , shear strength;
- C_2 , transverse compressive strength;
- α , nonlinear shear stress parameter.

S_1 , S_2 , S_{12} , and C_2 are obtained from material strength measurement, α is defined by material shear stress-strain measurements. In plane stress, the strain is given in terms of the stress as

$$\left. \begin{aligned} \varepsilon_1 &= \frac{1}{E_1} (\sigma_1 - \nu_1 \sigma_2) \\ \varepsilon_2 &= \frac{1}{E_2} (\sigma_2 - \nu_2 \sigma_1) \\ 2\varepsilon_{12} &= \frac{1}{G_{12}} \tau_{12} + \alpha \tau_{12}^3 \end{aligned} \right\} \quad (46)$$

The third equation defines the nonlinear shear stress parameter α .

A fiber matrix shearing term augments each damage mode:

$$\bar{\tau} = \frac{\frac{\tau_{12}^2}{2G_{12}} + \frac{3}{4}\alpha\tau_{12}^4}{\frac{S_{12}^2}{2G_{12}} + \frac{3}{4}\alpha S_{12}^4} \quad (47)$$

which is the ratio of the shear stress to the shear strength. α was set to 0.1.

- The matrix cracking failure criteria is determined from

$$F_{matrix} = \left(\frac{\sigma_2}{S_2}\right)^2 + \bar{\tau} \quad (48)$$

where failure is assumed whenever $F_{matrix} > 1$. If $F_{matrix} > 1$, then the material constants E_2 , G_{12} , ν_1 and ν_2 are set to zero. S_2 was set to 75 MPa [82].

- The compression failure criteria is given as

$$F_{comp} = \left(\frac{\sigma_2}{2S_{12}}\right)^2 + \left[\left(\frac{C_2}{2S_{12}}\right)^2 - 1\right] \frac{\sigma_2}{C_2} + \bar{\tau} \quad (49)$$

where failure is assumed whenever $F_{comp} > 1$. If $F_{comp} > 1$, then the material constants E_2 , ν_1 , and ν_2 are set to zero. S_{12} and C_2 were set to 75 MPa [82].

- The final failure mode is due to fiber breakage.

$$F_{fiber} = \left(\frac{\sigma_1}{S_1}\right)^2 + \bar{\tau} \quad (50)$$

Failure is assumed whenever $F_{fiber} > 1$. If $F_{fiber} > 1$, then the constants E_1 , E_2 , G_{12} , ν_1 , and ν_2 are set to zero. S_1 was 725 MPa [82].

Table.4.3. Mechanical properties of FG FM 94-27%-S2-Glass-187-460 [86]

ρ (Kg /m ³)	E_1 (GPa)	E_2 (GPa)	E_3 (GPa)	ν_{12}	ν_{13}	ν_{23}	G_{12} (GPa)	G_{13} (GPa)	G_{23} (GPa)
1974	53.2	9.3	9.3	0.279	0.279	0.49	5.495	5.495	3.121

Table.4.4. Mechanical properties of Al 7475 T761 Alloy [85]

ρ (Kg/m ³)	E (GPa)	ν	σ_y (MPa)	E_t (GPa)	Elongation at break
2810	70.3	0.33	420	40	12%

II.2.3. Sandwich- FML flexcore Configuration, The sandwich FML flexcore configuration of the leading edge bay was about 8.05 mm thick and consists of the following parts:

- *An outboard skin made of Fiber Metal Laminate (FML);*

- A honeycomb core made of Al 5052 flexcore;
- An inboard skin made of Al 2024-T3 alloy.

II.2.3.1. FML outboard skin: the FML outboard skin consists of the same FML discussed in section II.2.2.

II.2.3.2. Aluminum flexcore honeycomb: The honeycomb designed by, F40- 0.0019- 5052- 3.1 pcf [87], was considered as a core of the sandwich configuration of the LE bay, it is a Hexweb flexcore manufactured from aluminum 5052 alloy with a core height 6.35 mm, a core cell size 7.62 mm and a core cell wall thickness about 0.048 mm (Figure 4.17), has the mechanical properties as listed in Table.4.5 [87]. This honeycomb core was modeled with 65948 eight-node solid elements as an orthotropic crushable material, where the mathematical formulation comprises of two almost independent deformation phases. The first is referred to as not compacted phase. In this phase, the behavior is orthotropic and the components of the stress tensor are uncoupled. The second is referred to as fully compacted phase. The second stage is in essence a computational means to preclude the size of a brick finite element become equal to zero.



Figure 4.18. Unit cell of F40- 0.0019- 5052- 3.1 pcf honeycomb

The stresses in the not compacted phase are functions of a brick element relative volume V defined as

$$V = \frac{v}{v_f} \quad (51)$$

where: v is the element volume, v_f is the volume of the fully compacted element.

The compression and shear moduli in the not compacted phase vary from their initial values the fully compacted values.

$$E_{ii} = E_{ii}^{un} + \beta(E^{com} - E_{ii}^{un}), \quad G_{ij} = G_{ij}^{un} + \beta\left(\frac{E^{com}}{2(1+\mu)} - G_{ij}^{un}\right) \quad (52)$$

where: E^{com} is the compression modulus in the fully compacted phase, E_{ii}^{un} and G_{ij}^{un} are the compression and shear moduli in the not compacted phase, μ is Poisson's ratio, and β is computed from the following expression

$$\beta = \max\left[\min\left(\frac{1-V}{1-V_f}, 1\right), 0\right] \quad (53)$$

where : V_f is the relative volume of fully compacted brick element.

In the present work, the stresses in the not compacted phase are updated using a stress-relative volume curve obtained numerically by modeling the dynamic crushing of a single cell of F40- 0.0019- 5052 in the out of plane direction at a velocity of 129 m/s as shown in Figure 4.19, and following trial stresses

$$\sigma_{ii}^{n+1^{trial}} = \sigma_{ii}^n + E_{ii}\Delta\varepsilon_{ii}, \quad \sigma_{ij}^{n+1^{trial}} = \sigma_{ij}^n + 2G_{ij}\Delta\varepsilon_{ij} \quad (54)$$

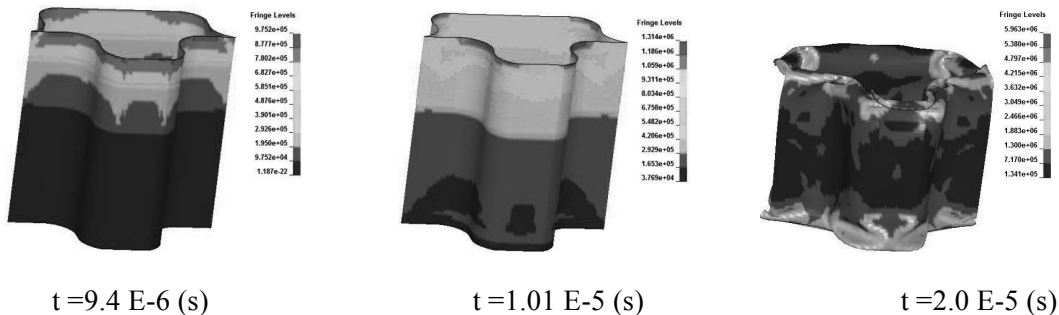
Where : $\Delta\varepsilon_{ij}$ is the strain increment, n is the time increment.

In the fully compacted phase, honeycomb is an elastic-perfectly plastic material, and its stresses S_{ij} updated as follow

$$S_{ij}^{n+1^{trial}} = S_{ij}^n + 2G\Delta\varepsilon_{ij}^{dev^{n+0.5}} \quad (55)$$

where : $\Delta\varepsilon_{ij}^{dev}$ is the deviatoric strain increment, n is the time increment.

When the compressed volume of the cell became 20% of the initial volume the honeycomb behave like an aluminum layer, which is defined the maximum failure strain of 18%.



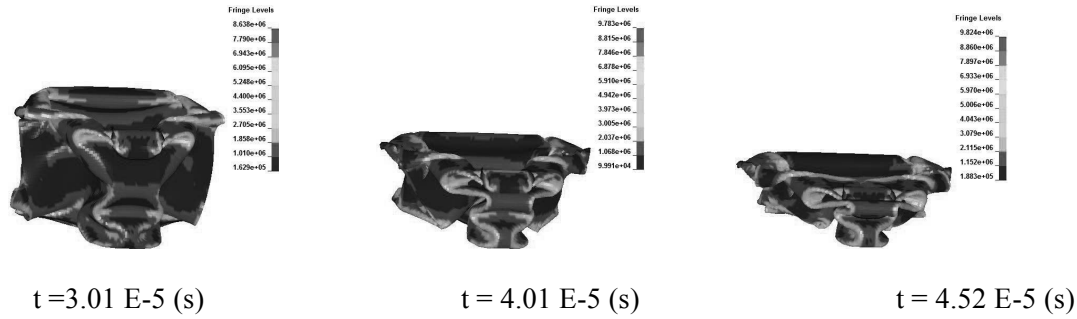


Figure 4.19. Effective stress (Kg/mm.s^2) of a single cell of the flexcore honeycomb F40-0.0019-5052 under dynamic out of plane compression at 129 m/s

Table.4.5. Hexecl 5052 aluminum Flexcore Honeycomb manufacturer's data [87]

Material cell count-gauge	core cell size, c (mm)	core height, l (mm)	core cell wall thickness, t (mm)	ρ (Kg/m^3)	E (GPa)	Crush strength (MPa)	G_{31} , (L) (MPa)	G_{23} , (W) (MPa)
F40-0.0019	7.62	6.35	0.048	49.65	0.861	1.137	220	89.63

II.2.3.3. Aluminum inboard skin: A sheet of Al 2024 T3 alloy with a thickness of 0.3 mm was considered for the inboard skin of the sandwich FML flexcore configuration of the LE bay. It was modeled with 16487 shell elements and was treated as an elasto-plastic material with failure based on a plastic strain. The material model includes strain rate effects. The strain rate is accounted for using the Cowper- Symonds model which scales the yield stress with the factor:

$$\beta = 1 + \left(\frac{\dot{\epsilon}}{D}\right)^{\frac{1}{p}} \quad (56)$$

where D and p are the Cowper-Symonds [Jones 1983] coefficients, are equal to $1.28\text{E}+5 \text{ s}^{-1}$, 4.0, [113] respectively, $\dot{\epsilon}$ is the strain-rate. The mechanical properties used for the inboard skin are reported in the Table.4.6.

Table. 4.6. Mechanical properties of Al 2024 T3 Alloy [85]

ρ (Kg/m^3)	E (GPa)	ν	G (GPa)	σ_y (MPa)	E_t (GPa)	Elongation at break
2780	72.4	0.33	28	290	28	18%

II.3. RESULTS & DISCUSSIONS

II.3.1. Bird Impact on Metallic LE Bay

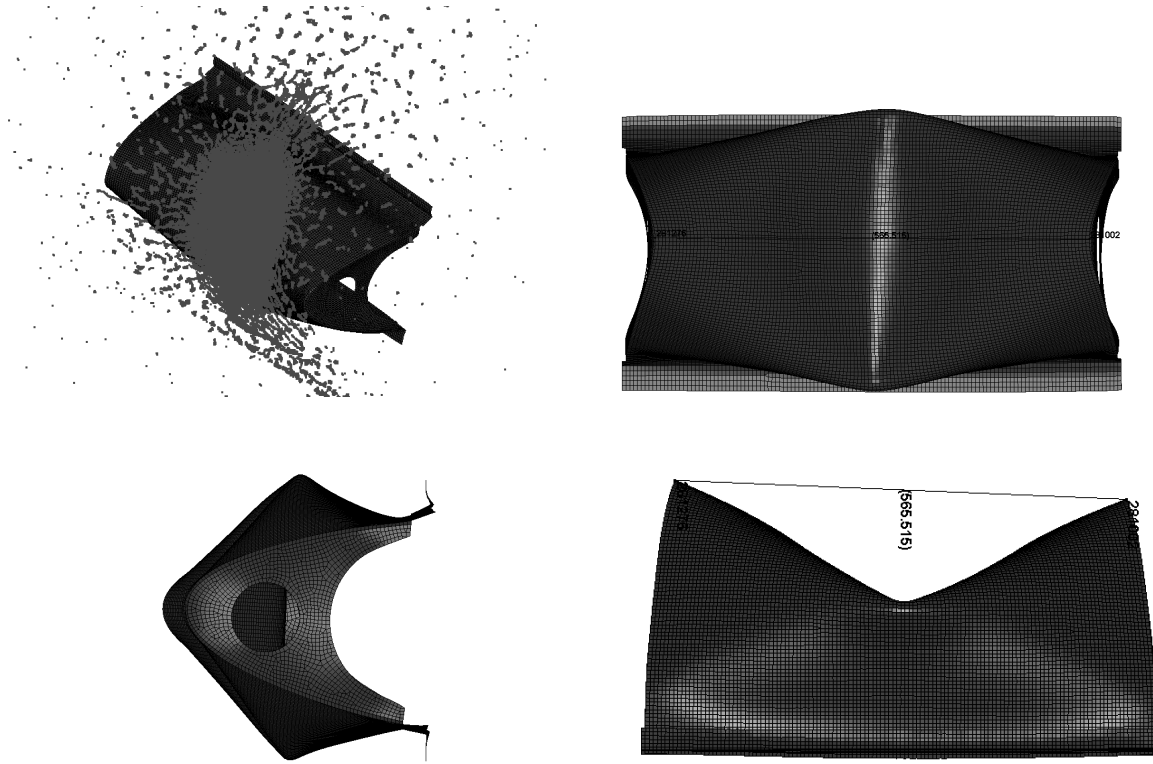


Figure 4.20. 4 lb bird striking onto Al 6013 T6 Alloy LE bay with a velocity of 129 m/s



Figure 4.21. 8 lb bird striking onto Al 6013 T6 Alloy LE bay with a velocity of 129 m/s

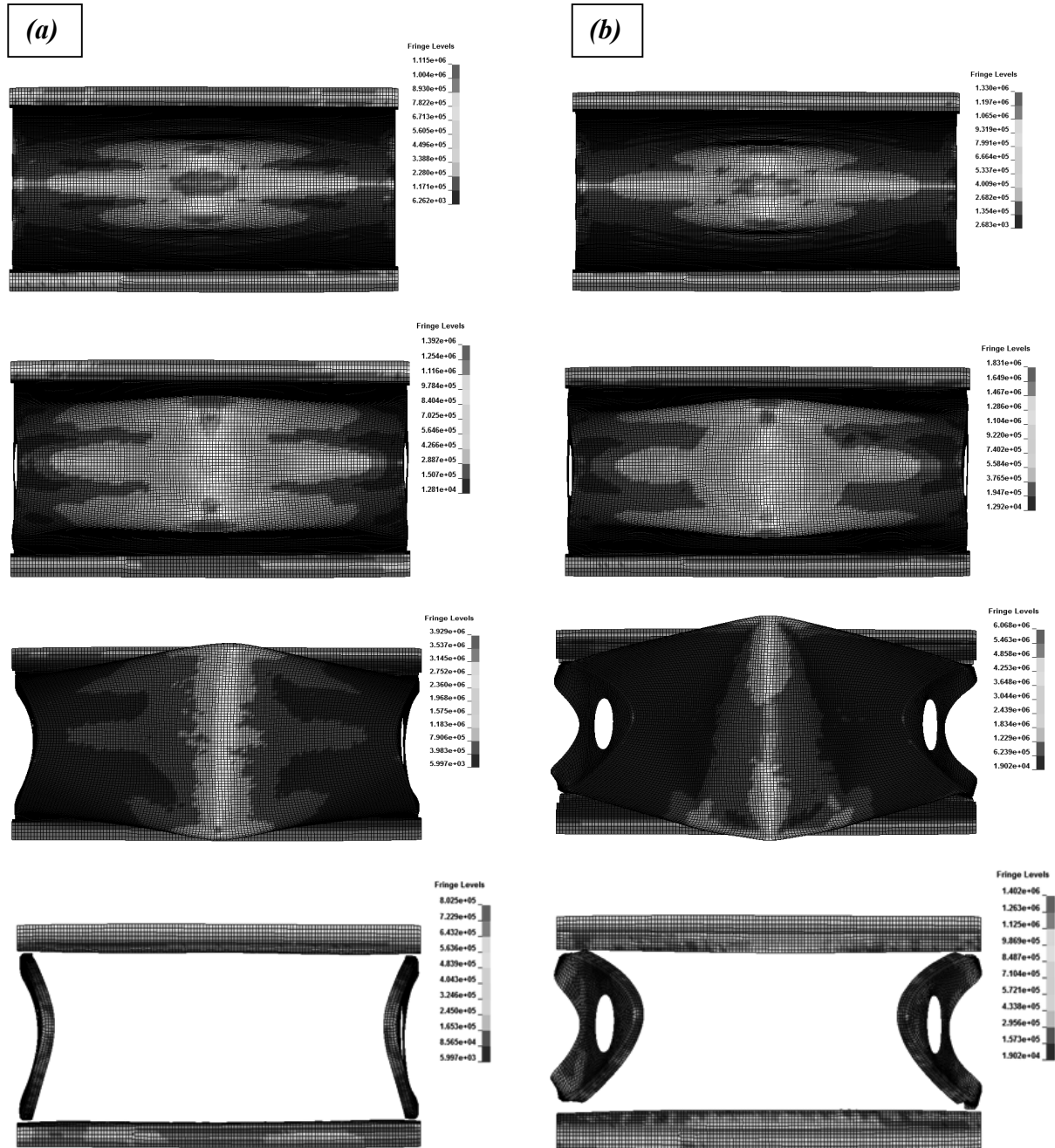


Figure 4.22. V.M stress distribution of, (a) 4lb, (b) 8lb, bird striking onto Al 6013 T6 LE bay with a velocity of $v=129$ m/s

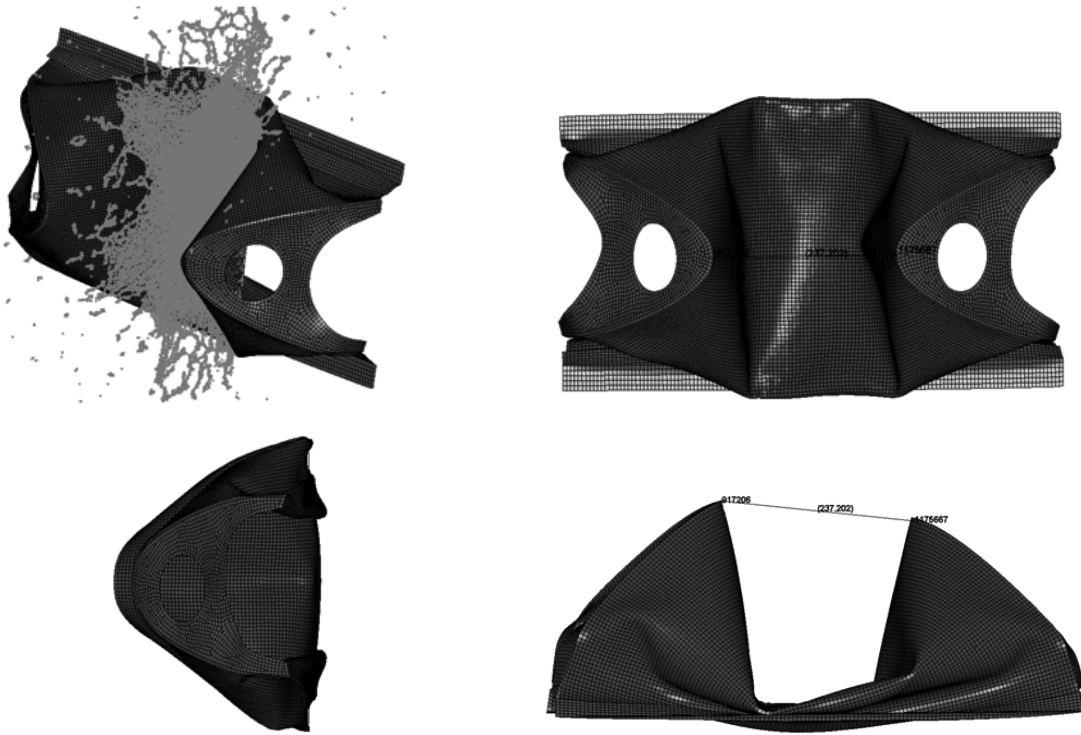
II.3.2. Bird Impact on Composite (FML) LE Bay

Figure 4.23. 4lb bird striking onto composite FML LE with a velocity of 129 m/s



Figure 4.24. 8lb bird striking onto composite FML LE with a velocity of 129 m/s

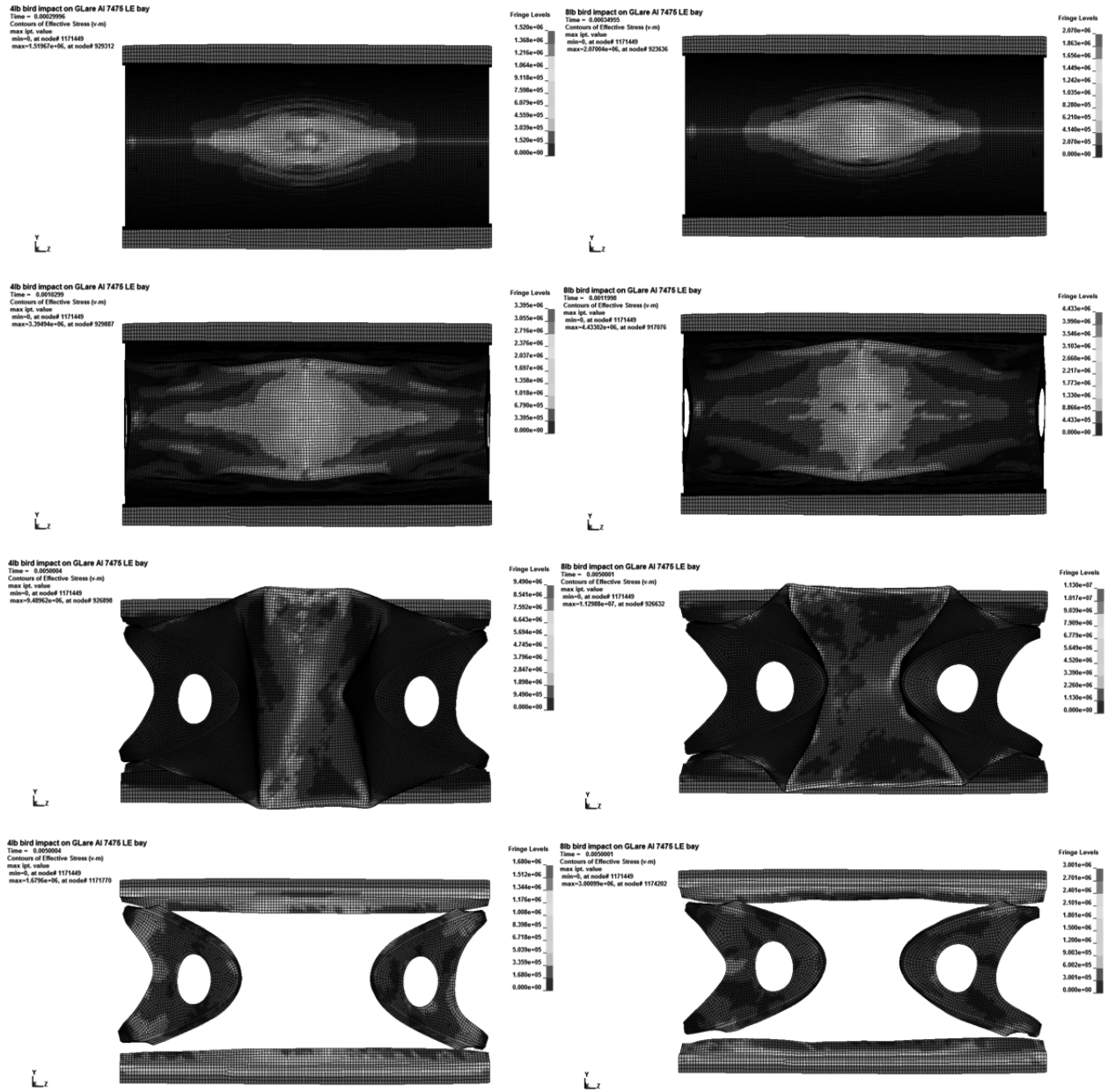


Figure 4.25. V.M stress distribution of, (a) 4lb, (b) 8lb, bird striking onto FML LE bay with a velocity of $v=129$ m/s

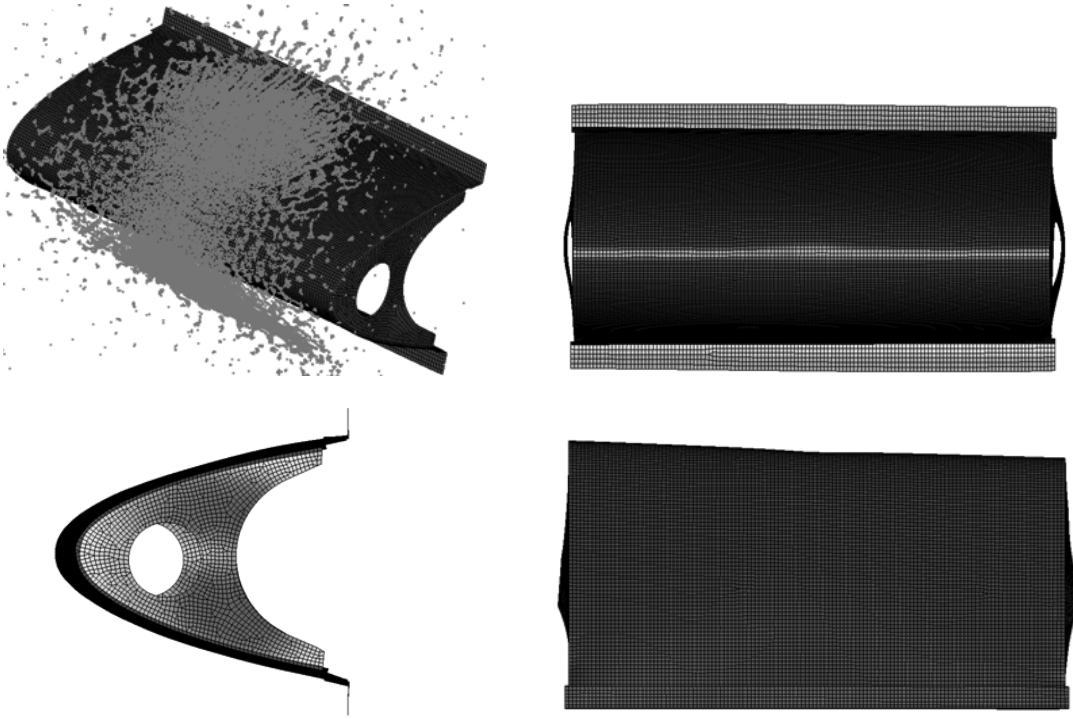
II.3.3. Bird Impact on Sandwich FML LE Bay

Figure 4.26. 4 lb bird striking onto sandwich FML LE bay with a velocity of 129 m/s

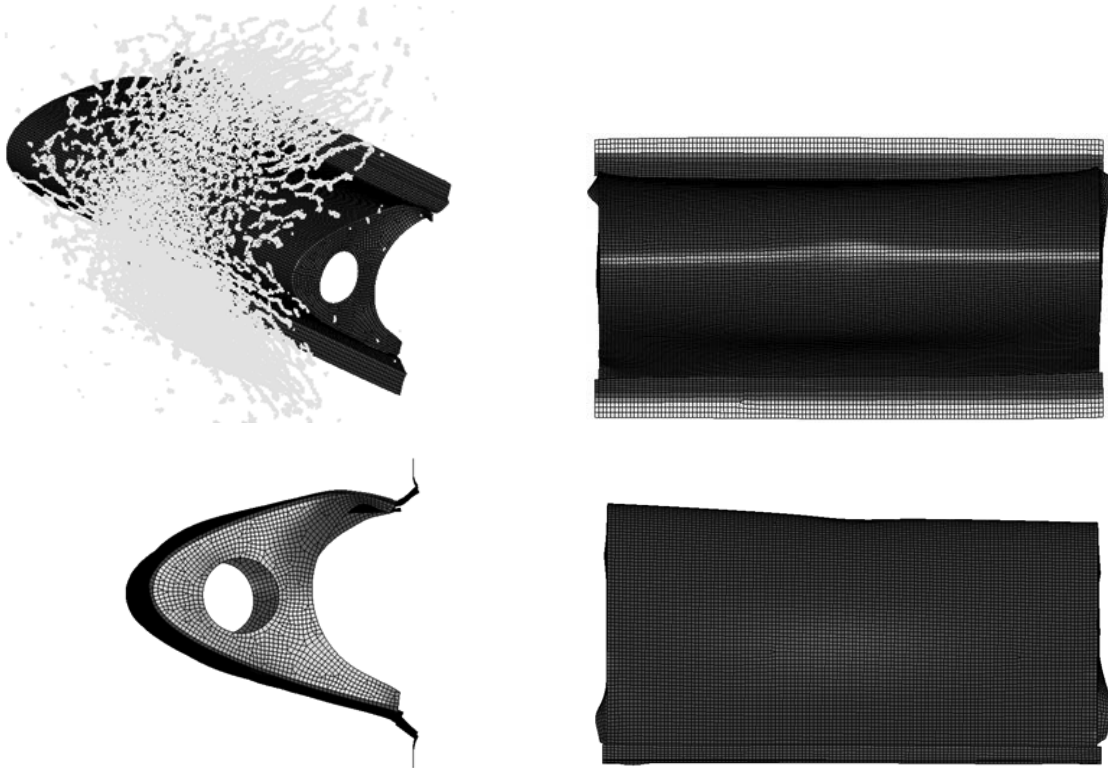


Figure 4.27. 8 lb bird striking onto sandwich FML LE bay with a velocity of 129 m/s

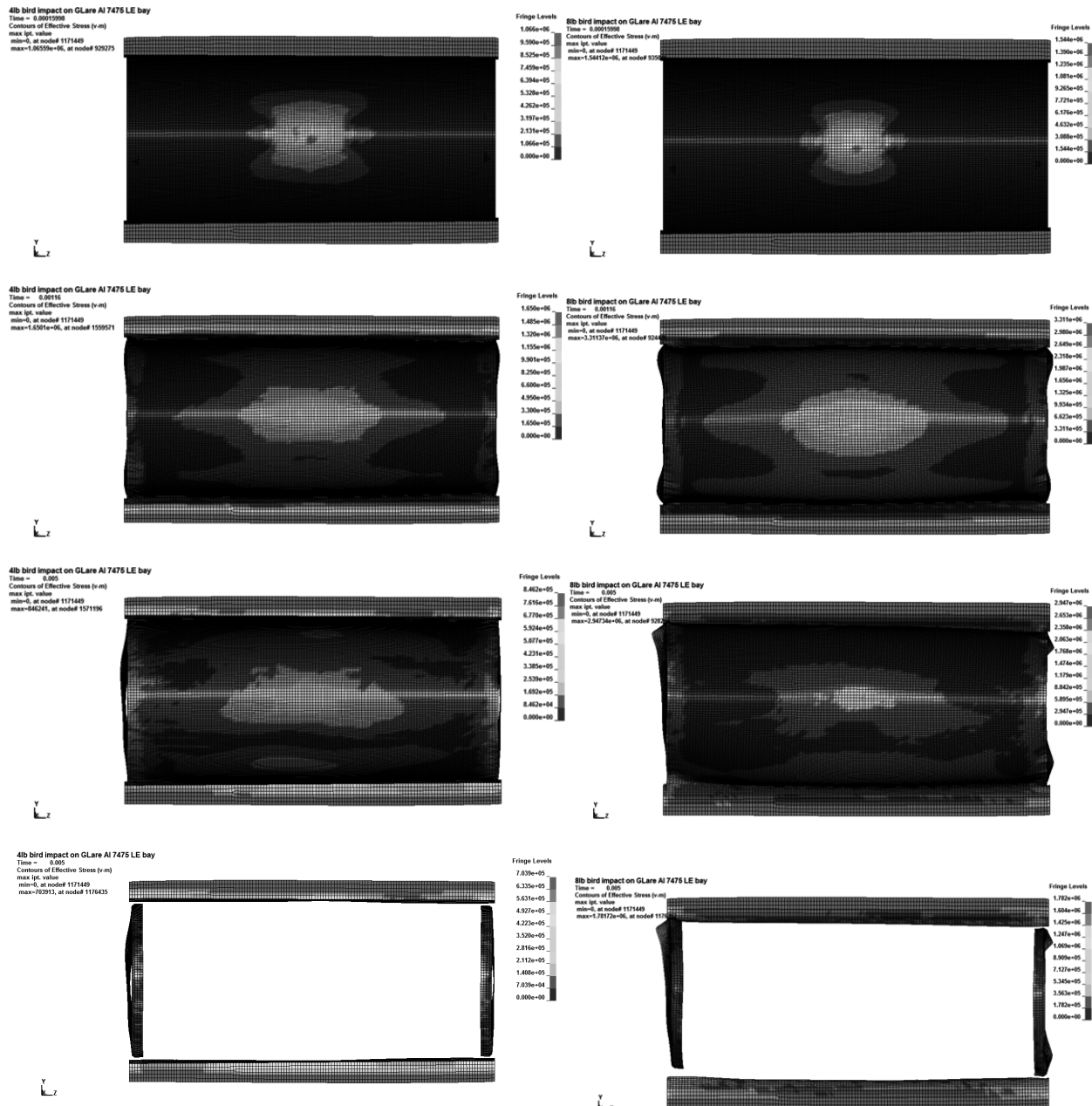


Figure 4.28. V.M stress distribution of, (a) 4lb, (b) 8lb, bird striking onto sandwich FML LE bay with a velocity of $v=129$ m/s

A deformation until the mid depth at the back spar was occurred for the impact of 4lb bird at velocity of 129 m/s on the aluminum, Al 6013 T6, configuration, that has not affected the back spar of the leading edge bay and no perforation was registered. The distance between the ribs at the end of impact was measured equal to 555.51 mm, Figure 4.20, shows the leading edge bay after impact in different views.

A total deformation of the skin was occurred in the impact of 8lb bird at velocity of 129 m/s on the aluminum configuration, that has not affected the back spar and no perforation was registered. The distance between the ribs at the last phase of impact was measured equal to 413.86 mm, Figure 4.21, shows the leading edge bay after impact in different views.

Figure 4.23, presents the final shape obtained from the simulation of the composite FML leading edge bay after been impacted by 4lb bird at velocity of 129 m/s, where a total deformation of the skin has affected the back spar without any perforation of the skin, the distance between the ribs at the last phase of impact was measured equal to 237.20 mm. (this test has been already validated with experimental test, Chapter 3).

As is shown in Figure 4.24, a total deformation of the skin of the composite FML leading edge bay was obtained from the simulation of 8lb bird impact at velocity of 129 m/s that affected the back spar and passed through it. A distance of 138.82 mm was measured between the edges of the ribs after impact.

The numerical simulation of 4lb bird impact onto the sandwich FML flexcore leading edge bay at a velocity of 129 m/s, shows a good behavior of this configuration and an excellent resistance to this impact with no remarkable deformation of the skin, except, the ribs buckling, see Figure 4.26.

The Figure 4.27, shows the final shape of the leading edge bay after impact in different views, where no significant deformation has occurred in the skin but an important buckling was occurred to the ribs.

In Figures, 4.22, 4.25, 4.28, the stress distribution during the impact on the three configurations of the leading edge bay for both birds weight, 4lb and 8lb bird, is shown, where

the maximum stress was captured at the center of impact, ribs detachment with relevant residual stress was captured in the ribs after bird diverting for all impacts configurations.

Those tests have been useful to identify the best material configuration capable to withstand the bird's loads.

Because of the ribs buckling occurred on the small scale of the leading edge during bird impact tests (section II), a ribless configuration of a real aircraft leading edge was considered in the following sections for bird strike's tests and certification by analysis.

III. BIRD IMPACT ONTO REAL AIRCRAFT RIBLESS SANDWICH FML LEADING EDGE STRUCTURE

The presence of ribs in a leading edge could increase the weight of the structure and could create a difficulty in assembling especially in case of a sandwich leading edge configuration because of the honeycomb presence. In addition, checking for the LE impact damage would only be necessary for bird perforation and for the spar integrity deformation. Having these advantages, a ribless leading edge configuration is considered.

Because of its satisfaction in the last bird impact tests and because of the affection of the ribs, the sandwich FML lay-up of the leading edge bay was reproduced on a real aircraft ribless leading edge.

C27J aircraft leading edge structure (Figure 4.29) was analyzed to the impact of 4 lb and 8 lb birds with a velocity of, 129 m/s that presents the cruise speed of the aircraft.



Figure 4.29. Alenia C27 J Spatran aircraft

The C27J aircraft leading edge structure presents a length of 2970 mm, with a cord that varies between 450 mm and 750 mm and a sweepback angle of 63°. It consists of two main parts:

(i) a spar made of aluminum 2024-T3 alloy 0.8 mm thick and (ii) a sandwich FML-Flexcore lay-up of 8.05 mm thick. Figure.4.30 shows the typical dimensions of this leading edge.

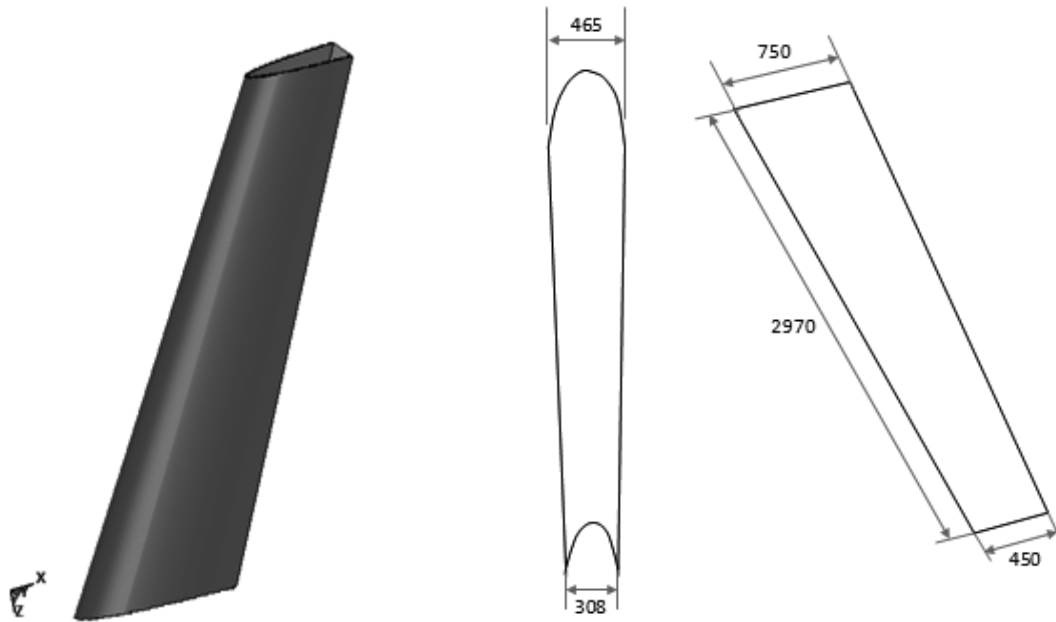


Figure. 4.30. Ribless leading edge

III.1. Finite Element Model of the C27J Aircraft Leading Edge

Based on simulation results which have been obtained previously on the small sample of the leading edge, section II.2.3, the same modeling technique, material models etc. were transferred to model the ribless sandwich FML leading edge. The constraints used were typical of a connection of a leading edge to the spar. The point of impact was chosen as the most critical, because of the presence of a compartment at the back of the leading edge, which could have consequences on the controls of the aircraft after the damage.

The outboard ply of the ribless leading edge was modeled with 72,000 shell elements, the honeycomb was modeled with 144,000 eight-node solid elements, and the inboard ply was modeled with 72,000 shell elements. The spar was modeled with 11,200 shell elements. Figure 4.31, shows the Finite element model of the ribless leading edge.

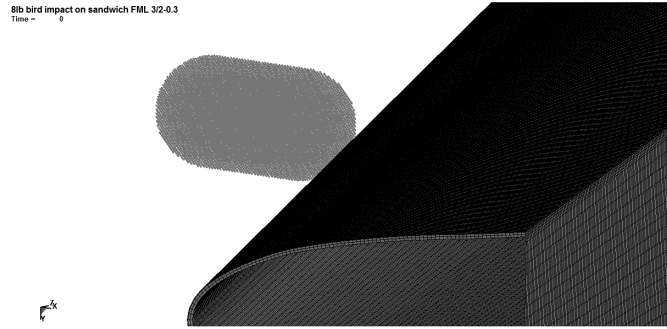


Figure 4.31. FE view of the ribless leading edge

III.2. Results & Discussions

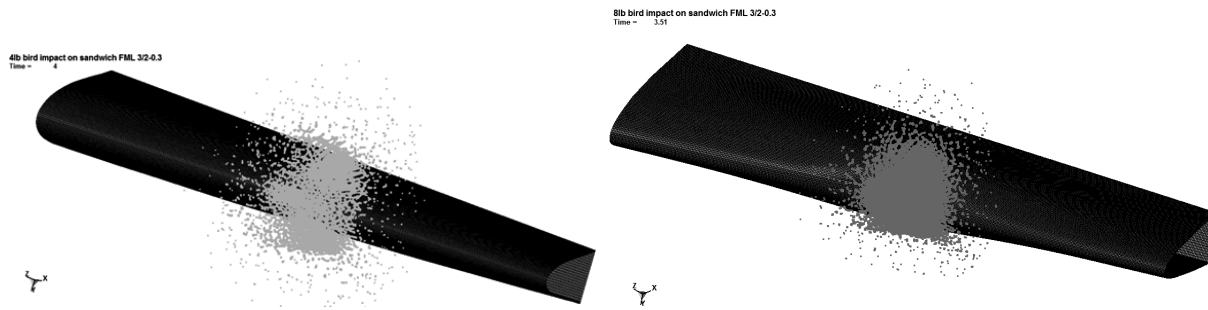
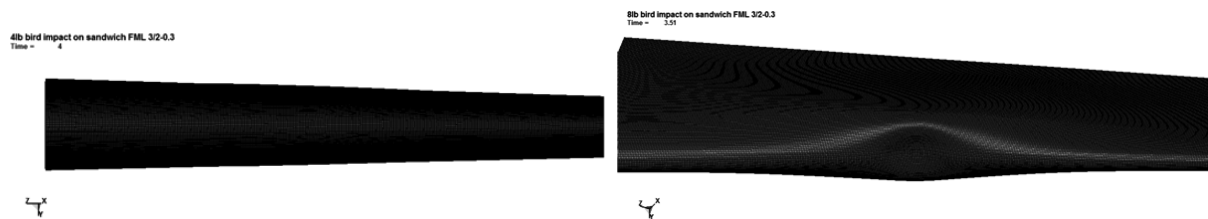


Figure 4.32. 4 lb bird and 8 lb bird impact onto ribless sandwich FML LE at 129 m/s



Figure 4.33. 3D views of the ribless sandwich FML LE after 4 lb and 8 lb bird impacts at 129 m/s





[82]

Figure 4.34. Front views of the ribless sandwich FML LE after 4 lb and 8 lb bird impacts at 129 m/s (the 8lb bird impact test on the S.FML. LE has been already validated in Chapter 3)

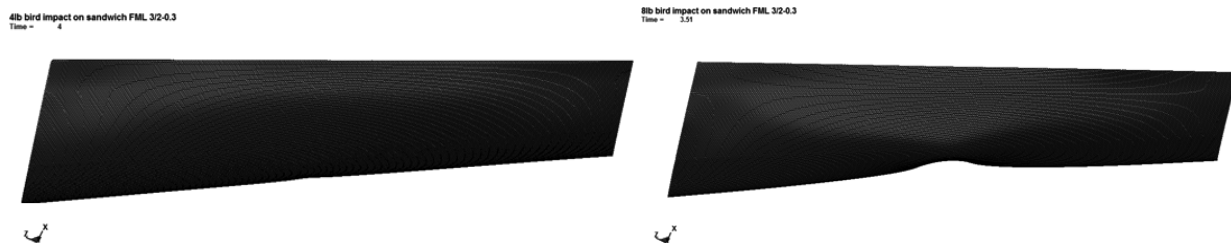


Figure 4.35. Up views of the ribless sandwich FML LE after 4 lb and 8 lb bird impacts at 129 m/s

Figure 4.32, presents the last step of the simulation of the impact of 4 lb and 8 lb birds at 129 m/s onto the C27J aircraft ribless leading edge. The Figure 4.33 presents the three dimension view of the final shape of this ribless leading edge for each impact simulation. Figure 4.34, shows the front views of the final shape of the ribless leading edge after each impact and Figure 4.35, presents the upper views. These figures show:

- 1- The excellent behavior of the sandwich FML flexcore configuration of the ribless leading edge to the impact of 4lb bird at 129 m/s where no remarkable deformation has occurred to the lay-up;
- 2- The good resistance of the sandwich FML flexcore configuration of the ribless leading edge to the impact of 8 lb bird at 129 m/s where a permanent localized deformation has occurred to the lay-up and the skin did not suffer any perforation. This structure was able to absorb the 8 lb bird impact energy at 129 m/s without any major failure. Note that the numerical results concerning the 8 lb bird impact was already validated with the experimental results obtained by Guida [82] for the same test (Chapter 3, section 6.4).

IV. BIRD IMPACT ONTO INNOVATIVE MATERIAL CONFIGURATIONS OF AN AIRCRAFT RIBLESS LEADING EDGE

The objective of this section is to simulate by the help of finite element analysis bird impact onto a real aircraft ribless leading edge made with innovative materials that should satisfy the airworthiness requirements. The leading edge shouldn't be perforated and in case of high deformations no critical damage must be induced to the front spar after impact. Structural response of different innovative configurations of a ribless leading edge structure subjected to bird impact was evaluated and certified numerically.

Three different lay-up configurations with various thicknesses were taken into account in this work: a sandwich metallic with single core (configuration n°1), a sandwich metallic with double core (configuration n°2) and a sandwich Glare with double core (configuration n°3). Six numerical impact tests were performed with birds with a nominal weight of 4 lb and 8 lb.

IV.1. The Sandwich Metallic Configuration With Single Core; had an outboard ply in aluminum 2024 T3 with a thickness of 0.5 mm, a core made of Aluminum 5052 honeycomb flexcore, F40- 0.0019, with a cell height of 6.35 mm, and an inboard ply made of aluminum alloy 2024 T3 alloy with a thickness of 0.3 mm, giving a total configuration thickness of 7.15 mm.

IV.2. The Sandwich Metallic Configuration With Double Core, consists of two cores made of Al 5052 honeycomb flexcore, F40- 0.0019, with a cell height of 6.35 mm for each core, separated by a ply in aluminum 2024 T3 alloy with a thickness of 0.3, an outboard and an inboard ply in aluminum 2024 T3 alloy, with a thickness of 0.4 mm and 0.3 mm, respectively. The total thickness of the configuration is 13.7 mm.

IV.3. The Sandwich Glare Configuration With Double Core, consists of the same parts as the sandwich metallic configuration with double core described above, except, the outboard skin which is made with a ply of Glare 3-1/2-0.4 mm with a stacking sequence as: [Al/G0°/G90°] where Al referred to a layer of aluminum alloy 2024-T3 with a thickness of 0.4 mm and G0° and G90° are the glass/epoxy layer orientations, FM 94-27%- S2- Glass- 187- 460; each glass layer had a thickness of 0.125 mm, giving a total thickness of the Glare lay-up of 0.65 mm and a total thickness of the configuration of 13.95 mm.

Table 4.7, summarizes materials and thicknesses which have been considered for the three different ribless leading edge configurations.

Table 4.7. Different innovative configurations of the ribless leading edge

<i>LE configuration</i>	<i>materials</i>	<i>Total thickness</i>
<i>Configuration n°1</i>	<i>Al 2024 T3 Alloy 0.5mm+ flexcore 6.35mm+ Al 2024 T3 Alloy 0.3mm</i>	<i>7.15 mm</i>
<i>Configuration n°2</i>	<i>Al 2024 T3 Alloy 0.4 mm + flexcore 6.35mm+ Al 2024 T3 Alloy 0.3mm+ flexcore 6.35mm+ Al 2024 T3 Alloy 0.3mm</i>	<i>13.7 mm</i>
<i>Configuration n°3</i>	<i>Glare 3 0.65mm+ flexcore 6.35mm+ Al 2024 T3 Alloy 0.3mm+ flexcore 6.35mm+ Al 2024 T3 Alloy 0.3mm</i>	<i>13.95 m</i>

IV.4. Results & Discussions

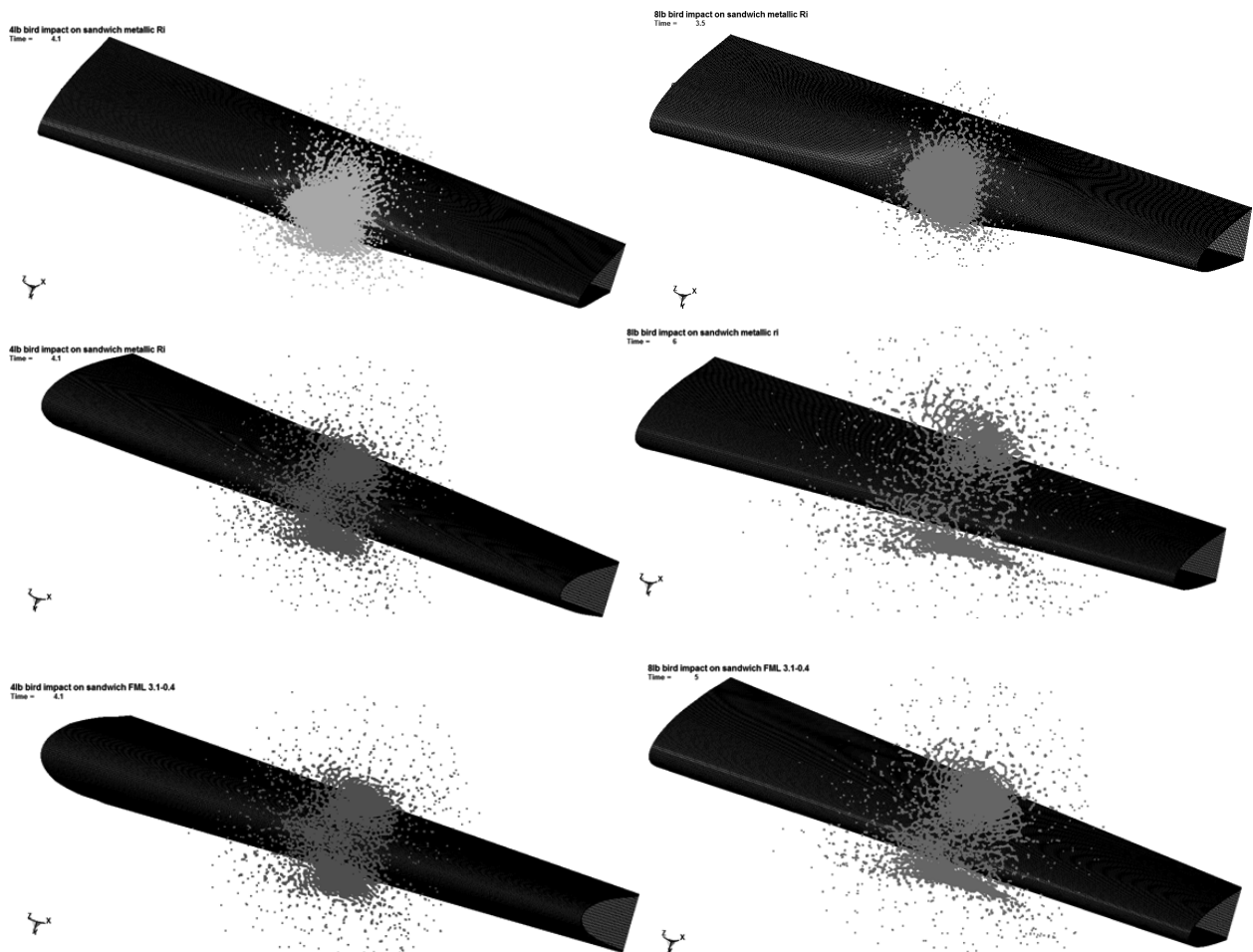


Figure 4.36. 4 lb bird and 8 lb bird impact onto the three different configuration of the ribless LE at 129 m/s

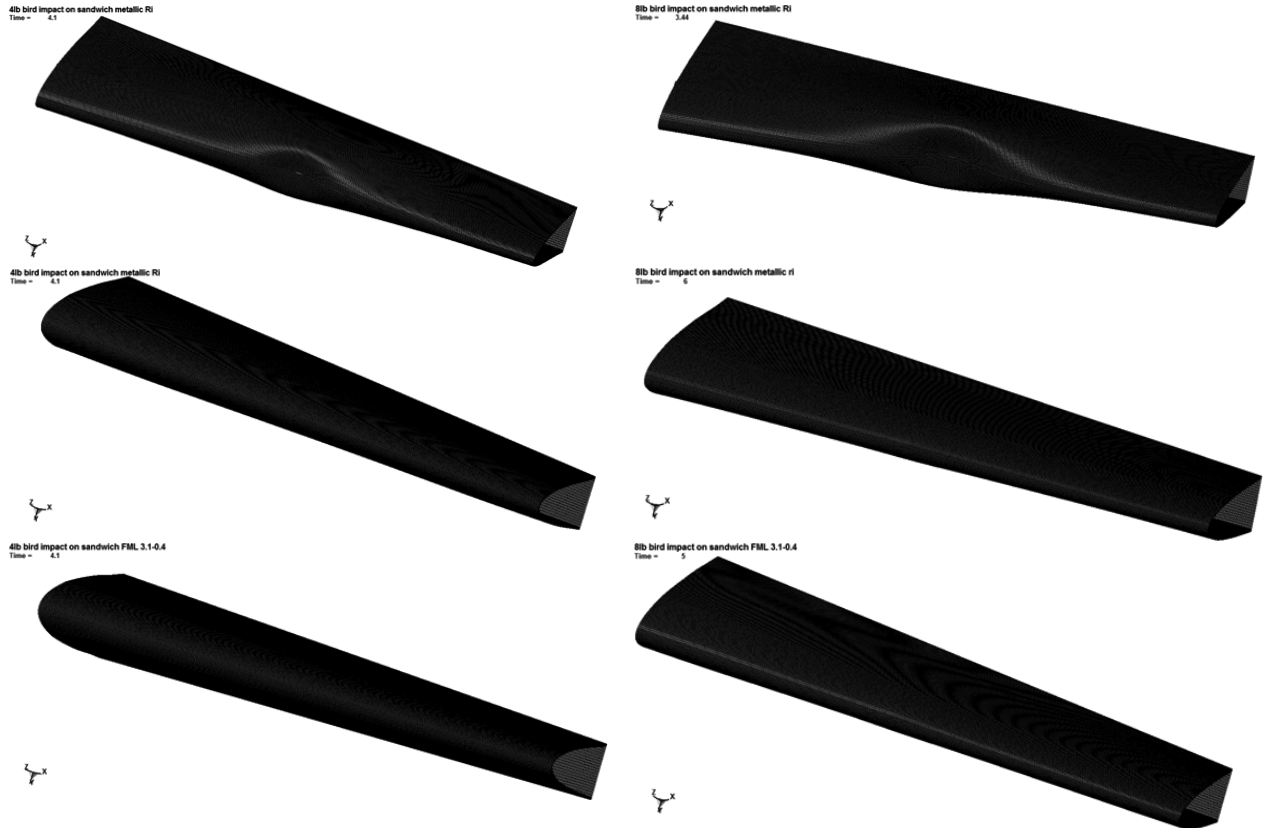
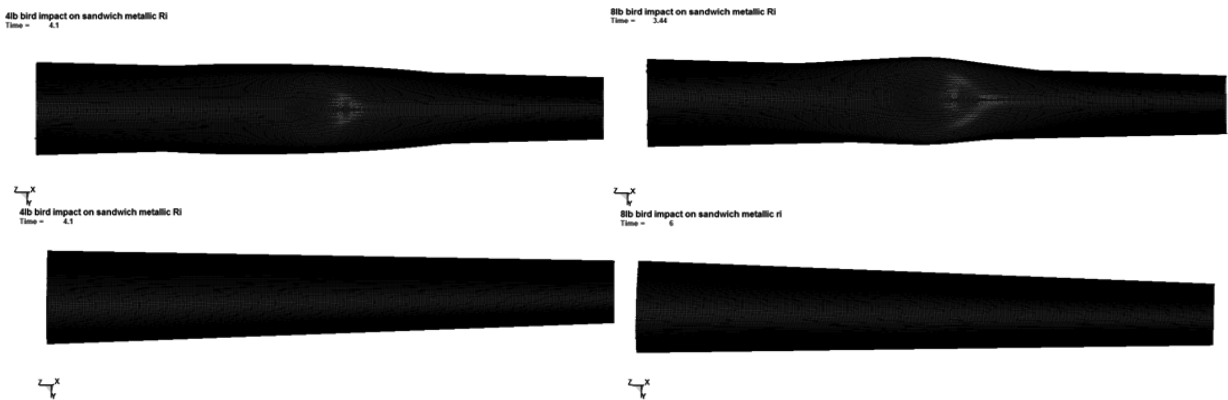


Figure. 4.37. 3D view of three configurations of the ribless LE after 4 lb and 8 lb bird impacts at 129 m/s



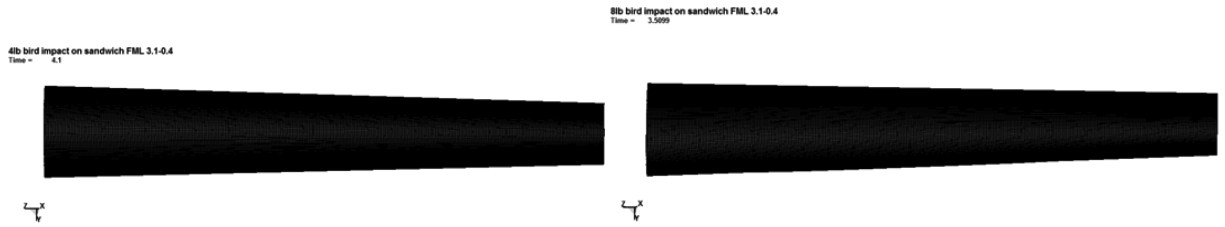


Figure. 4.38. Front view of three configurations of the ribless LE after 4 lb and 8 lb bird impacts at 129 m/s

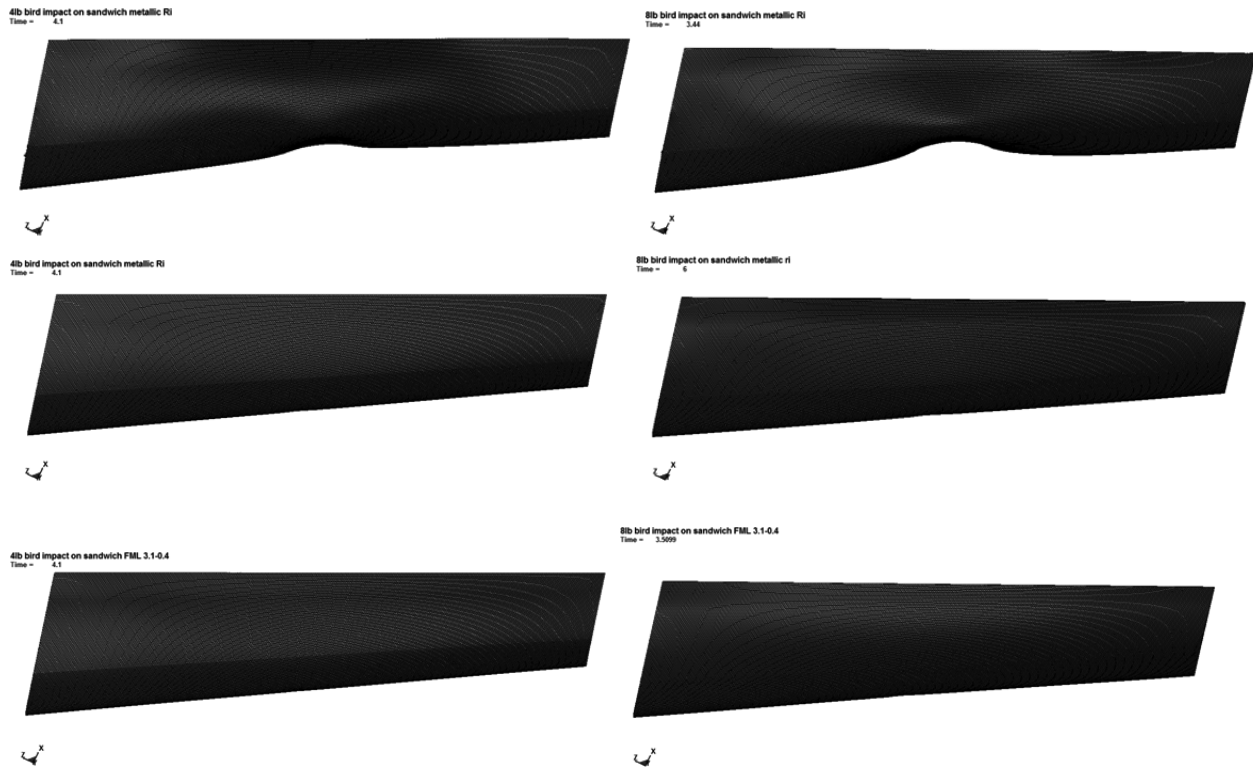


Figure. 4.39. Up view of three configurations of the ribless LE after 4 lb and 8 lb bird impacts at 129 m/s

Impact behavior of the ribless sandwich leading edge under impact of 4 lb and 8 lb birds at 129 m/s was numerically investigated for each configuration as illustrated in the figures above. The structural response was predicted for each configuration in terms of the deformation induced on the ribless leading edge lay-up. Figure 4.36, presents the last step of the impact simulation of 4 lb and 8 lb birds at 129 m/s onto the leading edge's, configuration n°1, configuration n°2, and configuration n°3, respectively. The Figure 4.37 presents the three dimension view of the final shape of these ribless leading edges after each impact simulation. Figure 4.38 shows the front

views and Figure 4.39 presents the upper views of the final shape of these ribless leading edges after each impact.

- In both scenarios of 4 lb and 8 lb bird impact onto the sandwich aluminum with single core “configuration n°1” the lay-up deforms during the collision with bird. This configuration has shown a good behavior and good resistance to the impact of 4lb bird at 129 m/s where no perforation was seen in the skin and a significant deformation has occurred to the lay-up without affecting the rear spar and. The leading edge was able to absorb the 4 lb bird impact energy at 129 m/s without any major failure. Same results were obtained for the impact of 8 lb bird at 129 m/s expecting the amount of deformation occurred to the lay-up which depends on the bird kinetic energy. This ribless sandwich aluminum configuration is an alleviated configuration of the ribless sandwich FML leading edge configuration certified by Guida 2013 and would allowed a considerable reduction in weight and manufacturing costs comparing to that certified by Guida 2013.
- Both structural materials of “configuration n°2” and “configuration n°3” exhibit excellent resistance performance under the impact of 4 lb and 8 lb birds at 129 m/s without any visible deformation in the leading edge lay-up. They behave like rigid structures under impact. Thus, these structures can guarantee their potential application in the aircraft industry.

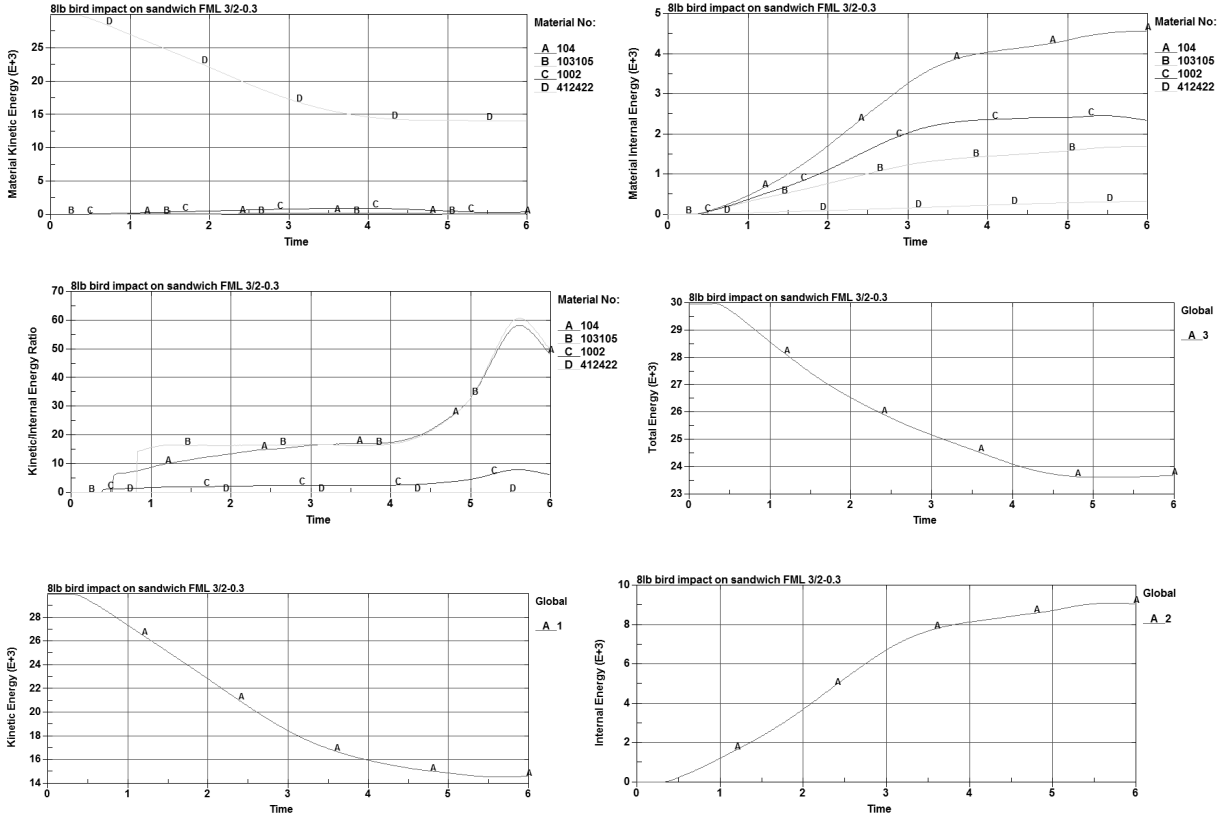
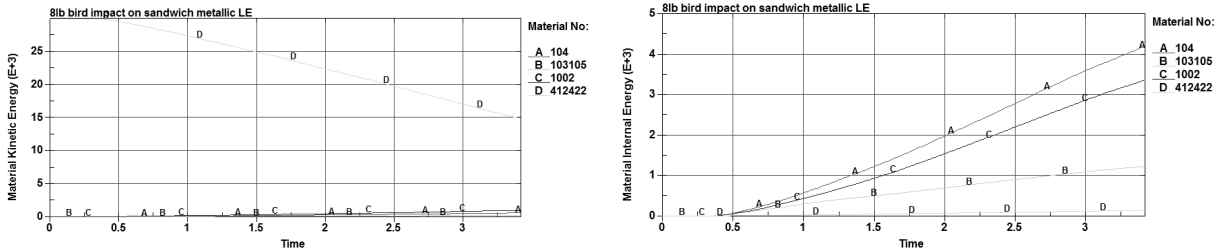


Figure 4.40. Plot of the different energies for the 8 lb impact at 129 m/s on the S- FML-LE



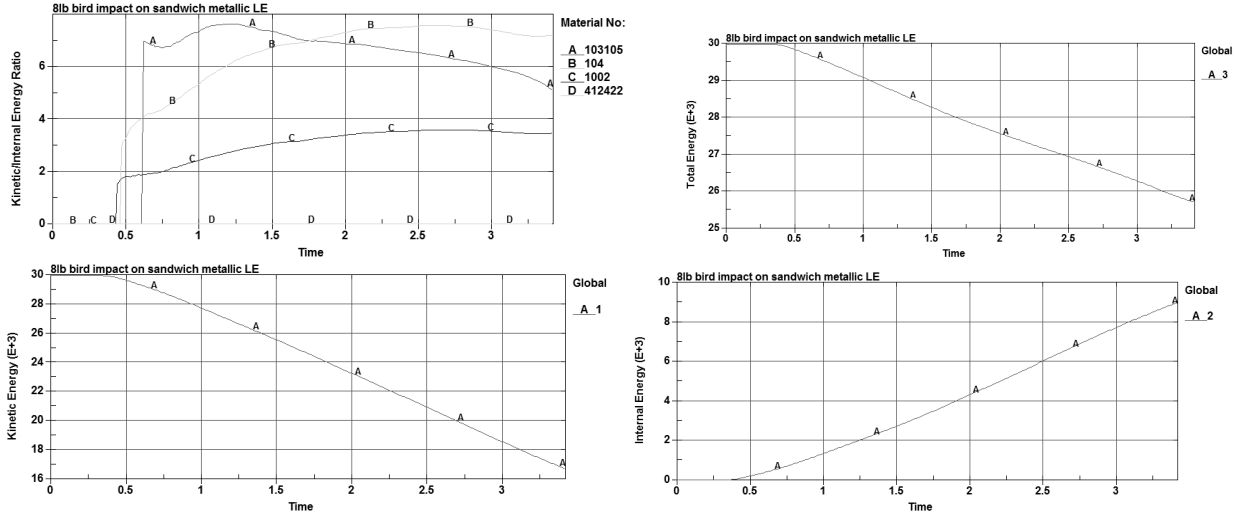


Figure 4.41. Plot of the different energies for the 8 lb impact at 129 m/s on the S-MTL-1C- LE

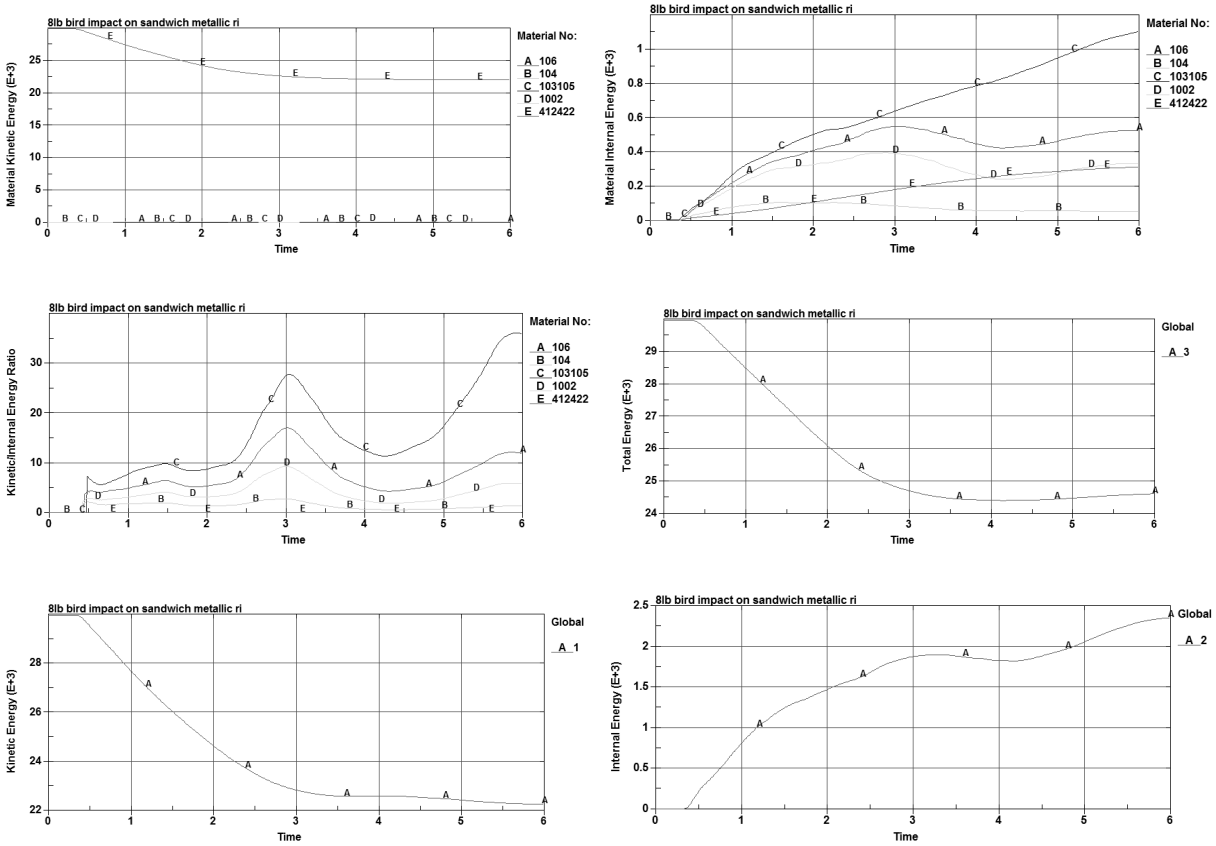


Figure 4.42. Plot of the different energies for the 8 lb impact at 129 m/s on the S- MTL-2C-LE

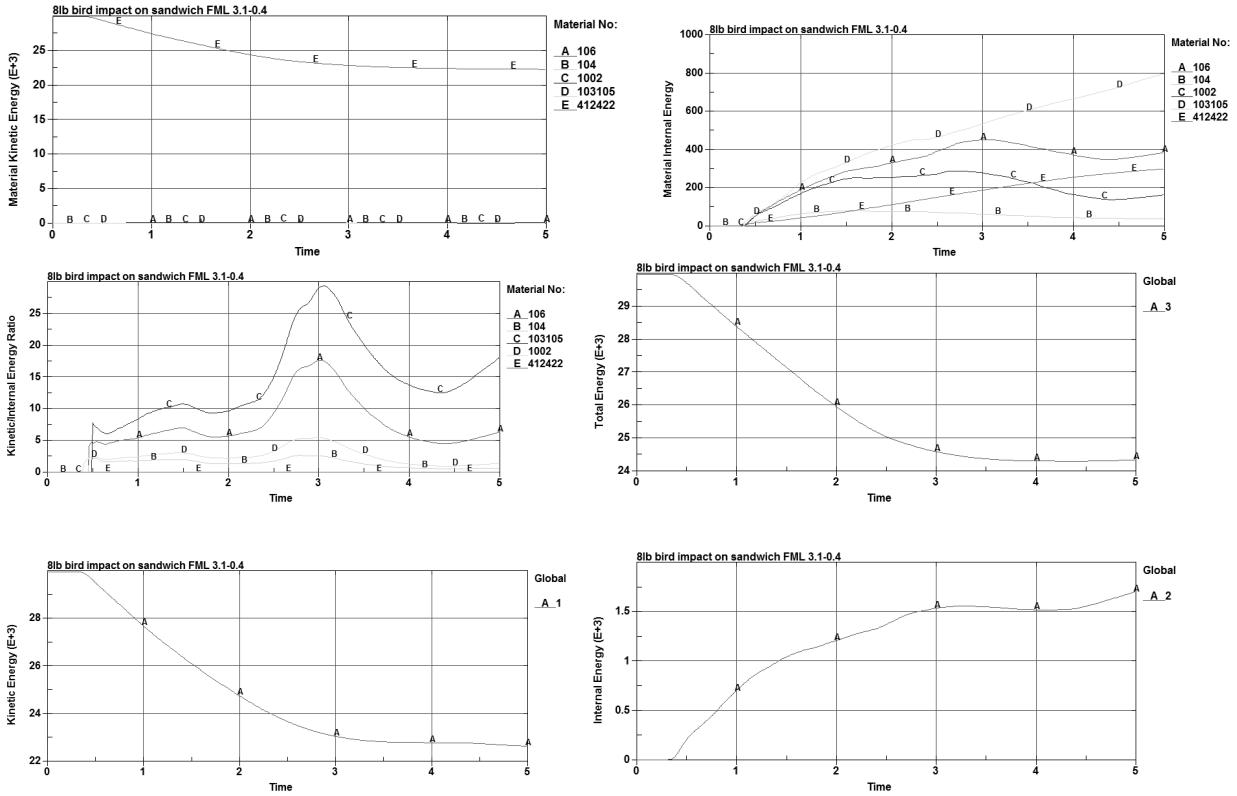


Figure 4.43. Plot of the different energies for the 8 lb impact at 129 m/s on the S- GLR- 2C-LE

Figures 4.36- 4.39 illustrate the plot of energies obtained from simulation of 8 lb bird impact at 129 m/s onto, single core sandwich FML, single core sandwich metallic, double core sandwich metallic and double core sandwich Glare, ribless leading edge, respectively.

The shock absorbing of the leading edge structure (Lay-up and spar- CNRB) depends on the amount of energy transferred-in due to bird impact. Before the bird/ LE collision, the total energy of the system is the bird kinetic energy which is equal the half the bird mass and the square of its velocity and is accounted to be equal to 29.95 Joules for the impact of 8lb bird at 129 m/s. this energy will decay just after collision because of the decay in the impact velocity and will not be entirely transferred to the leading edge structure. At the collision moment, some of this energy will lost and dissipated as heat energy in bird because of the occurrence of shock compression that results high pressure gradient and a very slight temperature rise into the bird and SPH bird particles speed up and they gain kinetic energy, where an internal energy developed into the bird in parallel with the decay of its kinetic energy (see figures above). The other part of the kinetic energy is received by the leading edge by the work done by the bird impact force. The material

elements of the leading edge skin started to deform and the nodes moved which generated internal forces into the leading edge materials. This work is not only done by the external impact force but also by the internal forces. The received bird kinetic energy is transferred into internal energy and distributed with different amounts into the different members of leading edge (see figures above). During material deformation, an amount of the internal energy is dissipated through heat and conducted away through the materials. Thus, a plastic deformation remains in the leading edge skin because of the non conservation of energy (dissipative internal forces), which is the case of the sandwich FML and the Sandwich metallic with single core leading edges, Figure 4.40 and 4.41. The work done in this case depends on the path taken and would be calculated by evaluating an integral.

For the case of the sandwich metallic with double core and sandwich Glare with double core leading edges, because of the strong resistance of these materials to impact, just few amount of the kinetic energy is transferred to the leading edge material and converted into internal energy. In the figures above, the slight loss in the total energy of the system is due to the energy dissipated by the hourglass forces reacting against the formation of the hourglass mode in elements and is tracked and reported in the output files of the simulation (MATSUM and GLSTAT).

CONCLUSIONS

V. CONCLUSIONS

In the presented work, the fundamental hydrodynamic theory was used to analyze the behavior of birds during impact. The detailed study of the bird impact process has led to well, understanding the phenomena, developing the equations of state describing the most important phases in the process and defining the pressures characterizing each phase. The selected EOS for water with 10% of air porosity was appropriate for the bird approximation. The validation of the developed SPH cylinder, of the porous water (10% air) impacting a rigid plate, with the theoretical results confirms the validity and robustness of the approach for a complete modeling of bird impact process.

The present numerical simulation also revealed that the length-to-diameter aspect ratio of the bird striking onto a rigid plate has little influence on the results, especially the impact peak pressure, and the bird geometry that more than others fits to a birdstrike test is the hemispherical ended shape with $L/D=2$, so the bird with the cylindrical shape doesn't have the desired effect for this application.

The validation of the developed hemispherical SPH model, with a double length in respect to diameter, for the impact of 4 lb and 8 lb bird on a rigid flat plate, with the experimental test results obtained by Challita in 1979 and with the experimental tests results obtained by Guida in 2009 & 2013 on a leading edge bay and a ribless aircraft leading edge, allowed their recognition as a valid and robust bird impact models and assures their effectiveness of its application on new designed aircraft leading edge structure. These numerical models allowed estimating the pressure and the impact force during the event.

The new designed sandwich ribless leading edge structures were able to withstand the 4 and 8 lb bird impacts at a velocity of 129 m/s. The results have been obtained with the help of finite element analysis using LS-DYNA. The FE models were able to predict the final deformed shape of the ribless leading edge structure with the absence of bird penetration and significant deformation, showing that the designed configurations were able to protect the inner structures of the LE from damage thus satisfying the certification requirements.

The obtained numerical results are very helpful for the design and certification of ribless aircraft leading edge structures because they allow good probability estimation for successful tests.

This method paves the way for advanced validations towards achieving the certification with the least possible number of iterations.

REFERENCES

- [1] European Organization for the Safety of Air Navigation. Bird Strike. 2019. Available online: http://www.skybrary.aero/index.php/Bird_Strike (accessed on 12 February 2020).
- [2] Avisure. Fatalities and Destroyed Aircraft in Aviation. 2019. Available online: <https://avisure.com/aboutus/fatalities-and-destroyed-aircraft-due-to-wildlife-strikes-1912-to-present/> (accessed on 30 January 2020).
- [3] Aviation Safety Network: <https://aviation-safety.net/database/record.php?id=19621123-1>
- [4] Dolbeer RA. Birds and aircraft – fighting for airspace in ever more crowded skies. *Human–Wildlife Conflicts* 2009;3(2):165–6.
- [5] Herald, A. Accident: Ural A321 at Moscow on Aug 15th 2019, Bird Strike into Both Engines Forces Landing in Corn Field. 2019. Available online: <http://avherald.com/h?article=4cb94927&opt=0> (accessed on 4 February 2020).
- [6] ICAO. Airworthiness of Aircraft, 11th ed.; Annex 8 to the Convention on International Civil Aviation; ICAO: Montreal, QC, Canada, 2010.
- [7] European Aviation Safety Agency. Certification Specifications for Normal Aeroplanes; Ammendment 5; European Aviation Safety Agency: Cologne, Germany, 2017.
- [8] Federal Aviation Administration. 14 CFR Part 25—Airworthiness Standards: Normal Category Airplanes; Federal Aviation Administration: Washington, DC, USA, 2011.
- [9] European Aviation Safety Agency. Certification Specifications and Acceptable Means of Compliance for Large Aeroplanes CS-25; Amendment 23; European Aviation Safety Agency: Cologne, Germany, 2019.
- [10] European Aviation Safety Agency. Definitions and Abbreviations Used in Certification Specifications for Products, Parts and Appliances; European Aviation Safety Agency: Cologne, Germany, 2007.
- [11] Federal Aviation Administration. Transport Airplanes. Available online: https://www.faa.gov/aircraft/air_cert/design_approvals/transport/ (accessed on 30 September 2019).
- [12] European Aviation Safety Agency. Certification Specifications for Engines; Amendment 3; European Aviation Safety Agency: Cologne, Germany, 2010.
- [13] Federal Aviation Administration. 14 CFR 33.76—Bird Ingestion; Federal Aviation Administration: Washington, DC, USA, 2011; Volume 1.
- [14] Monaghan, J. J., “Particle Methods for Hydrodynamics”, *Computer Physics Reports*, October 1985, Vol. 3, Issue 2, pp71-124.
- [15] Monaghan, J. J., “An Introduction to SPH”, *Computer Physics Communications*, 1988, Vol. 48, pp89-96.
- [16] Monaghan, J. J., “Smoothed Particle Hydrodynamics”, *Annual Review of Astronomy and Astrophysics*, 1992, Vol. 30, pp543-574.
- [17] Audic S, Berthillier M, Bonini J, Bung H, Combescure A. Prediction of bird impact in hollow fan blades. In: 36th AIAA/ASME/SAE/ASEE Joint propulsion conference and exhibit, Huntsville, AL, 16–19 July; 2000.

- [18] Letellier A, Bung H, Galon P, Berthillier M. Bird impact on fan blade analysis using smooth particle hydrodynamics coupled with finite elements. In: ASME pressure vessels and piping division, symposium on structures under extreme loading conditions, vol. 351; 1997. pp. 191–5.
- [19] Chevrolet D, Audic S, Bonini J. Bird impact analysis on a bladed disk. In: RTO AVT symposium on reduction of military vehicle acquisition time and cost through advanced modeling and virtual simulation, Paris, France, April 22–25; 2002.
- [20] Starke P, Lemmen G, Drechsler K. Anwendung von FE-Simulationsmethoden bei Vogelschlag. Deutscher Luft- und Raumfahrtkongress, Stuttgart, September 23–26; 2002.
- [21] Chandra C, Wong TY, Bayandor J. Crashworthiness assessment in aircraft ditching incidents. In: ICAS 2010, 27th congress of the international council of the aeronautical sciences, Nice, France, September 19–24; 2010.
- [22] Guida M, Grimaldi A, Marulo F, Meo M, Olivares G. Bird impact on leading edge wing with SPH formulation. In: 17th International conference on composite materials, ICCM-17, Edinburgh, UK, July 27–31; 2009.
- [23] Starke P, Lemmen G, Drechsler K. Validierung von Verfahren für die numerische simulation von Vogelschlag. In: 4th German LS-DYNA Forum, Bamberg, Germany, October 20–21; 2005.
- [24] Pilz S. “Developing military vehicles and aircraft”. ANSYS Solutions 2006; 7(3):4–9.
- [25] Lavoie MA, Gakwaya A, Nejad Ensan M. Application of the SPH method for simulation of aerospace structures under impact loading. In: 10th international LS-DYNA users conference, Dearborn, MI, June 8–10, 2008.
- [26] Lammen W, Van Houten R. Predictive simulation of impact phenomena for innovations in aircraft component design. In: 6th EUROMECH nonlinear dynamics conference, Saint-Petersburg, Russia, June 30–July 4, 2008.
- [27] Tischler J. Numerische Simulation des Vogelschlag-Impakts auf eine CFKFlügelvorderkante mit Hilfe der Finite Elemente Methode, Diploma thesis, Universität der Bundeswehr München; 2003.
- [28] Joosten M, Bayandor J. Coupled SPH-composite cohesive damage modeling methodology for analysis of solid–fluid interaction. In: 46th AIAA aerospace sciences meeting and exhibit, Reno, Nevada, January 7–10; 2008.
- [29] Guida M. Study, design and testing of structural configurations for the birdstrike compliance of aeronautical components. PhD thesis, University of Naples, Italy, 2008.
- [30] Guida M, Marulo F, Meo M, Grimaldi A, Olivares G. SPH- Lagrangian study of bird impact on leading edge wing. *Compos Struct* 2011;93(3):1060–71.
- [31] Johnson AF, Holzapfel M. Modeling soft body impact on composite structures. *Compos Struct* 2003;61(1–2):103–13.
- [32] McCarthy MA, Xiao JR, McCarthy CT, Kamoulakos A, Ramos J, Gallard JP, et al. Modeling of bird strike on an aircraft wing leading edge made from fiber metal laminates – Part 2: Modeling of impact with SPH bird model. *Appl Compos Mater* 2004;11(5):317–40.
- [33] Machunze W. Numerische Analyse des Restenergie- und Restfestigkeitskriteriums für eine CFK-Slat nach Vogelschlag-Impakt, Diploma thesis, Technische Universität Dresden; 2005.

- [34] Rössler C. Numerische Simulation des Vogelschlag-Impakts auf ein CFKFlügelvorderkanten Konzept mit Hilfe der Finite-Elemente-Methode, Diploma thesis. Technische Universität München; 2004.
- [35] Johnson AF, Holzapfel M, Petrinic N. Modeling soft body impact on composite structures. In: European conference on computational mechanics, ECCM- 2001, Cracow, Poland, June 26–29; 2001.
- [36] Ubels LC, Johnson AF, Gallard JP, Sunaric M. Design and testing of a composite bird strike resistant leading edge. SAMPE Europe conference and exhibition, Paris, France, April 1–3, 2003.
- [37] McCarthy M. “Bird impact on leading edge structures”. In: CRAHVI technical workshop, Bristol, UK, March 17; 2004.
- [38] Kermanidis T, Labeas G, Sunaric M, Ubels L. “Development and validation of a novel bird strike resistant composite leading edge structure”. *Appl Compos Mater* 2005; 12(6):327–53.
- [39] Richter R. Validierung der Impakt-Resistenz einer CFK-Slat gegenüber Vogelschlag, Diploma thesis, Universität der Bundeswehr München; 2005.
- [40] McCarthy MA, Xiao JR, McCarthy CT, Kamoulakos A, Ramos J, Gallard JP, et al. “Modeling bird impacts on an aircraft wing – Part 2: Modeling the impact with an SPH bird model”. *Int J Crashworthiness* 2005; 10(1):51–9.
- [41] Kermanidis T, Labeas G, Sunaric M, Johnson AF, Holzapfel M. Bird strike simulation on a novel composite leading edge design. *Int J Crashworthiness* 2006; 11(3):189–201.
- [42] Labeas G, Kermanidis T. Impact behavior modeling of a composite leading edge structure, Fracture of nano and engineering materials and structures. In: Proceedings of the 16th European conference of fracture, Alexandroupolis, Greece, July 3-7, 2006, pp. 1259–60.
- [43] Johnson AF, Holzapfel M. Numerical prediction of damage in composite structures from soft body impacts. *J Mater Sci* 2006;41(20):6622–30.
- [44] Roth YC. Composites in high lift applications for civil aircrafts: highlights in LuFo III, IVW-Kolloquium 2006, Kaiserslautern, Germany, November 14–15; 2006, pp. 71–85.
- [45] Machunze W, Middendorf P, Keck R, Roth YC. “Design, analysis and manufacturing of a thermoplastic slat”. In: 1st European conference on materials and structures in aerospace, EUCOMAS. Berlin, Germany, May 26– 27; 2008.
- [46] Keck R, Machunze W, Dudenhausen W, Middendorf P. Design, analysis, and manufacturing of a carbon-fiber-reinforced polyetheretherketone slat. *J Aerospace Eng* 2009;223(8):1115–23.
- [47] Bayandor J, Johnson A, Thomson RS, Joosten M. Impact damage modelling of composite aerospace structures subject to bird-strike. In: ICAS 2006, 25th International congress of the aeronautical sciences, Hamburg, Germany, September 3–9; 2006.
- [48] Kindervater C, Schwinn D, Reiter A. Bird strike qualification of the external stores of the new DLR research aircraft HALO, ICAS 2010. In: 27th Congress of the international council of the aeronautical sciences, Nice, France, September 19–24; 2010.
- [49] Shmotin YN, Chupin PV, Gabov DV, Ryabov AA, Romanov VI, Kukanov SS. Bird strike analysis of aircraft engine fan. In: 7th European LS-DYNA users conference, Salzburg, Austria, May 14–15; 2009.

- [50] Zammit A, Kim M, Bayandor J. Bird-strike damage tolerance analysis of composite turbofan engines. In: ICAS 2010, 27th congress of the international council of the aeronautical sciences, Nice, France, September 19–24; 2010.
- [51] Anghileri M, Castelletti LML, Molinelli D, Motta F. A strategy to design bird proof spinners. In: 7th European LS-DYNA users conference, Salzburg, Austria, May 14–15; 2009.
- [52] Lacomme JL. “Smoothed particle hydrodynamics method in LS-DYNA”. In 3rd German LS-DYNA forum, Bamberg, Germany, October 14–15; 2004.
- [53] Selezneva M, Stone P, Moffat T, Behdinin K, Poon C. Modeling bird impact on a rotating fan: the influence of bird parameters. In: 11th International LSDYNA users conference. Dearborn, MI, June 6–8; 2010.
- [54] Anghileri M, Castelletti LML, Invernizzi F, Mascheroni M. Birdstrike onto the composite intake of a turbofan engine. In: 5th European LS-DYNA users conference, Birmingham, UK, May 25–26; 2005.
- [55] Salehi H, Ziaei-Rad S, Vaziri-Zanjani MA. Bird impact effects on different types of aircraft bubble windows using numerical and experimental methods. *Int J Crashworthiness* 2010;15(1):93–106.
- [56] Liu J, Li YL, Xu F. The numerical simulation of a bird-impact on an aircraft windshield by using the SPH method. *Adv Mater Res* 2008;33–37:851–6.
- [57] Georgiadis S, Gunnion AJ, Thomson RS, Cartwright BK. Bird-strike simulation for certification of the Boeing 787 composite moveable trailing edge. *Compos Struct* 2008;86(1–3):258–68.
- [58] Wu L, Guo YN, Li YL. Bird strike simulation on sandwich composite structure of aircraft radome. *Explosion and Shock Waves* 2009;29(6):642–7.
- [59] Bianchi F. Bird strike simulations with RADIOSS on AW helicopter blade and rotor controls. In: 3rd European hyperworks technology conference, EHTC2009, Ludwigsburg, Germany, November 2–4; 2009.
- [60] Randles, P. W., and Libersky, L. D., “Smoothed Particle Hydrodynamics: Some Recent Improvements and Applications”, *Computer Methods in Applied Mechanics and Engineering*, 1996, No. 139, pp375-408.
- [61] Lacomme, J. L., “Smooth Particle Hydrodynamics (SPH): A New Feature in LS-DYNA”, 6th International LS-DYNA Users Conference Simulation 2000, April 9-11, 2000, Dearborn, Michigan, pp7-29-7-33.
- [62] Johnson, G. R., Stryk, R. A., and Biessel, S. R., “SPH for High Velocity Impact Computations”, *Computer Methods in Applied Mechanics and Engineering*, 1996, No. 139, pp347-373.
- [63] John O.Hallquist, *Ls-Dyna, theory manual*, Livermore software technology corporation, California, USA, March 2006.
- [64] V. M. Cogolev, V. G. Mirkin, and G. J. Yablokova, "Approximate Equation of State for Solids," *Zhurnal Prikladnoi Mekhaniki i Tekhnicheskoi Fiziki*, No. 5, 1963, pp. 93-98.
- [65] A. L. Ruoff, "Linear Shock-Velocity-Particle-Velocity Relationship," *Journal of Applied Physics*, Vol. 38, No. 13, Dec. 1967, pp. 4976-4980.

- [66] P. J. Torvik, "A Simple Theory for Shock Propagation in Homogeneous Mixtures, Air Force Institute of Technology, Wright-Patterson Air Force Base, Ohio, AFIT-TR-70-3, May 1970.
- [67] Wilbeck JS. Impact behavior of low strength projectiles (AFML-TR-77-134, ADA060-423), Airforce Materials Laboratory, USA; July 1978.
- [68] Barber, J.P., Taylor, H.R., and Wilbeck, J.S., "Bird Impact Forces and pressures on Rigid and Compliant Targets," Technical Report AFFDL-TR-77-60, May 1978.
- [69] Hess, J.L. and Smith, A.M.O., "Calculation of Non-Lifting Potential Flow About Arbitrary Three-Dimensional Bodies," Douglas Aircraft Company, Report No. E.S. 40622, March 1962. Also published in Journal of Ship Research, 8, No.2, 22, September 1964, pp. 22-44.
- [70] Bauer, D.P. and Barber, J.P., "Experimental Investigation of Impact Pressures Caused by Gelatin Simulated Birds and Ice," University of Dayton Report UDR-TR-78-II4, November 1978.
- [71] W. E. Deal, "Shock Hugoniot of Air," Journal of Applied Physics, Vol. 28, No. 7, July 1957, pp. 782-784.
- [72] M. H. Rice, R. G. McQueen, and J. M. Walsh, "Compression of Solids by Strong Shock Waves", Solid State Physics (Sietz and Turnball, eds.) Academic Press, Inc, New York, Vol. 6, 1958. PP. 1- 63.
- [73] F. J. Heyman, " On the Shock Wave Velocity and Impact Pressure in High- Speed Liquid- Solid Impact, " Transactions of the ASME, (Journal of Basic Engineering), Series D, Vol. 90, July 1968, P. 400.
- [74] H. G. Hopkins, and H. Kolsky, "Mechanics of Hypervelocity Impact of Solids," Proceedings of the Fourth Symposium on Hypervelocity Impact, Air Proving Ground Center, Eglin Air Force Base, Florida, 1960, paper no. 12.
- [75] Lacombe, J.L., "Smoothed particle hydrodynamics (sph): a new feature in ls-dyna". Proceedings of the 7th International LS-DYNA Users Conference, 2002.
- [76] S. J. Leach and G. L. Walker, "The application of high speed liquid jets to cutting," Philosophical transactions of the royal society of London, A, Vol. 260, July 1966, pp. 295-308.
- [77] A. Challita, J. P. Barber, " The Scaling of Bird Impact Loads", AFFDL-TR-79-3042, Feb 1979.
- [78] L.I. Boehman, A. Challita, " A Model For Predicting Bird and Ice Impact Loads on Structures", AFWAL-TR-82-2046, May 1982.
- [79] Fatima-Zohra Belkhef, "Etude analytique de l'impact hydrodynamique et modelisation de l'écoulement potentiel de l'impact FOD » Magister Thesis, department of aeronautics, University of Saad Dahleb-Blida, Algeria, 2011.
- [80] Barber JP, Wilbeck JS. "The characterization of bird impacts on a rigid plate: part I." AFFDL-TR-75-5, ADA021142. USA: National Technical Information Service; January 1975.
- [81] Huertas-Ortecho Carlo Alberto. " Robust bird-strike modeling using LS-Dyna". Master thesis, University of Puerto Rico, Department of Mechanical Engineering, 2006.
- [82] Guida M, Marulo F, Meo M, et al. Certification by birdstrike analysis on C27J full scale ribless composite leading edge. Int J Impact Eng. 2013; 54:105–113.

- [83] Richard B. The development of a substitute artificial bird by the international birdstrike research group for use in aircraft component testing. Amsterdam: International Bird Strike Committee; April 2000.
- [84] Nechitailo RC. Bare Penetration of steel plates by long ceramic rods, metallurgical and materials applications of shock-wave and high strain rate phenomena. Elsevier Science; 1995.
- [85] Metallic materials and elements for aerospace vehicle structures. Military Handbook, MIL-HDBK-5H. USA: Department of Defense; December 1998.
- [86] Citarella R, Armentani E, Sepe R, et al. FEM simulation of a FML full scale aeronautic panel undergoing static load. *Ind Eng Manag.* 3:2169-0316; 2014.
- [87] HexWeb Honeycomb Attributes and Properties. A comprehensive guide to standard Hexcel honeycomb materials, configurations, and mechanical properties. Hexcel, USA, 1999.
- [88] Anghileri M, Castelletti L-ML, Mazza V. Birdstrike: approaches to the analysis of impacts with penetration. In: *Proc International Conference on Impact Loading of Lightweight Structures*, Florianopolis, Brazil; 2005.
- [89] Gibson, J. L., Ashby, M. F.; *Cellular Solids*, Cambridge University Press, 2nd edition 1997
- [90] Plantema, F.J.; "Sandwich Construction: The Bending and Buckling of Sandwich Beams, Plates, and Shells", 1966, John Wiley & Sons, Inc., US
- [91] Vinson, J.R.; "The Behavior of Sandwich Structures of Isotropic and Composite Materials", 1999, Technomic Publishing Company, Inc., US
- [92] Heimbs, S., Middendorf, P.,Maier, M.; "Honeycomb Sandwich Material Modeling for Dynamic Simulations of Aircraft Interior Components", 9th International LS-DYNA Users Conference, 20, pp.1-13.
- [93] Norris, G., *Creating A Titan*, Flight International, 14 June 2005.
- [94] A. S. Herrmann, *et al.*, *Sandwich structures technology in commercial aviation - Present applications and future trends*. Dordrecht: Springer, 2005.
- [95] Cocchieri, E.B. et al., 2006. A Review on the Development and Properties of Continuous Fiber / epoxy / aluminum Hybrid Composites for Aircraft Structures 2. The Production of Metal / laminate Hybrid Composites. , 9(3), pp.247–256.
- [96] Sadighi, M., Alderliesten, R.C. & Benedictus, R., 2012. Impact resistance of fiber-metal laminates: A review. *International Journal of Impact Engineering*, 49, pp.77–90.
- [97] Vogelesang, L. B., *The Development of a New Family of Hybrid Materials*, Fatigue of Aeronautical Structures as an Engineering Challenge, Lucerne, Switzerland, Emas Publishing, 2004, 3-27.
- [98] Kardomateas, G. A., and Carlson, R. L., *A Micromechanical Model for the Fiber Bridging of Macro-Cracks in Composite Plates*, *Journal of Applied Mechanics*, 1996, 225-233.
- [99] Vlot A., Vogelesang L.B. and de Vries T.J., "Towards application of fibre metal laminates in large aircraft Aircraft Engineering and Aerospace Technology", (1999), vol. 71-6, pp. 558-570
- [100] Talreja, R., *Transverse cracking and stiffness reduction in composite laminates*. *Journal of Composite Materials*, 1985. 19: p. 355-375.

- [101] Zinno, A., E. Fusco, A. Prota, and G. Manfredi, *Multiscale approach for the design of composite sandwich structures for train application*. Composite Structures, 2010. 92(9): p. 2208-2219.
- [102] Feraboli, P., F. Deleo, et al., *Predictive modeling of an energy-absorbing sandwich structural concept using the building block approach*. Composites Part a-Applied Science and Manufacturing, 2010. 41(6): p. 774-786.
- [103] Quaresimin, M., M. Salviato, and M. Zappalorto, *Strategies for the assessment of nanocomposite mechanical properties*. Composites Part B-Engineering, 2012. 43(5): p. 2290-2297.
- [104] Fermeglia, M. and S. Pricl, *Multiscale molecular modeling in nanostructured material design and process system engineering*. Computers & Chemical Engineering, 2009. 33(10): p. 1701-1710.
- [105] Caprino, G., A. Langella, and V. Lopresto, *Elastic behaviour of circular composite plates transversely loaded at the centre*. Composites Part a-Applied Science and Manufacturing, 2002. 33(9): p. 1191-1197.
- [106] Olsson, R., *Analytical prediction of large mass impact damage in composite laminates*. Composites Part A-Applied Science and Manufacturing, 2001. 32(9): p. 1207-1215.
- [107] Naik, N.K., Y.C. Sekher, and S. Meduri, *Damage in woven-fabric composites subjected to low-velocity impact*. Composites Science and Technology, 2000. 60(5): p. 731-744.
- [108] Sutherland, L.S. and C.G. Soares, *Effect of laminate thickness and of matrix resin on the impact of low fibre-volume, woven roving E-glass composites*. Composites Science and Technology, 2004. 64(10-11): p. 1691-1700.
- [109] Quaresimin, M., M. Salviato, and M. Zappalorto, *Strategies for the assessment of nanocomposite mechanical properties*. Composites Part B- Engineering, 2012. 43(5): p. 2290-2297.
- [110] Sinmazçelik, T. et al., 2011. A review: Fibre metal laminates, background, bonding types and applied test methods. Materials & Design, 32(7), pp.3671–3685.
- [111] Asundi, A. & Choi, A.Y.N., 1997. Materials Processing Technology Fiber Metal Laminates: An Advanced Material for Future Aircraft.
- [112] “Chapter 7: Advanced composite material –FAA”, by Editor, Patrick Panzera, Published in issuu, on January 13, 2014.
- [113] Airoidi A, Cacchione B. Numerical analysis of bird impact on aircraft structures undergoing large deformations and localised failure. WIT Transactions on Engineering Sciences. In: Alves M, Jones N, editors. Impact loading of lightweight structures. vol. 49; 2005.